ABSTRACT

Title of dissertation: BIOINSPIRED SENSING AND CONTROL FOR UNDERWATER PURSUIT

Brian Free
Doctor of Philosophy, 2019

Dissertation directed by: Dr. Derek Paley
Department of Aerospace Engineering
Institute for Systems Research

Fish in nature have several distinct advantages over traditional propeller driven underwater vehicles including maneuverability and flow sensing capabilities. Taking inspiration from biology, this work seeks to answer three questions related to bioinspired pursuit and apply the knowledge gained therein to the control of a novel, reaction-wheel driven autonomous fish robot. Which factors are most important to a successful pursuit? How might we guarantee capture with underwater pursuit? How might we track the wake of a flapping fish or vehicle?

A technique called probabilistic analytical modeling (PAM) is developed and illustrated by the interactions between predator and prey fish in two case studies that draw on recent experiments. The technique provides a method for investigators to analyze kinematics time series of pursuit to determine which parameters (e.g. speed, flush distance, and escape angles) have the greatest impact on metrics such as probability of survival.

Providing theoretical guarantees of capture become complicated in the case

of a swimming fish or bioinspired fish robot because of the oscillatory nature fish motion. A feedback control law is shown to result in forward swimming motion in a desired direction. Analysis of this law in a pursuit scenario yields a condition stating whether capture is guaranteed provided some basic information about the motion of the prey.

To address wake tracking inspiration is taken from the lateral line sensing organ in fish, which is sensitive to hydrodynamic forces in the local flow field. In experiment, an array of pressure sensors on a Joukowski foil estimates and controls flow-relative position in a Kármán vortex street using potential flow theory, recursive Bayesian filtering, and trajectory-tracking, feedback control.

The work in this dissertation pushes the state of the art in bioinspired underwater vehicles closer to what can be found in nature. A modeling technique provides a means to determine what is most important to pursuit when designing a vehicle, analysis of a control law shows that a robotic fish is capable of pursuit engagements with capture guarantees, and an estimation framework demonstrates how the wake of a swimming fish or obstacle in the flow can be tracked.

BIOINSPIRED SENSING AND CONTROL FOR UNDERWATER PURSUIT

by

Brian Anderson Free

Dissertation submitted to the Faculty of the Graduate School of the
University of Maryland, College Park in partial fulfillment
of the requirements for the degree of
Doctor of Philosophy
2019

Advisory Committee:
Professor Derek A. Paley, Chair/Advisor
Professor Nikhil Chopra, Dean's Representative
Professor Anya Jones
Professor Michael Otte
Professor Robert M. Sanner

Dedication

To Lilly. My life, my love, and my lady.

Acknowledgments

I'd first like to thank my advisor, Prof. Derek Paley. He taught me a great many things over the course of my time in the Collective Dynamics and Controls Lab. He taught how to write an academic paper, how to clearly present my research to a broad diversity of audiences, and how to navigate the sometimes confounding landscape of the academic game. Dr. Paley helped me grow as a researcher and an adult by encouraging me to push myself outside of my comfort zone. "Challenge your assumptions" is a simple piece of advice he shared that has stuck with me. Following this advice helps tremendously not only to make headway in difficult lines of research, but also on my continuing journey of personal growth.

I'd also like to thank my dissertation committee for the time and energy they have gifted me in my pursuit of this degree. The feedback and challenges I have received from my committee has greatly strengthened my confidence and ability to present and *defend* my ideas. Professors Anya Jones, Robert Sanner, Michael Otte, and Nikhil Chopra were critical to this work and I thank them for their efforts.

Outside of his role as my committee member, I'd like to thank Dr. Sanner for his helpful discussions on probability theory and his feedback on making a technical paper clear to someone who has not been reading it over and over for a month. I have enjoyed four classes with Dr. Sanner and what I learned has not only laid the base foundation of my controls knowledge, but also my basic programming skills. I'd also like to thank Dr. Otte for his willingness to engage and his guidance in his Motion Planning class, a course that broadened my narrow view of controls to

encompass a much more realistic view.

This work would be impossible without our collaborators at Michagin State University and University of California, Irvine. Prof. Xiaobo Tan and his students Montassar Sharif and Hong Lei worked very hard on the bioinspired artificial lateral line. A visit from these two students in the Summer of 2016 and some late nights resulted in some of the earliest experimental results in this work. Prof. Matt McHenry and his student Alberto Soto provide invaluable insight into the biology of fish and hosted me for over a week in the Summer of 2017 as we studied the bluefish experimental data. Thanks for teaching me how to surf, too, Matt!

My labmates and colleagues in the department have been both technically and socially helpful and so I owe them my thanks. Frank Lagor showed and told me what it meant to be a graduate student and was a better mentor in my first few years than I could have asked for. Jinseong Lee knows our fish like no other man and I thank him for his efforts towards this goal. Jinseong designed and constructed the fish robot and directed two summer interns, Jenny Mei and Brynne Schoen, in the design of a custom printed circuit board for the robot. I owe thanks to Daigo Shishika, Brett Barkley, Will Craig, Debdipta Goswami, Jordan Boehm, Will Scott, and Artur Wolek for the memories and good times.

Throughout my research I have made use of the excellent facilities at the University of Maryland. I thank the Space Systems Lab for permitting my use of the Neutral Buoyancy Research Facility, particularly Prof. Dave Akin and his student Jeremy Chang. I appreciate the administrative staff in the Department of Aerospace Engineering and their help in arranging equipment orders, travel, and de-

grees. LaVita Williams, Becky Sarni, Otto Fandino, Tom Hurst, and Matt Sinclair, thank you. And of course I am thankful to the cleaning staff in the Kim Building and particularly Reyna of the third floor por nuestras divertidas conversaciones.

Outside of my academic world, there are many friends to whom I owe gratitude for listening to my worries and condoning my company. My past and present housemates, Scott Kindl, Tayler Esherick, Logan Grace, Luke Smith, Eric Frizzel, Travis Burch. My chemistry partner, Greg Holland. The denizens of my home away from home (but still in my neighborhood) Laura Paquin, Wayni Ng, Elain Petro, Caitlin King, Arber Masati. And Jenna Schueler, with whom I have found a friendship deeper and truer than any I have heard.

Of course this work would not be possible without financial support from a personal fellowship from the National Science Foundation Graduate Research Fellowship program (Grant No. DGE 1322106) and a grant from the Office of Naval Research (Grant No. N000141512246).

Table of Contents

List of Tables

List of Figures

Chapter 1: Introduction

1.1 Motivation for bioinpired pursuit

The motivation to take inspiration from biology in the development of pursuit with underwater vehicles follows a long history of man's fascination with nature's design. As far back as the myth of Icarus and Daedalus in Ancient Greece, man has yearned to make use of the solutions presented by natural selection. Studying nature to attain inspiration for engineering design has a history all the way from DaVinci's glider inspired by the structure of the bat's wing to the Wright Brother's flyer [1]. In more recent history, there has been interest in the touch-at-a-distance lateral line sensing modality in fish and its uses in an engineering context for the development of underwater autonomous vehicles [2–6]. Additionally, there have been many studies of the pursuit tactics used by animals in nature including humans, dogs, birds, dragonflies, bats, and fish [7–14]. This dissertation focuses on taking inspiration from the form and behavior of fish in the development of sensing and control algorithms for autonomous underwater vehicles.

Predation is a fundamental interaction between species, yet it is largely unclear what tactics are successful for the survival or capture of prey. One challenge in this area comes with how to test theoretical ideas about strategy with experimental mea-

surements of features such as speed, flush distance, and escape angles. Tactics may be articulated with an analytical model that predicts the motion of predator or prey as they interact. However, it may be difficult to recognize how the predictions of such models relate to behavioral measurements that are inherently variable. Here an alternative approach for modeling predator-prey interactions that uses deterministic dynamics, yet incorporates experimental kinematic measurements of natural variation to predict the outcome of biological events is presented. This method allows researchers to hypothesize why a particular species may have an evolutionary imperative to improve some features rather than others. From an engineering context, it allows designers to make informed decisions on where to focus resources. For example, is it better to have a faster vehicle or better sensing capabilities given limited resources?

Theoretical guarantees of capture become complicated in the case of a swimming fish or fish robot because of the oscillatory nature of the fish heading. Knowledge of the conditions under which capture is guaranteed is very important from both a biological and engineering perspective. In both cases, if it is known ahead of time that capture is unlikely, it is in the best interest of the pursuer to conserve resources by not engaging in pursuit.

Wake tracking is achieved by fish in nature through the use of their lateral line, a distributed sensing organ composed of mechanosensitive hairs that deflect in response to the flow field around the fish. Fish use this sensing modality to forage, capture prey, and follow walls even in complete darkness [5]. Equipping an underwater vehicle with an artificial lateral line composed of distributed pressure sensors

adds a complementary sensing modality for estimating the location of a target on top of the traditional computer vision solutions. In particular, this lateral line sensing modality has great use in murky or clouded waters where visual information is greatly degraded.

1.2 Relation to prior work

1.2.1 Probabalistic modeling of predator-prey interations

Predation is critical to the structure of populations and has guided the evolutionary fate of myriad species. Despite its importance in biology, investigators have struggled to formulate a predictive body of theory for understanding the behaviors that succeed in the survival or capture of prey. It is consequently unclear what traits of a predator or prey are most important to predation. This challenge has been met through the development of analytical models that articulate tactics and predict the motion of these animals. However, it is difficult to reconcile these predictions with kinematic measurements due to the highly uncontrolled and coupled nature of behavioral interactions between predator and prey. The aim of the current study is to advance our understanding of the behavior of predation through the introduction of an analytical approach that incorporates kinematic measurements of natural variation into analytical models of predator and prey tactics.

The work here is motivated by the importance of predation in the survival of a species. While this motivation may suggest that we study the growth rate of species, we instead take a individual-centric approach where we seek to quantify the

expected value of a metric of success in the predator-prey interaction. We demonstrate the utility of our approach, called probabilistic analytical modeling (PAM), by modeling predator-prey interactions in fishes that have been observed experimentally. Measurement of kinematic features such as speed, flush distance (escape or alert distance), and escape angles from experiment combined with dynamical modeling and probabilistic analysis predict the outcomes of biological events in ways that experiments or modeling alone cannot.

Hypothetical tactics of predators and prey have been previously formulated with analytical pursuit-evasion models. These models predict the trajectories of individuals [15–17], or the swarming behavior of one target and many pursuers [18,19], as particles capable of responding to the state of the opposing animal according to a behavioral algorithm [20–23]. Due to the transparency of analytical mathematics, it is possible to identify the parameters in these algorithms that optimize a particular aspect of performance. For example, the classic homicidal chauffeur game model was successfully used to formulate the direction of the escape response by prey fish that maximizes the distance from a predator [24, 25]. This model has been invoked in the interpretation of numerous experimental studies on prey fish [26–30].

However, attempts at reconciling theory with experimentation demonstrate some of the limitations of existing theory. The homicidal chauffeur model assumes that predator and prey maintain a fixed heading and velocity and that the prey senses the predator's speed and heading with perfect accuracy. These assumptions seem unlikely to hold true in most piscivorous interactions and it is therefore unclear to what extent measured deviation from predictions may be attributed to violations

of the model's assumptions, fish using a different tactic, or other natural variation in behavior. As a consequence, it is not clear whether prey fish escape optimally with respect to some metric (e.g., distance from the predator) or not.

The effects of natural variation have been considered by computational models that include stochasticity. Such data-driven models include those of fish schools that respond to a predator [31] and a schooling model that investigates how perturbations among a small number of agents affects the behavior of the school at large [32]. Certain classes of stochastic pursuit-evasion games have even been solved [33] and the importance of not using deterministic models in stochastic systems is highlighted in a model of the growth rate of feeding fish [34]. In work on specific species, data-driven techniques with stochastic or probabilistic elements are used to model the fast-turning dynamics of zebrafish [35], the probability of capture for suction feeding sunfish [36], the predation by the exotic shrimp species *Dikerogammarus villosus* [37], and the dynamics of the bacterial predation in soil [38]. On a macro scale, predator-prey population dynamics in the sense of Lotka-Volterra [39] are modeled with stochastic components to the birth and death rate of the species [40] and with data fitting techniques that generalize the local predator-prey interactions to the population dynamics as a whole [41].

Although perhaps more predictive than a classic analytical model, the above data-driven models lack the advantages of analytical analysis for formulating tactics that optimize some payout. The same disadvantage is apparent through a Monte Carlo approach to pursuit-evasion models. Monte Carlo approaches yield distributions of numerical results from batches of deterministic simulations that draw

parameter values from random-number generation according to measured probability distributions [42].

The alternative provided by this dissertation is called probabilistic analytical modeling (PAM). PAM is similar in concept to a Monte Carlo approach, but has the additional advantage of providing analytical transparency. Rather than using many numerical simulations of system dynamics and predicting the outcome from the resulting distribution of simulation outcomes, PAM applies tools from probability theory to the dynamics of the system to directly calculate the expected value of a metric of interest. This new tool provides a means for researchers to examine kinematic time series of pursuit to evaluate which parameters in a predator/prey interaction have the greatest effect on the key metric, typically probability of survival.

1.2.2 Bioinspired pursuit

Pursuit has long been a study of interest to researchers and engineers both for its mathematical elegance and its practicality in a world at war where intelligent guidance strategies for boats, planes, and missiles are critical to mission success [20, 21, 43]. In the context of this dissertation, we are interested in pursuit by autonomous underwater vehicles. This research area is itself one that bears many fruit, with applications to surveillance, ship inspection, and search and recovery [44–46]. However, the focus of this dissertation is more narrow in that it specifically deals with the state of the art in fish-inspired underwater vehicles.

A fish-inspired robot has several advantages over a traditional, propeller-driven underwater vehicle. Robots inspired by fish have been seen to be capable of rapid turning maneuvers due to their articulated or flexible bodies, energy efficient locomotion, and stealthy swimming [47–49]. Many types of fish-inspired underwater vehicles are seen in the literature including some with external actuators such as screws, fins, or wings of underwater vehicles [49–51]. Many of these designs suffer from excessive noise or distinct acoustic signatures that detract from their ability to act as surveillance drones [52].

Locomotion via an internal reaction wheel does not suffer from these shortcomings due to the actuating component being contained within the body of the robot. Reaction wheels are a technology typically used in satellite design to orient the craft without the use of fuel [53]. The principle of operation is conservation of angular momentum. As a heavy disc or wheel is accelerated by a motor in one direction, the body rotates in the opposite direction.

Recently, however, the reaction wheel has begun to see use in the development of swimming robots [55–57]. The oscillatory motion of the robots under the effect of the reaction wheel causes the fish-shaped bodies to form and shed a vortex, propelling the craft forward. These works lack a convenient means to model the dynamics of a fish robot swimming under this type of reaction wheel actuation, a gap that has been filled in recent years. A mathematical analog between a fish-shaped robot with an internal reaction wheel and a Chaplygin sleigh with an internal reaction wheel has been found by taking advantage of a shared non-holonomic constraint [58].

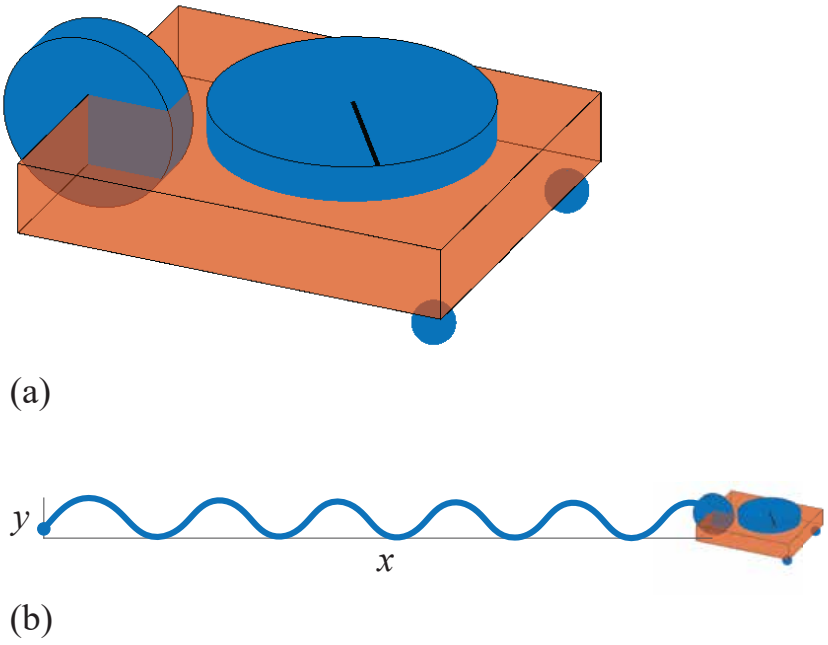

Figure 1.1: (a) Chaplygin sleigh schematic. A wheel in the back constrains motion to be perpindicular to its axis. Two casters in the front allow the sleigh to pivot about the wheel. A heavy disc on top is actuated by a motor to drive the sleigh forward. (b) Trajectory of the sleigh under a sinusoidal motor torque. This figure has been included here for the reader's clarity and is inspired by a figure from [54].

Before continuing, it is necessary to give a brief aside on the Chaplygin sleigh. The Chaplygin sleigh is one of the canonical examples in many classical mechanics textbooks used to demonstrate how energy methods can be used to derive equations of motion for a system with non-holonomic constraints [59]. The non-holonomic system is one with differential constraint, which has the effect of making the state of the system dependent on the path taken to get there. The non-holonomic constraint in the Chaplygin sleigh is the wheel or knife's edge that does not allow any transverse velocity. It is the similarity of this constraint to the Kutta condition on a foil, which dictates that flow must leave smoothly at the trailing edge [60], that allows the treatment of this type of fish robot as having the dynamics of a Chaplygin sleigh. Figure 1.1 shows a schematic of a Chaplygin sleigh and an illustration of the path it takes under a sinusoidal input torque on the reaction wheel.

The connection between the Chaplygin sleigh and reaction-wheel propelled fish robot allows the relatively simple dynamics of the Chaplygin sleigh to be used in the control design and analysis for steering and propulsion of the fish robot, which I hereafter refer to as the Chaplygin fish.

To steer a Chaplygin fish using a reaction wheel, various torque profiles such as symmetric, asymmetric, and impulsive have been used [55,61]. Other works focus on the analysis of the energy of the Chaplygin sleigh's motion as a piecewise-smooth non-holonomic constraint and simulate transitions between distinct dynamics belonging to the slip and stick modes [57, 62]. However, these prior works are limited to solid-bodied robots [57, 61–64], and do not use state-feedback control.

There has been no work prior to this dissertation and a preliminary conference

paper [65] that provides a control algorithm that is autonomous (meaning no explicit dependence on time [66]), continuous, or uses state-feedback control. A control algorithm of this type greatly increases the ease of analysis from a control-theoretic standpoint and relies less on empirical observations of the robot behavior under the control law. Furthermore, there has been no work detailing the use of one of these Chaplygin fish in pursuit, much less any means to provide guarantees of successful capture. This is likely due to the relative youth of the reaction-wheel driven underwater vehicle subset of the controls community.

Outside of the context of the Chaplygin fish, however, there has been much work on how to provide theoretical guarantees of capture. Game theoretic formulations of pursuit can provide formal solutions to the optimal control strategy that yields the best chances of capture [33, 67]. Advanced nonlinear control techniques such as sliding mode and robust partial control design have been used to guarantee capture of evasive targets with unknown dynamics but known maximum accelerations [19, 68, 69]. These works assume a vehicle with two traditional control inputs, steering and thrust, to change direction and speed, respectively. The Chaplygin fish has only one control input, the torque imparted on the internal reaction wheel, and so more care is needed to provide capture guarantees due to the necessarily oscillatory motion in the heading.

1.2.3 Vortex estimation and flow relative control

Autonomous navigation of underwater vehicles through complex flow struc-

tures such as the turbulent wake of another vehicle requires a sensing mechanism to perceive variable flow patterns. Fish have a sensing structure known as the lateral line, which contains spatially distributed superficial and canal neuromasts sensitive to flow velocity and pressure gradients respectively [2, 3], that provides inspiration for a similar sensing system for underwater vehicles. Fish utilize lateral-line sensing of the hydrodynamic properties of the flow to help navigate and seek prey, even in complete darkness [4, 5, 70]. Bioinspired artificial lateral lines comprised of pressure sensors have the potential to enable robotic platforms to estimate the flow speed and angle of attack in uniform flows [71] and the location and strength of circulating flow structures such as vortices and vortex streets [72].

A frequently studied circulating structure is the Kármán vortex street, a pattern of clockwise and anti-clockwise vortices shed by a blunt body due to flow separation [73]. This pattern is also produced in the wake of fish as they swim (though with opposite vortex strength, known as a reverse Kármán vortex street) [74], and is investigated here as a precursor to fish-robot multi-vehicle control including pursuit and schooling behavior. Figure 1.2 shows a schematic of both a Kármán vortex street and a reverse Kármán vortex street.

This work describes the use of a Bayesian filter in conjunction with a potential flow model and distributed pressure sensors on a fish-shaped, underwater Joukowski foil [60, 75] to estimate the strength, phase, and cross-stream location of a Kármán vortex street, as well as the design of a feedback controller to drive the foil to an arbitrary reference trajectory through the street. The Joukowski foil is fixed in its downstream position in a flow tank and its angle of attack is controlled so

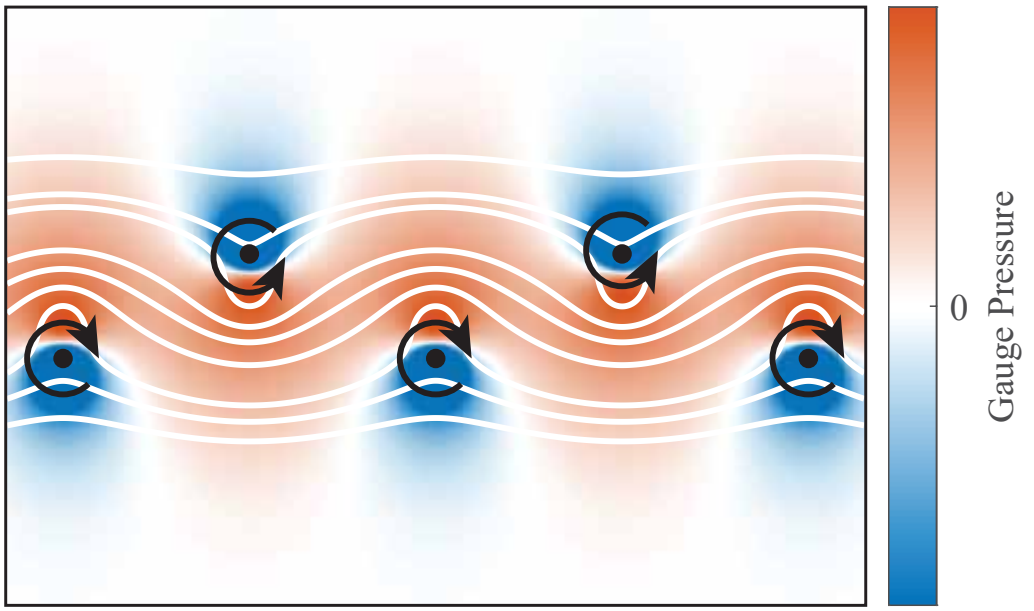

(a)

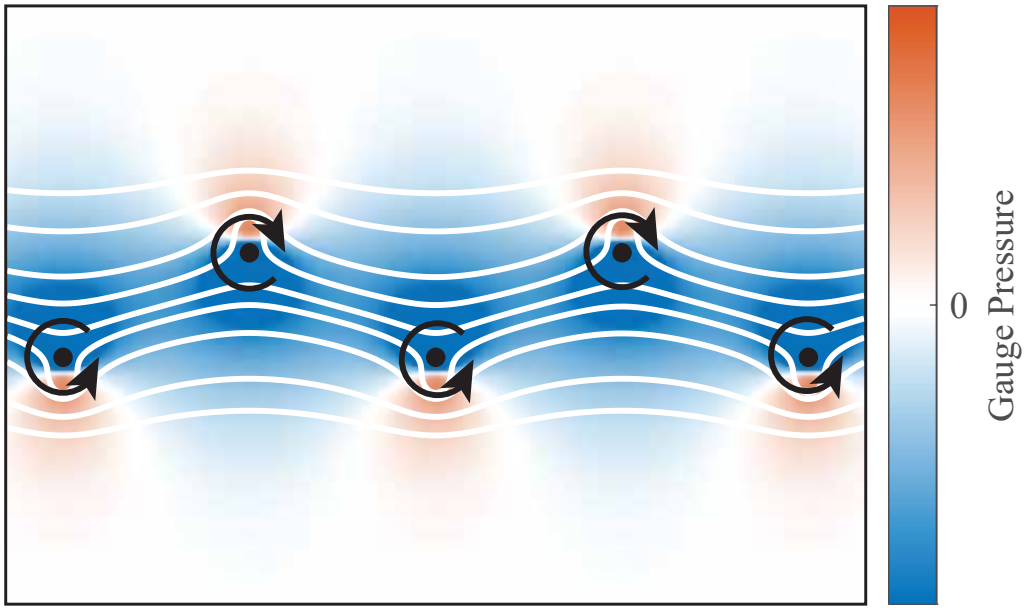

(b)

Figure 1.2: Illustration of (a) Kármán vortex street and (b) Reverse Kármán vortex street. White lines are streamlines. Black circles indicate vortex locations within the street and arrows indicate the direction of rotation. Orange indicates a pressure higher than the freestream and blue, lower.

the foil moves in the cross-stream direction along an air-bearing track. It can be programmed to follow any differentiable reference trajectory through a vortex street. In particular, both an optimal sinusoidal path determined by empirical observability and the slaloming path known as Kármán gaiting are experimentally validated. Observability is a concept that determines how well a set of states can be reproduced from a set of measurements, if at all.

Fish in nature slalom through alternating vortices using a combination of their lateral line and vision system and are capable of Kármán gaiting even in the absence of vision [76]. Research has also shown that during Kármán gaiting behavior the tail-beat frequency of the fish matches the vortex-shedding frequency, and muscle activity decreases compared to station holding in uniform flow [77]. Dead (but still flexible) trout towed behind an obstacle in the flow can even exhibit Kármán gaiting and passively generate thrust [78].

The lateral line in fish is an important sensing mechanism for navigating the underwater space, particularly for Kármán gaiting, but also for schooling [79], predator/prey detection [80, 81], and wall following [5]. The effective sensing range of the lateral line is on the order of one body length [82]. An artificial lateral line has the capability of providing the same sensing mechanism to robotic fish and marine vessels. The signal on the nerve fibers in fish associated with the lateral line carries enough information to determine the vortex-shedding frequency of a Kármán vortex street and can also be decoded to locate the source of a vibrating dipole [83, 84].

There is a well established research effort in applying the sensing principles seen in the lateral line of fish to the development of an artificial lateral line (ALL)

to be deployed on underwater vehicles. It has been demonstrated that an ALL comprised of spatially distributed pressure sensors is capable of localizing a vibrating dipole [85], estimating freestream flow direction [6] as well as freestream speed [71], localizing upstream obstacles [86], and tracking moving obstacles through a flow field [87]. These works demonstrate that the ALL sensing modality is capable of determining some of the basic flow parameters in an engineering context. The ALL can be used with rudimentary control algorithms to demonstrate some of the same behaviors as fish, such as rheotaxis [6, 71], the alignment of the head towards the direction of oncoming flow.

The focus of the ALL work in this dissertation is in the estimation of the state of a Kármán vortex street. The presupposition of this task is that there exists a method to estimate the state of a single vortex, since a vortex street is composed of many vortices. On this front, there has also been progress made by researchers over the years. ALL have been shown to be capable of estimating the strength of free vortices [88] and the position of moving vortices [87]. It has been shown that the readings from an ALL contain enough information to estimate the state of a vortex street (position, vortex spacing, vortex strength) [89], though no method to do so was provided in that work. Efforts to estimate the full state of a vortex street have been only partially successful. Some researchers have utilized empirical methods to determine whether or not an ALL is within a vortex street [90, 91] as well as vortex shedding frequency [91, 92]. Methods to estimate the source of a vortex street from ALL measurements onboard robots has been demonstrated [92, 93], but no means to estimate the location of individual vortices within the street are in the literature.

In order to display the Kármán gaiting behavior onboard an underwater vehicle, it is necessary to estimate the location of each vortex within the street.

A model-free approach [85, 90–93] relies on examining the data from an artificial lateral line and establishing heuristic methods to determine various parameters of a vortex street. The analytical model developed herein is independent of the shape of the Joukowski foil and sensor placement so it is easily adaptable to a variety of platforms, whereas a model-free approach requires new heuristics for each sensor or body configuration.

The state of the field is thus. There have been many works demonstrating using an ALL to estimate the state of various flow structures including vortices and vortex streets. Several of these works have performed control actions relative to these flow structures, but none have attempted the Kármán gaiting behavior. The estimation methods include Kalman Filters [88], Particle Filters [87], Bayesian Filters [71, 86], as well as more empirical methods. This dissertation builds upon those works and extends the capabilities of the ALL to include estimation of the position and strength of a vortex street. Additionally, this dissertation provides a control algorithm that will guide a robot to any arbitrary reference trajectory through a Kármán vortex street, not only the bioinspired Kármán gaiting path.

1.3 Contributions to the state of the art

This dissertation provides research contributions in the areas of data-driven modeling, pursuit, and estimation. The main results of this dissertation have been

already published in peer-reviewed journals or have been submitted to journals and are under review [14, 94, 95]. Early results for pieces of this project appeared in conference proceedings [65, 72, 96]. Certain sections of this dissertation have not appeared elsewhere, notably many of the pursuit results. The work in those publications was performed in collaboration with the coauthors, but the following contributions are due to my personal efforts there within.

1.3.1 Probabalistic Analytical Modeling

I created a data-driven framework to identify key features of survival. Starting with an experimental dataset of the kinematics of the predator/prey interactions, this technique provides a mechanism to determine which parameter in a dynamic model has the greatest effect on some key metric (e.g. probability of capture). This technique was applied in two case studies. The first case study on the predation of fundulus by bluefish showed that bluefish do not use time-optimal pursuit tactics. The second case study on the predation of larval zebrafish by adults showed that sensing range is most important to the survival, having a greater effect on probability of capture than even escape speed.

1.3.2 Bioinspired pursuit

Taking advantage of the shared non-holonomic connection between this system and the Chaplygin sleigh, I propose an autonomous feedback law that results in a stable, forward-swimming limit cycle of a fish robot in the desired direction. Ad-

ditionally, I performed analytical and numerical bifurcation analyses to determine what control gains result in the desired limit cycle. Using this control law, I derived an expression for evaluating whether or not capture is guaranteed based on parameters such as the control gains, physical parameters of the robot, and maximum speed and turning rate of the prey. Finally, I demonstrated use of this control law for pursuit in the Neutral Buoyancy Research Facility testbed using a flexible fish robot driven by an internal reaction wheel facilitated by a motion capture system in the control loop. This robot was designed and constructed by my labmate Jinseong Lee, but I am solely responsible for the onboard programming and its experimental use.

1.3.3 Vortex estimation and flow relative control

I developed a grid-based Bayesian filter framework to estimate the state of a vortex street. Specifically, distributed pressure sensors combined with a potential flow model for a Joukowski airfoil in a Kármán vortex street allows the Bayesian filter to estimate the strength, planar location, and phase relative to a fish robot. I also developed feedback control of a foil to an arbitrary phased-based reference trajectory through a Kármán vortex street. I used tools from empirical observability to establish the optimally observable trajectory through a Kármán vortex street, which is the one that intersects each vortex in the street.

1.4 Outline of dissertation

The organization of this dissertation is as follows. Chapter 2 provides necessary technical background for the subsequent chapters. The mathematical frameworks of potential flow theory, Bayesian estimation, probability theory, and pursuit are presented to familiarize the reader with basic tenants of these fields before bringing their tools to bear on the problem at hand.

Chapter 3 proposes a technique for analyzing kinematic time-series of predator-prey interactions called Probabalisitc Analytical Modeling. This technique is an alternative to Monte Carlo simulations and its use in determining which model parameter has the greatest effect on some metric is demonstrated in two case studies of fish predator-prey interactions.

Chapter 4 covers the development of a novel, reaction wheel driven underwater robot inspired by fish as well as the conditions necessary to guarantee capture with this vehicle. Experimental demonstration in an underwater motion capture arena shows the vehicle to be capable of pursuit.

Chapter 5 describes the efforts to use an artificial lateral line to estimate the state of a Kármán vortex street, a pattern of left/right vortices that is shed in the wake of a swimming fish. Potential flow is used to model the flow field and a grid-based Bayesian filter is developed to provide real-time estimates of vortex position for use in closed-loop feedback control.

Chapter 6 summarizes the work done here, presents the contributions of this work, and makes suggestions for future work in this area.

Chapter 2: Technical background

Before covering the work done in this dissertation, it is necessary to present background information on complex variables, potential flow, Bayesian estimation, pursuit, and the dynamics of the Chaplygin sleigh. The tools provided here are used in later chapters to derive the results of interest.

2.1 Complex variables

Throughout this dissertation complex variables are used to compactly represent planar location, rather than pairs of coordinates. A full treatise on this subject is beyond the scope of this work, and so we provide only the facts necessary to understand the subsequent content. In a Euclidean space, planar location is most often represented as coordinate pairs (x, y), the horizontal and vertical displacement from the origin, or (r, θ), the distance and angle from the origin. Complex variables have both a real and imaginary component and so a single complex variable z contains two pieces of information, which makes it attractive from a compactness and aesthetic point of view.

Define a complex variable $z = x + \mathbf{j}y = r\exp(\mathbf{j}\theta)$ [97]. Here and throughout this work we use $\mathbf{j} = \sqrt{-1}$ to be the imaginary number. The conjugate of a complex

variable z is defined as $\overline{z} = x - \mathbf{j}y = r\exp(-\mathbf{j}\theta)$. That is to say, the sign of the imaginary component of the variable is reversed. This is useful for calculating the magnitude or absolute value of a complex variable $|z| = \sqrt{z\overline{z}} = \sqrt{x^2 + y^2} = r$.

On top of the traditional definition of the conjugate of a variable, there are several notions of the complex conjugate of a function used in literature and in this work, so it is important to be clear on what is meant by each. Below are definitions of 3 types of complex conjugates of a function $f(z)$ where $z = x + \mathbf{j}y$ is a complex number [98–100]. These notions are used in Chapter 5 in the use of the Milne-Thomson Circle Theorem.

$\overline{f(z)}$: evaluate $f(z)$ completely and take conjugate of result, e.g.

$$f(z) = 6z + 3\mathbf{j}z^2$$

$$z_* = 1 - 2\mathbf{j}$$

$$f(z_*) = 18 - 21\mathbf{j}$$

$$\overline{f(z_*)} = 18 + 21\mathbf{j}$$

$f(\overline{z})$: replace z with $\overline{z}$ in $f(z)$ and evaluate, e.g.

$$f(z) = 6z + 3\mathbf{j}z^2$$

$$z_* = 1 - 2\mathbf{j}$$

$$f(\overline{z_*}) = 6\overline{z_*} + 3\mathbf{j}\overline{z_*}^2$$

$$f(\overline{z_*}) = -6 + 3\mathbf{j}$$

$\overline{f}(z)$: replace $\mathbf{j}$ with $-\mathbf{j}$ everywhere it appears explicitly in $f(z)$ (including constant terms, as in switch z_0 to $\overline{z_0}$ if z_0 is a constant that appears in $f(z)$)and

evaluate, e.g.

$$f(z) = 6z + 3\mathbf{j}z^2$$

$$z_* = 1 - 2\mathbf{j}$$

$$\overline{f}(z) = 6z - 3\mathbf{j}z^2$$

$$\overline{f}(z_*) = -6 - 3\mathbf{j}$$

Notes on $\overline{f}(z)$:

1. Replacing $\mathbf{j}$ with $-\mathbf{j}$ must be done before evaluating the argument of the function. It is best to think of $\overline{f}(z)$ as a function separate from $f(z)$ entirely.
2. $\overline{f}(z) = \overline{f(\overline{z})}$
3. $\overline{f}(\overline{z}) = \overline{f(z)}$

2.2 Potential flow theory

Potential flow theory provides tools to calculate the velocity at any point in a field from the derivative of a scalar function. Its use assumes that flow is irrotational, inviscid, and incompressible [75]. Complex potential flow uses a complex number $z = x + \mathbf{j}y$ to represent planar coordinates. This also allows for a single derivative with respect to the complex variable z to represent the velocity field, rather than one derivative each for the x and y velocity components.

Potential flow allows the calculation of the velocity vector field from the derivative of a scalar function [75]. Let $z = x + \mathbf{j}y = re^{\mathbf{j}\theta}$ be the complex coordinates in

some reference frame. Define complex potential $f(z) = \phi + \mathbf{j}\psi$ where ϕ is the potential function and ψ is the stream function.

To calculate the conjugate velocity field, take the derivative with respect to z,

$$\frac{\mathrm{d}f}{\mathrm{d}z} = w(z) = u - \mathbf{j}v, \tag{2.1}$$

where u and v are the real-valued horizontal and vertical velocities respectively. The true velocity field is found by taking the functional complex conjugate, $\overline{w(z)} = u + \mathbf{j}v$. Alternatively, taking the real and negative imaginary components gives

$$u(z) = \mathrm{Re}(w(z))$$

and

$$v(z) = -\mathrm{Im}(w(z))$$

Observe the potential flow function for a point vortex at the origin,

$$f_{\mathrm{vortex}}(z) = -\mathbf{j}\frac{\Gamma}{2\pi}\log z.$$

Here we use $\log z$ to indicate natural logarithm, which is sometimes also referred to as $\log_e z$ or $\ln z$. Taking the derivative with respect to the complex variable z,

$$\begin{aligned}\frac{\mathrm{d}f_{\mathrm{vortex}}}{\mathrm{d}z} &= -\mathbf{j}\frac{\Gamma}{2\pi z} \\ &= -\mathbf{j}\frac{\Gamma}{2\pi r e^{\mathbf{j}\theta}} \\ &= -e^{\mathbf{j}\pi/2}\frac{\Gamma e^{-\mathbf{j}\theta}}{2\pi r}\end{aligned}$$

Complex potential makes use of the principle of superposition allowing multiple flows to be combined into a single field. To model the flow over a lifting

cylinder, combine the complex potentials of a uniform freestream, a doublet, and a point vortex

$$f_{\text{lifting cylinder}} = Uz + U\frac{r_0^2}{z} - \mathbf{j}\frac{\Gamma}{2\pi}\log z. \tag{2.2}$$

The freestream speed is given by U, the radius of the cylinder by r_0, and the circulation strength by Γ. The conjugate velocity W is found by taking the derivative,

$$W_{\text{lifting cylinder}} = \frac{\mathrm{d}f_{\text{lifting cylinder}}}{\mathrm{d}z} = U - U\frac{r_0^2}{z^2} - \mathbf{j}\frac{\Gamma}{2\pi z}. \tag{2.3}$$

Figure 2.1 shows the resulting flow field with color indicating the pressure difference from p_∞. The pressure field was calculated according to Bernoulli's principle, which states that total pressure is conserved for incompressible, irrotational, inviscid flow [60]. Here, total pressure is given by $p_\infty + \frac{1}{2}\rho|W|^2$ where p_∞ is the ambient pressure of the flow field at speed U [60]. The circulation term in these equations can be physically interpreted as rotation of the cylinder, which has the effect of generating lift. Many phyically meaningful flows can be modeled this way, by taking advantage of the principle of superposition and the ability to combine simple flow elements into something greater.

2.3 Grid-based Bayesian filter

The estimation of the states of the vortex street in Chapter 5 is performed by a recursive, grid-based Bayesian filter [101, 102] and so we provide background here. The principle of this filter is to form a measurement model that predicts what the measurements from the sensors would be if the state of the system were a

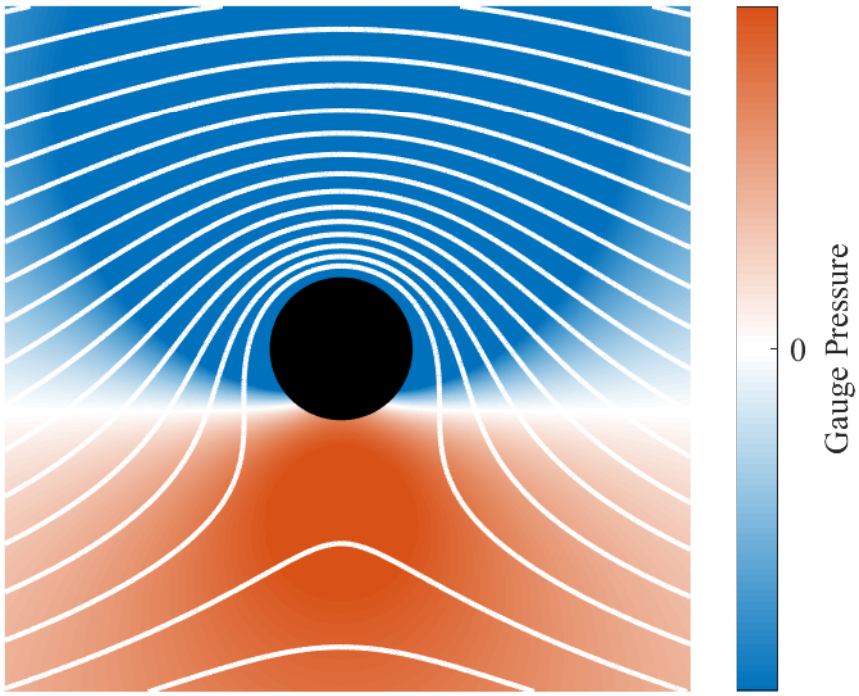

Figure 2.1: Lifting cylinder. White lines are streamlines. The color of the gauge pressure field indicates the difference from the freestream pressure. Orange indicates that the pressure is higher than the freestream, blue that it is lower, and white that it is equal. In this example, the pressure differential between the upper and lower surfaces of the cylinder generates lift. The freestream moves from left to right and the cylinder rotates in the counter-clockwise direction.

particular value in the state space. By comparing the measurement predictions of every point in the state space grid with the actual measurement, a multi-dimensional conditional probability density function (PDF) is formed, called the measurement likelihood function. The likelihood function is combined with the *prior* PDF of the previous time step to become the *posterior* PDF according to Bayes' theorem. The posterior then becomes the prior of the next time step after it is forecast forward according to the system dynamics including process noise.

The recursive, grid-based Bayesian filter estimates a set $\mathbf{X}$ of parameters from a set $\mathbf{Y}$ of measurements [101]. Suppose the instantaneous measurement vector is

$$\mathbf{Y} = \mathscr{H}(\mathbf{X}) + \eta, \tag{2.4}$$

where $\mathscr{H}(\mathbf{X})$ is the (nonlinear) measurement equation relating the state vector $\mathbf{X}$ to the measurement vector $\mathbf{Y}$ and η is (Gaussian) sensor noise. With m as the number of measurements, the measurement vector is

$$\mathbf{Y} = [y_1, \ \ldots \ , y_m]^T \in \mathbb{R}^m. \tag{2.5}$$

2.3.1 Likelihood function

For the grid-based Bayesian filter with Gaussian measurement noise, the likelihood function is the following conditional probability of measurement $\mathbf{Y}$ given state vector $\mathbf{X}$ [101]:

$$\pi(\mathbf{Y}|\mathbf{X}) = \frac{1}{\sqrt{(2\pi)^n \det(R)}} \exp\left[-\frac{1}{2}(\mathbf{Y} - \mathscr{H}(\mathbf{X}))^T R^{-1} (\mathbf{Y} - \mathscr{H}(\mathbf{X}))\right], \tag{2.6}$$

where n is the dimension of the state space and $R \in \mathbb{R}^{m \times m}$ is the covariance matrix of the sensor noise. Let m_i be the width of the i^{th} dimension in the n-dimensional

state space, then the discrete grid $\mathbf{X} \in \mathbb{R}^{m_1 \times m_2 \times \ldots \times m_n}$ of all expected possible values of the state space is used to evaluate the measurement equation. (For a large number of grid points, this calculation may be computationally intensive.)

2.3.2 Update step (Bayes' theorem)

Bayes' formula allows each new measurement and its likelihood function Eqn. (2.6) to be combined with the prior estimate, yielding the posterior estimate. Let $\mathbf{Y}_k$ be the set of measurements at time t_k, with $k = 1, 2, \ldots$. Then,

$$\pi(\mathbf{X}|\mathbf{Y}_k, \ldots, \mathbf{Y}_1) = \kappa\pi(\mathbf{Y}_k|\mathbf{X})\pi(\mathbf{X}|\mathbf{Y}_{k-1}, \ldots, \mathbf{Y}_1),$$

where κ is a normalizing factor to ensure the posterior integrates to one. After the incorporation of each new measurement, the posterior becomes the prior for the next time step. For the initial time step, we choose a uniform prior. The notation $\pi(\mathbf{X}|\mathbf{Y})$ is used for the posterior $\pi(\mathbf{X}|\mathbf{Y}_k, \ldots, \mathbf{Y}_1)$ at an arbitrary value of k.

2.3.3 Forecast step

The posterior estimate $\pi(\mathbf{X}|\mathbf{Y})$ is an n-dimensional matrix with each dimension corresponding to one of the states in the parameter space. The width m_i of each dimension is determined by how fine a grid is chosen for the Bayesian filter. The computational time needed for each time step increases with the size of $\pi(\mathbf{X}|\mathbf{Y})$. The time evolution of the posterior (in order to become the prior of the next time step) is accomplished by shifting the values of the PDF according to the continuous dynamics of the states.

2.3.4 Process noise

Process noise is modeled by convolving the PDF with an n-dimensional, zero-mean Gaussian kernel as a numerical approximation of the Fokker-Planck equation with diffusion only [103]. This operation has a blurring effect on the PDF as time goes on. In the absence of new measurements, the PDF becomes uniform as time goes to infinity.

2.4 Probability theory

The techniques in this manuscript also require many tools from probability theory [104], which we now present for completeness. The probability that a random variable X has value less than x is described by the cumulative distribution function $F_X(x) = P(X \leq x)$. The probability density function of the same random variable describes how often values occur and is given by $f_X(x) = \mathrm{d}F_X(x)/\mathrm{d}x$. Many techniques and toolboxes exist for fitting probability density functions to a data set [105, 106].

The expected value of a random variable X with probability density $f_X(x)$ is [104]

$$E[X] = \int_{-\infty}^{\infty} x f_X(x) \mathrm{d}x. \tag{2.7}$$

The expected value of a function $Y = h(X)$ of random variable X with probability density $f_X(x)$ is [104]

$$E[Y] = \int_{-\infty}^{\infty} h(x) f_X(x) \mathrm{d}x. \tag{2.8}$$

The probability that random variable X is less than random variable Y is [104]

$$P(X \leq Y) = \int_{-\infty}^{\infty}\int_{-\infty}^{y} f_{XY}(x,y)\mathrm{d}x\mathrm{d}y, \tag{2.9}$$

where $f_{XY}(x,y)$ is the joint probability density function of X and Y. If X and Y are independent random variables, then [104]

$$f_{XY}(x,y) = f_X(x)f_Y(y), \tag{2.10}$$

otherwise the joint probability density must account for cross-correlation between the two random variables. Similarly, if two events A and B are independent, then the probability of both A and B occurring at the same time is [104]

$$P(A \cap B) = P(A)P(B). \tag{2.11}$$

The probability density function for the random variable $Z = c_1X + c_2Y$, where c_1 and c_2 are known scalar values, is [104]

$$f_Z(z) = \frac{1}{\mid c_1 \mid}\int_{-\infty}^{\infty} f_X\left(\frac{1}{c_1}z - \frac{c_2}{c_1}y\right) f_Y(y)\mathrm{d}y. \tag{2.12}$$

The joint PDF of the linear combination of two random variables $V = aX + bY$ and $W = cX + dY$ is [107]

$$f_{VW}(v,w) = \frac{1}{ad-bc} f_{XY}\left(\frac{dv-bw}{ad-bc}, \frac{-cv+aw}{ad-bc}\right). \tag{2.13}$$

We now turn to two results not found in literature but necessary for subsequent chapters.

2.4.1 Expected value of an auxiliary function

Using the bivariate extension of Eqn. (2.8), the independence of X and Y with Eqn. (2.10), and Eqn. (2.9) the expected value of

$$h(X,Y) = \begin{cases} g(Y) \text{ if } X \leq Y, \\ \\ 0 \qquad \text{otherwise} \end{cases}$$

is

$$\begin{aligned} E[h(X,Y)] &= \int_{-\infty}^{\infty}\int_{-\infty}^{\infty} h(x,y) f_{XY}(x,y) \mathrm{d}x\mathrm{d}y \\ &= \int_{-\infty}^{\infty}\int_{-\infty}^{\infty} h(x,y) f_X(x) f_Y(y) \mathrm{d}x\mathrm{d}y \\ &= \begin{cases} \int_{-\infty}^{\infty}\int_{-\infty}^{\infty} g(y) f_X(x) f_Y(y) \mathrm{d}x\mathrm{d}y \text{ if } X \leq Y \\ \\ 0 \qquad \text{otherwise} \end{cases} \\ &= \int_{-\infty}^{\infty}\int_{-\infty}^{y} g(y) f_X(x) f_Y(y) \mathrm{d}x\mathrm{d}y \\ &= \int_{-\infty}^{\infty} g(y) f_Y(y) \left(\int_{-\infty}^{y} f_X(x) \mathrm{d}x \right) \mathrm{d}y. \end{aligned}$$

And so,

$$E[h(X,Y)] = \int_{-\infty}^{\infty} g(y) f_Y(y) \left(\int_{-\infty}^{y} f_X(x) \mathrm{d}x \right) \mathrm{d}y. \tag{2.14}$$

2.4.2 Minimum of two random variables

Given a random variable $Z = \min(X,Y)$, let us compute $f_Z(z)$. We first state that from the definition of a CDF $F_Z(z) = P[\min(X,Y) \leq z]$. The event

$\min(X, Y) \leq z$ is true if either $X \leq z$ or $Y \leq z$. In set notation,

$$\begin{aligned} F_Z(z) &= P[\min(X, Y) \leq z] \\ &= P[X \leq z \cup Y \leq z] \\ &= P[X \leq z] + P[Y \leq z] - P[X \leq z \cap Y \leq z] \\ &= F_X(z) + F_Y(z) - F_{XY}(z, z), \end{aligned}$$

where the third line is a direct application of the inclusion-exclusion principle which states that for two events A and B, $P[A \cup B] = P[A] + P[B] - P[A \cap B]$ [104]. To find the PDF from this CDF, we take the derivative with respect to z,

$$f_Z(z) = \frac{\mathrm{d}F_z(z)}{\mathrm{d}z} = f_X(z) + f_Y(z) - \frac{\mathrm{d}}{\mathrm{d}z} F_{XY}(z, z),$$

where

$$\begin{aligned} \frac{d}{dz} F_{XY}(z, z) &= \frac{\mathrm{d}}{\mathrm{d}z} \int_{-\infty}^{z}\int_{-\infty}^{z} f_{XY}(v, w)\mathrm{d}v\mathrm{d}w \\ &= \int_{-\infty}^{z} f_{XY}(z, w)\mathrm{d}w + \int_{-\infty}^{z} f_{XY}(v, z)\mathrm{d}v \\ &= \int_{-\infty}^{z} \left(f_{XY}(z, w) + f_{XY}(w, z)\right) \mathrm{d}w. \end{aligned}$$

Using the definition of the marginal densities f_X and f_Y allows further simplification,

$$\begin{aligned} f_Z(z) &= f_X(z) + f_Y(z) - \int_{-\infty}^{z} \left(f_{XY}(z, w) + f_{XY}(w, z)\right) \mathrm{d}w \\ &= \int_{-\infty}^{\infty} f_{XY}(z, w)\mathrm{d}w + \int_{-\infty}^{\infty} f_{XY}(w, z)\mathrm{d}w - \int_{-\infty}^{z} \left(f_{XY}(z, w) + f_{XY}(w, z)\right) \mathrm{d}w \\ &= \int_{z}^{\infty} \left(f_{XY}(z, w) + f_{XY}(w, z)\right) \mathrm{d}w. \end{aligned}$$

And so, the probability density of a random variable $Z = \min(X, Y)$ is (see Section 2.4.2)

$$f_Z(z) = \int_z^\infty \left(f_{XY}(z, w) + f_{XY}(w, z)\right) \mathrm{d}w. \tag{2.15}$$

This two results are included here as background as they are a straightforward application of probability theory that are both necessary to the work in later chapters and demonstrates how to derive probabilistic relationships.

2.5 Pursuit tactics

Literature on pursuit is multi-disciplinary, with works coming from both the animal behavior [12, 13, 21, 108] and missile guidance [20, 43, 109] communities. Due to this mixing of disciplines and a lack of formalization in the field, there are many (sometimes conflicting) terms used to describe various pursuit tactics. In *pure pursuit*, also sometimes called *tracking* or *classical pursuit*, a pursuer aligns its velocity vector with the line of sight (LOS), which is the vector from the pursuer to the target's current location and is used by many predators [11, 20].

In *deviated pure pursuit* (DPP) (i.e., *constant bearing pursuit* or *constant aspect pursuit*), the pursuer aligns its velocity vector a fixed angle away from the LOS such that it leads (or lags) the target. Certain fish [108], insects [11], dogs [8], and humans [9] exhibit this tactic in their pursuit trajectories. The special case where the target is not turning or changing speed and the pursuer's lead angle is such that it moves in a straight line for the entire pursuit phase is sometimes called *interception*.

In *constant absolute target direction* (CATD) *pursuit* (also known as *motion camouflage*, *parallel navigation*, or *constant bearing*), the pursuer moves in such a way that the LOS angle stays fixed with respect to some inertial reference frame. This tactic has the effect of masking the pursuer's transverse movement from the perspective of the target, because the pursuer appears only to increase in size. Certain dragonflies [12], bats [13], and falcons [110] use this tactic. In the case of a non-manuevering target, CATD pursuit is equivalent to constant bearing pursuit, but the converse is true only in the case of interception. A common technique to actualize one of these geometrical tactics into a control law for a physical system with dynamics is proportional navigation [43], though other techniques exist [20, 111].

Chapter 3: Probabilistic analytical modeling of predator-prey interactions

This chapter presents a method called probabilistic analytical modeling (PAM). This technique fills a gap in the current state of the art for pursuit modeling from experimental data (see Section 1.2.1). PAM allows researchers to determine which factors are most critical to survival by analyzing the kinematic time series of their pursuit trajectories. The use of this method is demonstrated by two case studies. The chapter proceeds as follows. Section 3.1 introduces two case studies of fish predator-prey interactions. Section 3.2 presents the general PAM approach used to analyze each experimental data set in order to determine the most important tactical factors in predator-prey interactions. Section 3.3 applies PAM to a case study of the pursuit tactics of bluefish predators and Section 3.4 uses the methodology on a case study on the evasion tactics of zebrafish prey. Although the primary data analyzed in these two cases is based on two previous experimental studies [14, 42], the results reported here can be verified using the statistical data provided in this work. Section 3.5 summarizes the results and describes ongoing work.

3.1 Case study background

The techniques developed in this chapter are applied to two sets of case study data of pursuit by fish. The data were not gathered as part of this thesis and I played no role in the experiments to do so. In the context of this work, it is only the final kinematic time series data which of interest. This section provides a brief background on how the data were collected to provide valuable context for the later sections.

3.1.1 Case study 1: bluefish

Piscivorous interactions may largely be described by two-dimensional kinematics, but exhibit a diversity of tactics that have the potential to vary with the habitat and the physiology of a fish species. Bluefish (*Pomatomus saltatrix*) are voracious pelagic fish predators that pursue prey at high speed. This species exhibits predatory behavior in an aquarium with motion that is largely two dimensional and is therefore conducive to single-camera kinematic measurements. As detailed in a separate study [14], the high-speed swimming kinematics were measured for bluefish ($\sim 30\,\text{cm}$ in length) as they preyed upon smaller prey fish, mummichog (*Fundulus heteroclitus*, $\sim 5\,\text{cm}$). These data were gathered by Dr. Matt McHenry and Dr. James Liao at the University of Florida. The details of these experiments are beyond the scope of this thesis, but can be found in Ref. [14]. With that said, a brief description is necessary to understand the modeling work done later in this chapter.

These experiments introduced an individual prey into the center of a large

cylindrical aquarium (diameter = 6 m), which contained all of the predators. Kinematic measurements were performed for the prey and predator that first struck at the prey. Inherent in this decision is the assumption that the successful predator's trajectory is not affected by the presence of other predators in the area. (The validity of this assumption is addressed in Section 3.3.1.) These measurements consisted of a manual frame-by-frame tracking of the rostrum of each fish from the moment that both appeared in the camera's field of view until the predator's strike. The mummichog did not attempt an escape when pursued by bluefish, but rather maintained a relatively straight path and consistent speed. The trajectories of predator and prey were recorded for 70 experimental trials. The dynamical model of bluefish predation presented in Section 3.3 takes advantage of the largely non-maneuvering prey, allowing for a deviated pure pursuit representation with only the line-of-sight range and angle as state variables.

3.1.2 Case study 2: zebrafish

Under laboratory conditions, zebrafish adults ($\sim$ 2.5 cm) prey on larvae ($\sim$ 4 mm) of the same species [112]. However, unlike the mummichog preyed upon by bluefish, zebrafish larvae generally remain stationary until initiating an escape response at a certain point during the predator's approach [30]. This response allows for a consideration of the evasion tactic of a prey fish that can be measured and modeled. The kinematic data were previously reported from experiments in a hemispherical aquarium (diameter = 8.5 cm), where the predator attempted multiple

strikes at the prey until successful, See Ref. [42]. Within one second of initiating an escape, the prey ceased swimming and were stimulated to escape again when approached by the predator. The predator approached the prey at a constant speed, well below the prey's maximum escape speed. This approach was consistent with a pure-pursuit tactic, such that the predator's heading was directed towards the instantaneous position of the prey. These interactions repeated for as many as twenty approaches in experiments performed in a relatively small aquarium and were previously characterized by iterating a model of a single interaction using a Monte Carlo technique [42].

3.2 General method

We now present the general PAM procedure used to determine which parameters in a given predator-prey interaction are most critical to survival.

1. Choosing a dynamic model. The first step is to analyze the experimental kinematic data to determine the dynamics of the system. A catalog of standard pursuit tactics and their dynamical models may be useful [20, 21], see Section 2.5. In more complicated cases where the prey is highly responsive to the actions of the predator, a differential-game setting may be required [67].

The chosen model need not exactly predict the actions of the predator and prey seen in experiments, but it should capture the essential attributes of their behavior. For example, many of the standard pursuit models assume constant speed of the predator and prey, which is not the case in a biological system. This assumption

may be tolerable (as with the bluefish case study in Section 3.3) unless either the predator or prey exhibit some specific speed-changing behavior (such as the starting and stopping of the larvae's motion in response to the zebrafish in Section 3.4).

If the predator-prey interaction is well modeled by a dynamical system from literature (as it is in Section 3.3), then deriving an analytical expression for the key metric may be trivial or already available. If a more non-traditional model is required to describe the behavior (as in Section 3.4), then the development of the model and the derivation of the expression for the key metric may be an iterative process.

2. Fitting probability densities to the experimental data. Once a model has been selected, each of the parameters in that model are fit from the experimentally observed data set. These parameters may include predator or prey speeds, angles, capture rates, etc. It may be advantageous to model certain parameters as deterministic and others as probabilistic to simplify the expression of the expected value of the key metric. For example, in Section 3.3, the predator and prey speeds are treated as random variables, whereas in Section 3.4 they are treated as deterministic because more interesting behavior in the prey species arises from variations in sensing range.

Many techniques exist for fitting probability density functions (PDFs) to data sets [105, 106]. A particular form of the PDF for each parameter is not required for the following steps (e.g., it need not be normally distributed) and that fact is a strength of this work. In certain cases, deterministic functions may be fit to data,

like the success rate of strikes as a function of distance in Section 3.4.

3. Choosing a key metric. The key metric will be a measure of the success of the predator or prey in either the predation or escape behavior. In many cases, such as for probability of capture, the predator's goal is to maximize the metric and the prey's goal is to minimize it.

An analytical expression of the key metric is required to calculate its expected value. The expression is derived from the model of the predator/prey interaction and both the expression itself and the steps to derive the expression may be unique to each model and metric. Some component of the system dynamics may need to be directly integrated and numerical integration may not be sufficient. For this reason, concurrent or iterative development of the model and the expression of the key metric may be required to modify the model into an integrable form.

4. Finding the expected value of the key metric. Depending on the form of the expression of the key metric, a direct application of the multivariate extension of equation (2.8) will provide the expected value, as is the case in Section 3.3. For more complicated expressions, something akin to what is done in Section 3.4 may be required, where conditional statements are incorporated into the calculation of the expected value.

5. Parameter perturbation analysis. To study the relative effect each of the parameters in the model has on the expected value of the key metric, we employ a scheme similar to that used in [42], where the expected values of the probabilistic

parameters are varied by shifting the terms within the PDFs. In [42], the varied PDFs were tested in a Monte Carlo framework to recalculate the expected value of the key metric from a multitude of simulations. In the work described here, the expression for the expected value of the key metric need only be re-evaluted with the varied PDFs, taking advantage of the inclusion of the system dynamics in the key metric.

The expected value of the key metric as a function of the change of each parameter from its nominal value reveals which parameter most greatly influences the key metric and, therefore, the survival of either the predator or prey. Though the PAM technique was developed for predator-prey interactions, it is applicable to examine metrics for any dynamical process with natural variation in the parameters.

3.3 Bluefish case study

This section describes the application of PAM (Section 3.2) to examine the predatory behavior of bluefish as they preyed upon mummichog [14]. Section 3.1.1 provides background on the case study data examined here.

3.3.1 Deviated pure pursuit model

Figure 3.1 defines the planar pursuit geometry used in this case study. The vector of length r between the predator and the prey is known as the line of sight and is inclined from the inertial reference frame by an angle λ. The predator's velocity vector $\mathbf{v}_p$ is inclined from the line of sight by the pursuit (deviation) angle

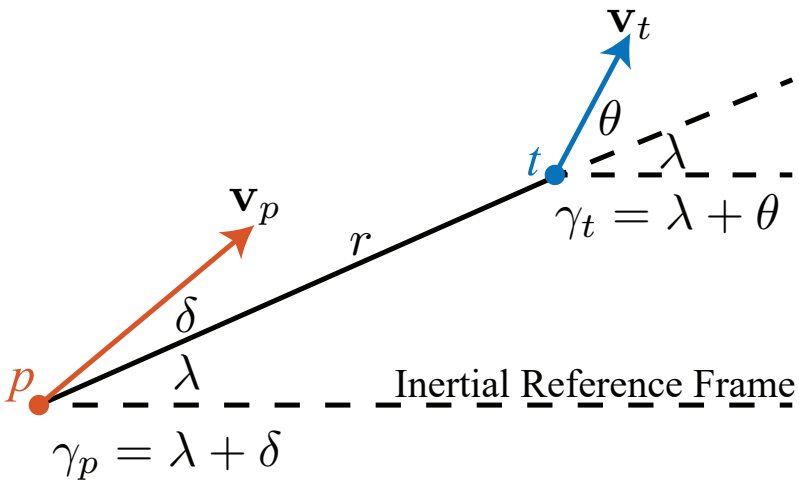

Figure 3.1: Pursuit kinematics for predator (p, red) and prey (t, blue). The swimming direction of both animals are defined by the velocity of prey ($\mathbf{v}_t$) and predator ($\mathbf{v}_p$), relative to the range vector (r, at angle λ), specified by the bearing of predator (δ) and prey (θ). The heading (γ) of each animal is defined relative to the inertial reference frame.

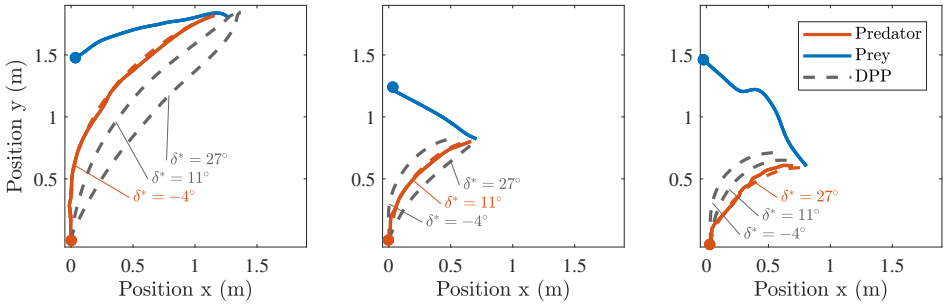

Figure 3.2: Trajectories of predator and prey for three representative experiments. Dotted trajectories are those generated by the deviated pure pursuit (DPP) control (Eqn. 3.1) with $\delta^* = -4°, 11°,$ and $27°$, which were the best match for these trials from left to right, respectively.

δ and likewise the prey's velocity $\mathbf{v}_t$ is inclined by θ. The velocity magnitudes (i.e., speeds) are denoted $v_p > 0$ and $v_t > 0$. The angle of the velocity vectors from the inertial frame are γ_p and γ_t for the predator and prey, respectively.

To verify that the bluefish are using DPP, we compared simulations of the DPP dynamics to the experimental trajectories. Comparisons were very favorable even without accounting for predator-predator interactions. Figure 3.2 shows three examples of these comparisons, where the simulated trajectories obey the following dynamics:

$$\begin{aligned} \dot{x}_p &= v_p \cos\gamma_p \\ \dot{y}_p &= v_p \sin\gamma_p \\ \dot{\gamma}_p &= k(\lambda + \delta^* - \gamma_p) = k(\delta^* - \delta) \\ v_p(t) &= \text{measured predator speed at time } t, \end{aligned} \tag{3.1}$$

where (x_p, y_p) is the predator position, $k > 0$ is the scalar feedback gain, and δ^*

is the desired pursuit angle. With γ_p as a control input, these dynamics use only the geometric angle δ as feedback, a value that may be available to the bluefish from their visual system [108]. In the experimental data, the predator's speed v_p varies within a pursuit. Thus, in the simulated trajectories (e.g., Fig. 3.2) the DPP tactic is used for the predator steering, given the experimentally measured values of speed. The particular pursuit angle δ^* used in Eqn. (3.1) is unique to each trial and was found by sweeping through values $\delta^* \in (-\pi, \pi]$ and choosing the δ^* that best matched the experimental trajectories in the least-squares sense.

3.3.2 Experimental data fitting

Three probabilistic parameters are needed to calculate the expected value of the time to capture as seen below in the key metric section. The pursuit angle δ as calculated by the geometry in Fig. 3.1 is well represented by a normal distribution. However, since $\delta \in (-\pi, \pi]$, we use a von Mises distribution, which is often referred to as the wrapped normal distribution. Figure 3.3 shows two PDFs given by

$$f_\Delta(\delta) = \frac{1}{2\pi I_0(\kappa_\delta)} \exp\left(\kappa_\delta \cos(\delta - \mu_\delta)\right), \tag{3.2}$$

where I_0 is the modified Bessel function of order 0, μ_δ is the mean value and $\kappa_\delta \geq 0$ is a term that represents the spread of the distribution with $\kappa_\delta = 0$ corresponding to a uniform distribution. The first PDF is fit from the geometrical $\delta(t)$ at every time step across all experiments and the second is fit from the δ^* value associated with each trial from dynamics Eqn. (3.1). The $\delta(t)$ PDF has higher variance because the bluefish do not perfectly track the δ^* values and oscillate about them in each

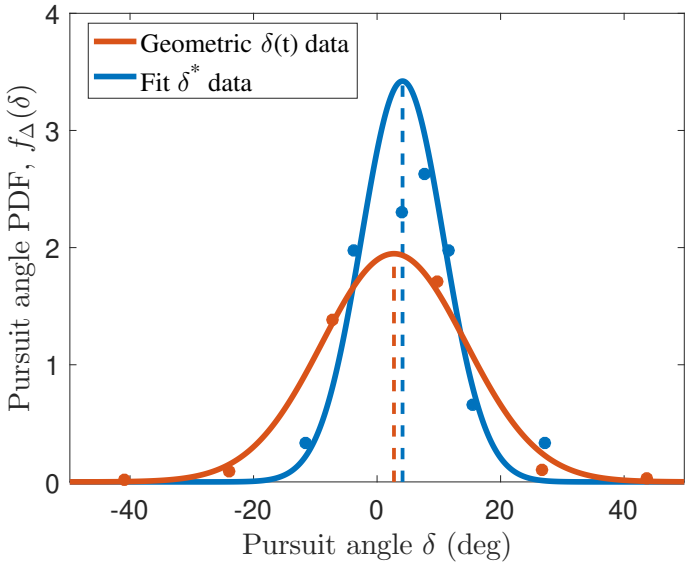

Figure 3.3: PDF for the pursuit angle δ fit from experimental data. Geometric $\delta(t)$ data are determined from the predator heading γ_p and line of sight angle λ at each time step. Fit δ^* data are the angles in dynamics (3.1) that best match the fish trajectories.

trial. Values for the δ^* fit parameters are used in this case study (the result is nearly identical in either case) and are given in Table 3.1.

The probability densities for the speed of the predator and prey are not independent because although the prey is largely unresponsive to the actions of the predator, it is unclear whether or not the predator adjusts its speed in response to the prey. A bivariate log-normal density is fit to the data set of (v_p, v_t) pairs taken at every time step across all experimental trials. Let $L(v_p, v_t, \mu_v) = [\ln v_p, \ln v_t]^\intercal - \mu_v$. Figure 3.4 shows the joint PDF

$$f_{V_p,V_t}(v_p, v_t) = \frac{1}{2\pi\sqrt{\det \Sigma_v}} \exp\left(-\frac{1}{2} L(v_p, v_t, \mu_v)^\intercal \Sigma_v^{-1} L(v_p, v_t, \mu_v)\right), \tag{3.3}$$

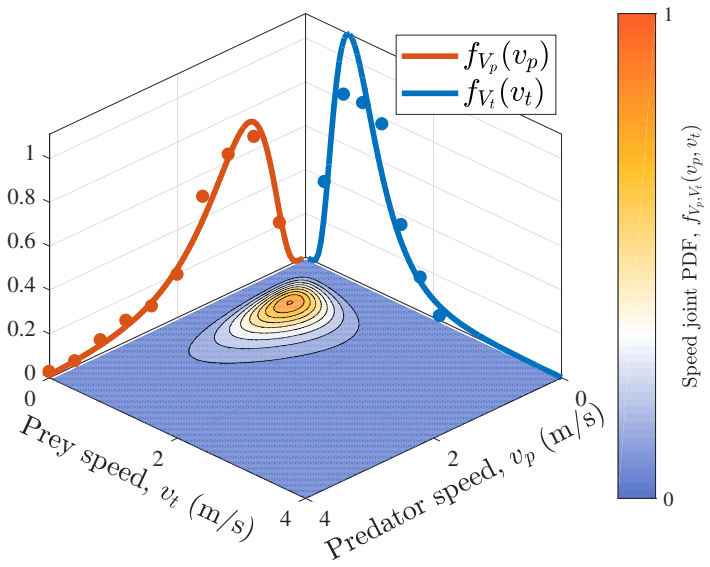

Figure 3.4: Joint PDF for predator speed v_p and prey speed v_t shown as a contour plot. Marginal PDFs are shown in blue and orange in the vertical axis.

where μ_v and Σ_v are given in Table 3.1.

3.3.3 Key metric: expected time to capture

In the experimental setup, many bluefish simultaneously begin pursuit when the prey fundulus is dropped into the arena. Since the bluefish are nearly always successful in capturing the prey once they reach it, the first predator to reach the prey received the reward. Therefore we choose the key metric to be the time to capture.

Assume a constant speed for the predator and a non-maneuvering prey, meaning the prey moves with constant speed and direction. Though this is not strictly the case for the experimental data, we seek to examine the effect of pursuit angle δ and so we do not study the effect of changing speed during a pursuit. Addition-

Table 3.1: Parameters of the bluefish pursuit model. Pursuit angle δ has a von Mises distribution with PDF $f_\Delta(\delta)$. The predator speed v_p and prey speed v_t form a bivariate lognormal PDF $f_{V_p,V_t}(v_p, v_t)$. The given parameters correspond to mean speeds of 1.38 m/s and 0.95 m/s for the predator and prey, respectively. Intial conditions are determinisitic with nominal values as given.

Probabilistic parameters	δ	Pursuit angle	$\mu_\delta = 0.0720$ rad $\kappa_\delta = 73.8049$
	v_p	Predator speed	$\mu_v = \begin{bmatrix} 0.1565 \\ -0.5286 \end{bmatrix}$
	v_t	Prey speed	$\Sigma_v = \begin{bmatrix} 0.2849 & 0.1070 \\ 0.1070 & 0.9147 \end{bmatrix}$
Initial conditions	r_0	Range	1 m
	θ_0	Prey heading	$\pi/2$ rad

ally, assume that the predator maintains a constant pursuit angle δ throughout its trajectory. The predator speed, prey speed, and pursuit angle are considered as random variables.

With these assumptions, the dynamics of the DPP system in terms of the rate of change of the line-of-sight range r and angle λ shown in Fig. 3.1 are [20]

$$\dot{r} = v_t \cos\theta - v_p \cos\delta$$
$$-\dot{\lambda} = \dot{\theta} = \frac{1}{r}\left(-v_t \sin\theta + v_p \sin\delta\right),$$

where $\dot{\lambda} = -\dot{\theta}$, because the prey is non-maneuvering. Using these dynamics, the time to capture is [20]

$$t_c(r_0, \theta_0, v_p, v_t, \delta) = r_0 \frac{v_p + v_t \cos(\theta_0 + \delta)}{(v_p^2 - v_t^2)\cos\delta}. \tag{3.4}$$

For two random variables X and Y and a nonlinear function $Z = g(X, Y,)$ it is not true in general that $\mathrm{E}[Z] = g(\mathrm{E}[X], \mathrm{E}[Y])$ [104]. Since three of the parameters in Eqn. (3.4) are random variables, we must instead calculate the expected value by using the multivariate extension of Eqn. (2.8):

$$\mathrm{E}[T_c] = \iiint_{-\infty}^{\infty} t_c(r_0, \theta_0, v_p, v_t, \delta) f_{V_p, V_t}(v_p, v_t) f_\Delta(\delta) dv_p dv_t d\delta, \tag{3.5}$$

which assumes δ is independent from v_p and v_t.

3.3.4 Non-optimallity of pursuit angle

To determine which parameters have the greatest effect on the time to capture t_c, we use the technique described in Section 3.2. Figure 3.5(a) shows the result

of this process, in comparison to a deterministic evaluation of Eq. (3.4) directly using E[V_p], E[V_t], and E[Δ]. Increasing the prey speed or decreasing the predator speed has a much less pronounced effect on E[T_c] as compared to the deterministic technique. This effect is because the deterministic case considers only single values of v_p or v_t that may become very close as either is varied, causing t_c to become large. The probabilistic case balances this effect by considering all possible values of v_p and v_t according to their likelihood from Eqn. (3.3). Even if $E[V_p]$ and $E[V_t]$ are very close, there are still many other values that are accounted for by Eqn. (3.5). The nominal initial conditions used in Fig. 3.5 are $r_0 = 1$ m and $\theta_0 = \pi/2$ rad.

Figure 3.5(b) shows an extended variation of the pursuit angle δ from its small nominal value of 4.13°. We see that there exists an optimal pursuit angle much higher than the pursuit angle most often used by the bluefish. This optimal angle corresponds to the intercept tactic (see Section 2.5). Since the bluefish do not appear to be optimizing this metric, alternative explanations are suggested below.

3.3.5 Discussion

The deterministic versus probabilistic study of the effect of varying the parameters yields different, yet qualitatively consistent results as seen in Fig. 3.5. Though the unperturbed (0% change from experimental parameters) value of time to capture is incorrect, the deterministic study yields the correct trends near the nominal values, but does not accurately predict time to capture as the parameters are varied further. For larger deviations, the probabilistic study shows the expected

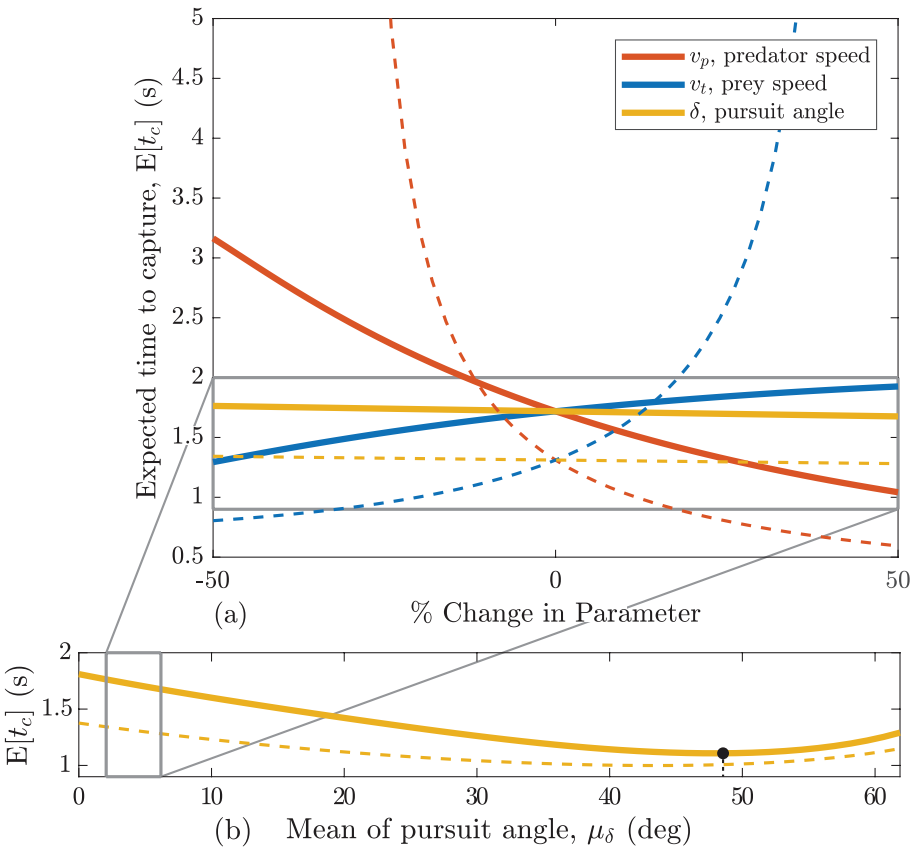

Figure 3.5: (a) Probabilistic parameter variation for the bluefish case study (solid). Dashed lines are those from deterministic perturbation analysis. (b) Extended variation for the pursuit angle δ with the black circle showing the minimum time to capture. The region outlined in gray is shown in (a).

effect on the time to capture t_c.

As seen in the δ curve in Fig. 3.5(a), increasing/decreasing the pursuit angle δ has very little effect on the time to capture, because the bluefish most often use small, but non-zero, pursuit angles (Fig. 3.3). Why the bluefish use a deviated pure pursuit (DPP) tactic over a pure pursuit (PP) tactic (the $\delta = 0$ case) when it yields such small changes in capture time is not clear. The analysis shows that a

time-optimal pursuit angle exists (Fig. 3.5(b)), though the bluefish operate far from its value. DPP may present a tactical advantage for a more evasive prey than the prey presently considered. For example, a faster prey might prompt the bluefish to increase δ such that their swimming trajectory more closely resembles the CATD tactic (see Section 2.5). Alternatively, DPP may indicate a constraint or bias on the sensorimotor system of the bluefish. Bluefish may more quickly process the position of the prey when it is present in the visual field of a single eye, which is facilitated by a non-zero value for δ. In most cases, the predator chose to fix the prey in the eye on the side that leads the prey velocity ($\delta > 0$), which does slightly reduce capture time compared to the negative of that angle.

3.4 Zebrafish case study

The second PAM case study considers prey evasion tactics in larval zebrafish pursued by adult zebrafish [42]. The prey in this case attempts to escape by accelerating to a speed that is faster than the predator, as described in Section 3.1.2.

To calculate the key metric for this case study, a one-dimensional hybrid system model of the dynamics is formulated. The continuous part of the hybrid system describes the approach of the predator and the escape behavior of the prey, whereas the discrete part handles the switching of parameters between repeated approaches and the onset of escaping behavior.

A hybrid system is a dynamical system that has a combination of continuous- and discrete-time behavior [113, 114]. Hybrid systems often involve the discrete

switching between sets of dynamics, such as a thermostat, or a discrete jump in states, such as a bouncing ball. Stochastic hybrid systems are those that have non-deterministic dynamics or non-deterministic conditions on the state switching [115]. Here, a hybrid system is needed to model the switch between freezing and escaping behavior.

3.4.1 Hybrid dynamics model for repeated escape

Among pursuit tactics [20–22], pure pursuit is best represented by a one-dimensional model since the predator always moves directly towards the prey and the distance between them is of prime importance.

The distance between the predator and prey at time t is $r(t)$. The predator will attempt a strike if $r(t)$ is less than the strike distance s. The prey begins its escape if $r(t)$ is less than its sensing range (flush distance) l. The prey escapes for η seconds, reaching its maximum speed v_t at a fraction χ of its escape time. $C(s)$ is the probability of a successful strike as a function of strike distance s and is experimentally determined. Table 3.2 summarizes the parameters used in the model and includes their values for this case study.

Assume that the predator reaches its maximum speed v_p sufficiently far from the prey so that predator acceleration may be ignored. The prey remains stationary until it detects the predator, that is, until $r(t) \leq l$, the sensing distance of the prey. Once the predator is detected, the prey escapes with a sawtooth velocity profile, as shown in Fig. 3.6. This type of velocity profile is general to many startle responses

Table 3.2: Parameters of the model for the zebrafish case study. Probabilistic parameters have log-normal probability density functions $f_S(s)$, $f_L(l)$, and $f_H(\eta)$. $C(s)$ is a sigmoidal function of the form $C(s) = [1 + \exp(-\rho(s - \rho_0))]^{-1}$.

Probabilistic parameters	s	Strike distance of predator	$\mu_s = -4.980$ $\sigma_s = 0.448$
	l	Sensing distance of prey	$\mu_l = -4.546$ $\sigma_l = 0.587$
	η	Escape duration of prey	$\mu_\eta = -1.369$ $\sigma_\eta = 0.552$
Deterministic parameters	v_p v_t χ	Predator speed Maximum prey speed Fraction of η when u is reached	0.13 m/s 0.4 m/s 0.2
Deterministic function	$C(s)$	Strike success chance	$\rho = -0.573$ $\rho_0 = 5.20$

seen in nature where the prey quickly flees only to come to rest again a short time later [42].

Figure 3.7 illustrates the hybrid dynamics of this non-deterministic system for one or more approaches. The approach number $a_n = n$ counts the number of times the prey has begun escaping from the predator. The time since observation begins is t. The time from when approach a_n begins is $t^{(n)} = t - t_0^{(n)}$, where $t_0^{(n)}$ is the

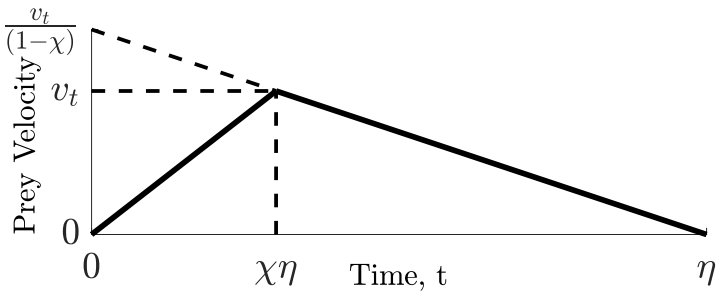

Figure 3.6: Prey velocity profile (v_t) after detecting the predator. The prey escape duration is η; it reaches its maximum speed at fraction χ of the escape duration.

time when a_n increments. Additionally, on approach n, each of the probabilistic parameters $s^{(n)}$, $l^{(n)}$, and $\eta^{(n)}$ are redrawn from their densities, $f_S(s)$, $f_L(l)$, and $f_H(\eta)$, respectively. Figure 3.8 shows a sample trajectory of the dynamics using the case-study data.

3.4.2 Experimental data fitting

All of the parameters in Table 3.2 were experimentally determined or fit in [42]. The probabilistic parameters have log-normal PDFs with the form

$$f_X(x) = \frac{1}{x\sqrt{2\pi\sigma_x^2}} \exp\left(-\frac{(\ln x - \mu_x)^2}{2\sigma_x^2}\right).$$

The strike probability of success has the form $C(s) = [1+\exp(-\rho(s-\rho_0))]^{-1}$. Though the experiments showed some variation in the maximum speed of the predator and prey, here they are treated as constants because we seek to study the more interesting fleeing behavior of the prey.

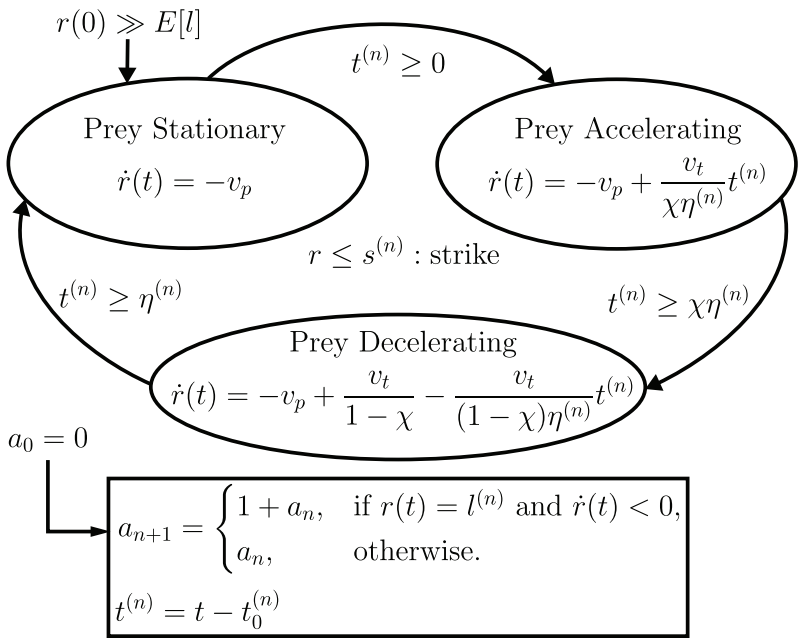

Figure 3.7: Non-deterministic hybrid system model of predator-prey interaction. The box represents the discrete dynamics and the ellipses represent continuous dynamics. Probabilistic variables are redrawn from their respective PDFs each time the approach number a_n is incremented.

3.4.3 Key metric: expected probability of capture

Probability of capture has relevance to both the predator and prey, one seeking to maximize it and the other to minimize. The goal is now to analyze the hybrid system to derive an expression for the expected value of the probability of capture on approach and the probability of survival after n approaches.

For the prey to be captured, two conditions must be met. First, the minimum distance $\underline{r}^{(n)}$ must be less than the strike distance. If $\underline{r}^{(n)}$ is not less than $s^{(n)}$, then no other point on the trajectory will be. This condition states that a strike will be

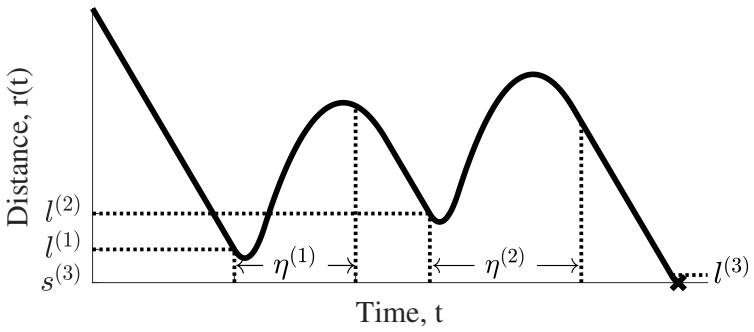

Figure 3.8: Sample trajectory of the simulated dynamics in Fig. 3.7 using the zebrafish case-study data and model. The prey begins escape three times before a strike occurs at the black $\times$.

attempted, though not where the strike will occur. Second, the strike must be successful. This condition is given by the function $C(s)$, which gives the probability of success of a strike at distance $s^{(n)}$. Thus for the predator-prey interaction described by the dynamics in Fig. 3.7, the probability of capture on approach is

$$P_{\text{CoA}} = E[C(s)], \text{ given } \underline{r} \leq s.$$

Critical to this analysis is finding the minimum distance $\underline{r}^{(n)}$ between the predator and prey. With the goal to find the minimum distance $\underline{r}$ on a single approach, we restrict our analysis to the interval $t^{(n)} \in [0, \eta^{(n)}]$. The first of two possibilities where r may achieve a minimum is $\underline{r_1}$ during the prey accelerating phase in Fig. 3.7, when $\dot{r} = 0$ at $t^{(n)} = v_p \chi \eta^{(n)} / v_t$. The second possibility is $\underline{r_2}$ during the prey decelerating phase in Fig. 3.7, which occurs at the end of the interval, $t^{(n)} = \eta^{(n)}$. The minimum on the interval is then $\underline{r} = \min(\underline{r_1}, \underline{r_2})$.

To find $\underline{r_1}$, from Fig. 3.7, we have

$$\dot{r}(t) = -v_p + \frac{v_t}{\chi\eta}t, \quad r(0) = l \tag{3.6}$$

on the interval $t \in [0, \chi\eta]$, where we dropped the superscripts on $t^{(n)}$, $\eta^{(n)}$, and $l^{(n)}$ as we are considering only a single approach and each approach is an independent event. Integrating directly and evaluating at $\underline{t} = v_p(\chi\eta/v_t)$, the local minimum is

$$\underline{r_1}(\eta, l) = -\frac{v_p^2\chi}{2v_t}\eta + l. \tag{3.7}$$

The second possible minimum, $\underline{r_2}$, occurs at the end of the entire escape phase shown in Fig. 3.6 at $\underline{t} = \eta$. The distance traveled by the predator and prey during this time are $v_p\eta$ and $v_t\eta/2$, so

$$\underline{r_2}(\eta, l) = \left(\frac{v_t}{2} - v_p\right)\eta + l, \tag{3.8}$$

The two possible minima $\underline{r_1}$ and $\underline{r_2}$ are each a linear combination of η and l, so the joint PDF is expressed in terms of $f_H(\eta)$ and $f_L(l)$ as (see Eq. 2.13)

$$f_{\underline{R_1R_2}}(\underline{r_1}, \underline{r_2}) = \frac{1}{ad-bc} f_H\left(\frac{d\underline{r_1} - b\underline{r_2}}{ad-bc}\right) f_L\left(\frac{-c\underline{r_1} + a\underline{r_2}}{ad-bc}\right), \tag{3.9}$$

where $a = -v_p^2\chi/2v_t$, $b = 1$, $c = v_t/2 - v_p$, and $d = 1$. The PDF of the minimum of $\underline{r_1}$ and $\underline{r_2}$ is found using Eqn. (2.15):

$$f_{\underline{R}}(\underline{r}) = \int_{\underline{r}}^{\infty} \left(f_{\underline{R_1R_2}}(\underline{r}, w) + f_{\underline{R_1R_2}}(w, \underline{r})\right) \mathrm{d}w, \tag{3.10}$$

The joint probability density function of $\underline{r}$ and s is $f_{\underline{R}S}(\underline{r}, s) = f_{\underline{R}}(\underline{r})f_S(s)$ [104], assuming the minimum distance and the strike distance are independent. The probability of capture $P_{\mathrm{CoA}} = E[\hat{C}(\underline{r}, s)]$, where $\hat{C}(\underline{r}, s)$ is an auxiliary function that

takes value $C(s)$, if $\underline{r} \leq s$, and 0 otherwise. From (2.14), we have the probability of capture on approach

$$P_{\text{CoA}} = \int_{-\infty}^{\infty} C(s) f_S(s) \left(\int_{-\infty}^{s} f_{\underline{R}}(\underline{r}) \mathrm{d}\underline{r} \right) \mathrm{d}s. \tag{3.11}$$

Equation (3.11) provides the probability that the prey is captured on a given approach of the predator. Applying this equation to the case-study data yields $P_{\text{CoA}} = 0.07$. As a check, the dynamics given in Fig. 3.7 were simulated until the result was invariant to the number of simulations and it was found that P_{CoA} matched the result from Eqn. (3.11). For each trial in the simulation, $r(t)$ was integrated using a first-order Euler method. To calculate P_{CoA}, the total number of captures was divided by the total number of trials in the simulation. Figure 3.9 shows the result of the Monte Carlo trials, where 100,000 trials were needed to converge to the output of the single equation Eqn. (3.11).

Assuming each approach is an independent event, the probability that the prey survives after n approaches is [104]

$$P_{\text{SnA}}(n) = (1 - P_{\text{CoA}})^n. \tag{3.12}$$

Equation (3.12) in conjunction with Eqn. (3.11) allows experimentally gathered PDFs of predator-prey parameters to be used to calculate the odds of prey survival after repeated approaches by the predator. Note that as $n \to \infty$, $P_{\text{SnA}}(n) \to 0$ and thus, in this model, the prey are always captured eventually.

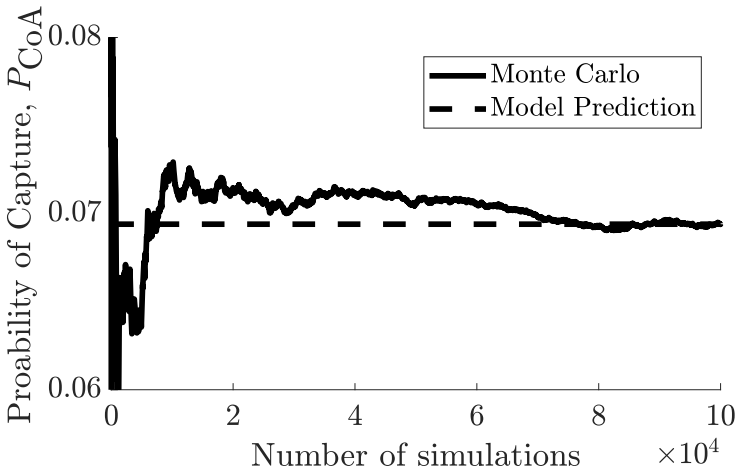

Figure 3.9: Monte Carlo simulation results of the dynamics in Section 3.4.1. The dashed line indicates the prediction of Eqn. (3.11).

3.4.4 Importance of sensing range

3.4.4.1 Parameter perturbation analysis

Equations (3.10) and (3.11) allow interrogation of experimentally gathered data to find which parameters are most important in the predator-prey interaction. By shifting the mean of the probabilistic parameters (or shifting the values of the deterministic parameters) and recalculating Eqn. (3.11), the most important parameters to prey survival become readily apparent.

Figure 3.10 shows the result of the perturbation analysis. Increasing sensing range l and maximum escape speed v_t increases the probability of survival of the prey. However, there is a larger increase seen when sensing range is increased rather than escape speed. Increasing escape duration η decreases probability of survival, likely because it takes the prey longer to reach its maximum speed (escape duration

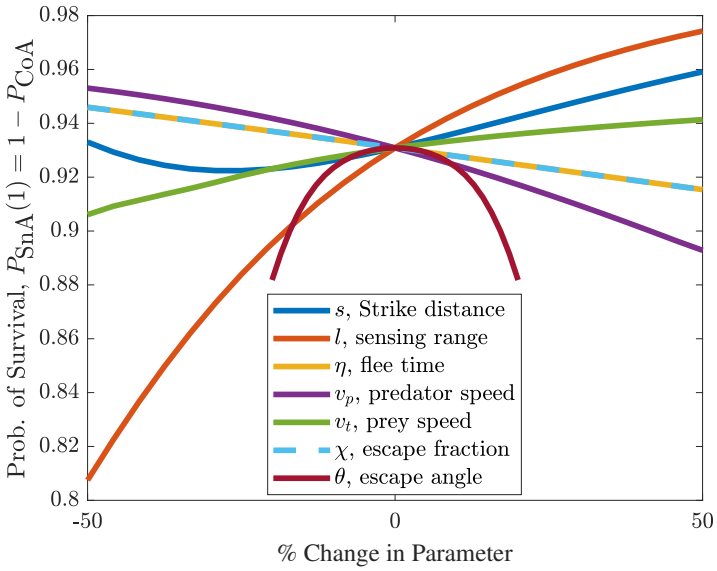

Figure 3.10: Probability of suvival $P_{\mathrm{SnA}}(1) = 1 - P_{\mathrm{CoA}}$ for $n = 1$ approach as the means of the parameter distributions are varied.

and maximum speed determine acceleration). Parameter χ, the fraction of the escape time at which the prey reaches its maximum speed, matches the result of varying η almost exactly because both terms determine the prey's acceleration on the first leg of its velocity profile.

When strike distance s is increased, the probability of survival also increases. In this case study, the decrease in probability of capture that results from the condition $\underline{r} \leq s$ is outweighed by the decrease in likelihood of a strike being successful at the increased range (capture probability $C(s)$ is much lower when striking from a farther distance). Decreasing s decreases prey survival only up until a point where the trend reverses. The probability densities interact such that the increased odds of a successful strike at a short distance eventually outweigh the chance that the prey escapes due to sensing the predator before it can strike.

3.4.4.2 Discussion

Trend-reversing behavior, such as is seen here when strike distance is varied, cannot be predicted from the dynamics of the non-deterministic hybrid system presented in Fig. 3.7 alone as it depends on the particular parameter PDFs. The ability to predict behavior of this type by combining experimentally fit PDFs with a model of the dynamics is a strength of the data-driven approach. In this case study, sensing range is pivotal to prey survival. Especially in the negative changes in l, there is a much larger decrease in survivability compared to the other parameters. These results agree with those of a comparable analysis performed by a Monte Carlo simulation [42], but were resolved here analytically.

The PAM method gives something more than agreement with numerical simulations for this case study: it explains *why* sensing range is most important. The derivation of the probability of capture revealed that it is imperative to increase the minimum distance if the prey wishes to survive. The analytical expressions Eqn. (3.7) and Eqn. (3.8) for the minimum distance show that it has a one-to-one correspondence with sensing range. (Compare this observation to the other parameters that enter the expressions multiplied by other factors.) To increase survivorship, natural selection would favor individuals with greater sensing range more so than greater speed. However, to account for additional features such as a requirement of the prey to feed or predators that have difficulty sensing motionless prey, the model used here is insufficient. Special consideration would be needed in that case, which adds complexity to the model formulation.

Figure 3.10 also includes a curve corresponding to varying escape angle θ from a nominal value of 2π, which corresponds to when the prey flees directly away from the predator. Since our dynamics model is one dimensional, a reasonable approximation to the two-dimensional concept of escape angle is to reduce the effective escape speed to $u_{\text{eff}} = u\cos\theta$. Note that in the model any variations away from direct escape result in lower chances of survival, something not seen in [42]. The choice to represent the pursuit in only the one-dimension r ignores any turning dynamics that may exist in the predators motion, i.e., it is always heading directly towards the prey. This choice neglects the potential tactic of the prey of changing its escape direction unexpectedly after each escape phase, thereby requiring the predator to change its orientation with some associated time delay corresponding to its turning dynamics. Expanding this model to include turning dynamics of the predator and thereby allowing an investigation of the benefit of unpredictability in the prey's escape angle is a suitable topic for future work.

3.5 Summary of chapter

This chapter models the tactical behavior of predator or prey with a novel combination of analytical mathematics and data-driven variability called probabilistic analytical modeling (PAM). Experimental measurements of kinematic features such as speed and flush distance combined with PAM predict the outcomes of biological events in ways that experiments or modeling alone cannot. The first case study showed that the trajectory of a bluefish predator may be predicted with a devi-

ated pure pursuit tactic. Analysis of this tactic revealed no substantial advantage compared to pure pursuit, indicating that the small, non-zero values for the pursuit angle observed in bluefish predation may indicate a sensorimotor bias or perhaps a tactical advantage not revealed by the prey species presently considered. The second case study on zebrafish predicted the survivorship of prey using a simple evasion algorithm. Analysis of this model was consistent with previous numerical results showing that sensing range is most important to survival among the behavioral parameters of the prey. In both case studies, PAM demonstrates the utility of a principled approach for understanding tactics in predation.

Beyond predator-prey interactions, the PAM method offers advantages for the modeling of a variety of dynamical systems. These benefits compare well against a Monte Carlo method, which may similarly incorporate measurements but requires numerical simulations to formulate its predictions. Unlike Monte Carlo, the predictions of PAM do not vary with the number of simulations or the tolerances of the numerical solver [116]. PAM scales well with the number of probabilistic variables in the model, whereas the number of Monte Carlo simulations required to formulate a prediction is a multiple of these variables. Models with stochastic processes additionally challenge the capacity of numerical solvers to converge or arrive at an accurate solution [117]. Therefore, the capacity of PAM to formulate predictions through analytical means should become increasingly more apparent for systems of greater complexity.

Chapter 4: Bioinspired pursuit

This chapter covers the effort to achieve pursuit behavior onboard a bioinspired fish robot. This content is an extension of the current state of the art in fish-like robotics to include pursuit behavior (see Section 1.2.2). The ultimate goal of this chapter is to derive a condition under which capture is guaranteed. A common criterium for guaranteed capture is to show that the range between the predator and prey is always decreasing. Analysis of the two-agent range dynamics converts this criterium into a condition on the maximum heading deviation away from the desired swimming direction.

To draw conclusions about whether a pursuit engagement will be successful, it is first necessary to derive the equations of motion in a two body pursuit scenario. As shown in the pursuit geometry in Fig. 4.1, define r as the distance between agent 1 and agent 2 and θ as the angle from the inertial reference of the line from 1 to 2. Define δ_i as the angle of the agent's velocity from the line of sight.

Thus, with $\mathbf{j} = \sqrt{-1}$

$$re^{\mathbf{j}\theta} = (x_2 - x_1) + j(y_2 - y_1).$$

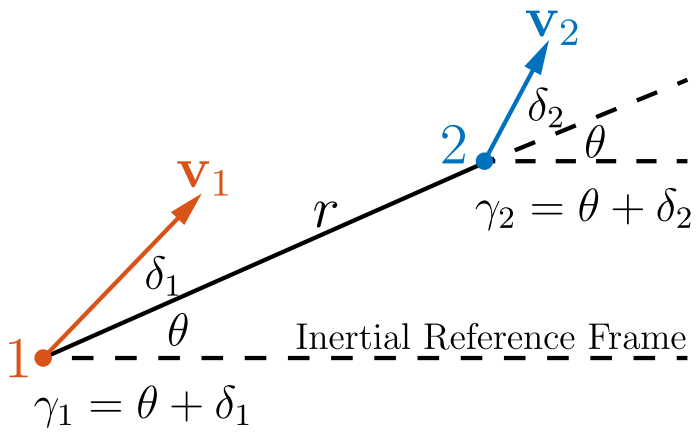

Figure 4.1: Pursuit geometry.

Taking the derivative,

$$\begin{aligned}
\frac{\mathrm{d}}{\mathrm{d}t}(re^{\mathbf{j}\theta}) &= (\dot{x}_2 - \dot{x}_1) + \mathbf{j}(\dot{y}_2 - \dot{y}_1) \\
\frac{\mathrm{d}}{\mathrm{d}t}(re^{\mathbf{j}\theta}) &= (v_2\cos\gamma_2 - v_1\cos\gamma_1) + j(v_2\sin\gamma_2 - v_1\sin\gamma_1) \\
\frac{\mathrm{d}}{\mathrm{d}t}(re^{\mathbf{j}\theta}) &= v_2 e^{\mathbf{j}\gamma_2} - v_1 e^{\mathbf{j}\gamma_1} \\
\dot{r}e^{j\theta} + \mathbf{j}r\dot{\theta}e^{\mathbf{j}\theta} &= v_2 e^{\mathbf{j}\gamma_2} - v_1 e^{\mathbf{j}\gamma_1} \\
\dot{r} + \mathbf{j}r\dot{\theta} &= v_2 e^{\mathbf{j}(\gamma_2-\theta)} - v_1 e^{\mathbf{j}(\gamma_1-\theta)} \\
\dot{r} + \mathbf{j}r\dot{\theta} &= v_2 e^{\mathbf{j}\delta_2} - v_1 e^{\mathbf{j}\delta_1},
\end{aligned}$$

Separate the real and imaginary parts to arrive at,

$$\dot{r} = v_2\cos\delta_2 - v_1\cos\delta_1 \tag{4.1}$$

$$r\dot{\theta} = v_2\sin\delta_2 - v_1\sin\delta_1, \tag{4.2}$$

or see Ref. [20] for an alternative derivation. From Eqn. (4.1), a sufficient condition for $\dot{r} < 0$ is $\cos\delta_1 > \frac{v_2}{v_1}\cos\delta_2$, or equivalently,

$$|\delta_1| < \cos^{-1}\left(\frac{v_2}{v_1}\cos\delta_2\right). \tag{4.3}$$

And so to state whether capture is guaranteed, information about the prey movement and the bound on $|\delta_1|$ are needed. To determine this bound, it is first necessary to show that the control law results in a stable, forward-swimming limit cycle in the desired direction. As will be seen in Section 4.2, the average swimming speed and angular velocity of the limit cycle are also needed in the derivation of the bound and so these are determined in Section 4.1.

The chapter then proceeds as follows. Section 4.1 analyzes an autonomous control law to determine which gains result in the desired swimming behavior. Section 4.2 derives the capture condition for this vehicle by deriving an expression for the bound on $|\delta_1|$. Section 4.3 details the experimental demonstration of pursuit under this control law with the fish robot.

4.1 Feedback control of Chaplygin fish

With the ultimate goal of providing a condition under which capture is guaranteed, it is first necessary to present an autonomous control law that results in a stable, forward-swimming limit cycle. This section presents that result by performing a limit cycle and bifurcation analysis. At the end of this section, the mean speed and angular velocity of the stable limit cycle are determined. These are used in Section 4.2 to aid in determining the bound on the pursuit angle.

4.1.1 Dynamics of a Chaplygin fish

As mentioned in Chapter 1, the modeling work done here takes advantage of the connection between the Chaplygin sleigh and a fish robot driven by an internal reaction wheel. The Chaplygin sleigh is a well understood dynamical system with a nonholonomic constraint. A sleigh with a reaction wheel of inertia J_d located at the center of mass (x, y) on a body of inertia J has dynamics [118]

$$\begin{aligned}
\dot{x} &= v\cos\gamma - l\omega\sin\theta \\
\dot{y} &= v\sin\gamma + l\omega\cos\theta \\
\dot{v} &= l\,\omega^2 - \frac{\zeta_d}{m}v \\
\dot{\gamma} &= \omega \\
\dot{\omega} &= \frac{1}{b}\left(\zeta_m\dot{\psi} - \omega\left(\zeta_d l^2 + \zeta_r\right) - mlv\omega - \tau\right) \\
\ddot{\psi} &= -\ddot{\theta} + \frac{1}{J_d}\left(-\zeta_m\dot{\psi} + \tau\right)
\end{aligned}$$

where v is the forward speed of the sleigh, γ is the inertial heading angle, $\dot{\psi}$ is the speed of the wheel with respect to the body frame, $b = J + J_d$, ζ_d is a translational drag term, is ζ_r a rotational drag term, and ζ_m is a motor drag term.

For $\zeta_m = \zeta_r = 0$, the equations of motion become

$$\dot{v} = l\,\omega^2 - dv \tag{4.4}$$

$$\dot{\gamma} = \omega \tag{4.5}$$

$$\dot{\omega} = \frac{ml}{b}v\omega - \frac{1}{b}\tau \tag{4.6}$$

$$\ddot{\psi} = -\ddot{\theta} + \frac{1}{J_d}\tau, \tag{4.7}$$

where $d = \zeta_d/m$. These equations of motion are used throughout this chapter with the control law presented in Section 4.1.2.

4.1.2 Limit Cycle

It must first be established that there exists a control law to steer the Chaplygin fish in the desired direction while undergoing forward swimming behavior in a limit cycle. Consider the control law

$$u = b\left(-K_1\omega + K_2 \sin(\gamma - \gamma_d + \mu)\right), \tag{4.8}$$

where b is the moment of inertia $J + ml^2$, and K_1 and K_2 are the feedback gains.

The feedback law given in Eqn. (4.8) with drag coefficient $d \geq 0$, mass $m > 0$, length $l > 0$, moment of inertia $b > 0$, $K_1 > 0$, and $K_2 > 0$ results in the closed-loop dynamics

$$\dot{\omega} = -\frac{ml}{b} v\omega + K_1\omega - K_2 \sin(\gamma - \gamma_d) + \mu, \tag{4.9}$$

where K_1 and K_2 are feedback gains and μ is a parameter used later to adapt this law for pursuit.

The simulation with $\mu = \gamma_d = 0$ shown in Fig. 4.2 suggests that these dynamics result in a forward swimming limit cycle with some nominal speed $\overline{v}$. A stable limit cycle is a periodic trajectory through a state space to which all initial conditions converge. The following section establishes the existence of a stable limit cycle for this system.

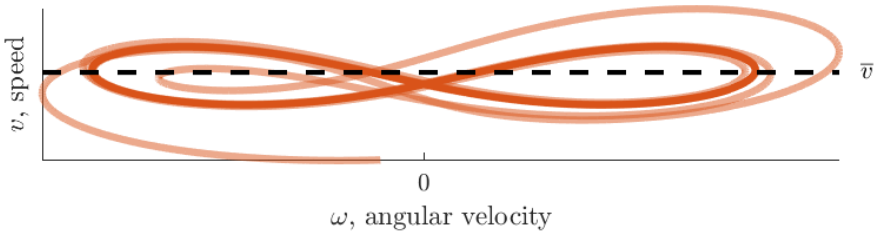

Figure 4.2: Limit cycle in the speed v, angular velocity ω plane. Dashed line indicates the average forward speed $\overline{v}$.

4.1.3 Bifurcation analysis of closed-loop system

The closed-loop system exhibits bifurcation behavior in which the desired limit cycle corresponding to forward swimming behavior is achieved only for certain values of the control gains K_1 and K_2. For other values of these gains, the angular velocity in the resulting limit cycle does not switch signs and the model fish spins in a circle, see Fig. 4.3(b). Turn now to a bifurcation analysis to establish the existence of the desired limit cycle and determine the allowable range of gains.

First, Eqn. (4.4) can be re-written as

$$\dot{v} = d\left(\frac{l}{d}\omega^2 - v\right). \tag{4.10}$$

For $\dot{\omega} = 0$, i.e., $\omega = \omega_0$ constant, the subsystem in Eqn. (4.10) exponential stabilizes $v = \frac{l}{d}\omega_0^2$ with Lyapunov function

$$V_1(v) = \frac{1}{2}\left(\frac{l}{d}\omega_0^2 - v\right)^2. \tag{4.11}$$

For $d \gg 1$, there is a time-scale separation between the v subsystem (fast) and the (θ, ω) subsystem (slow). Let $a = \frac{ml^2}{bd} > 0$. Without loss of generality, let reference

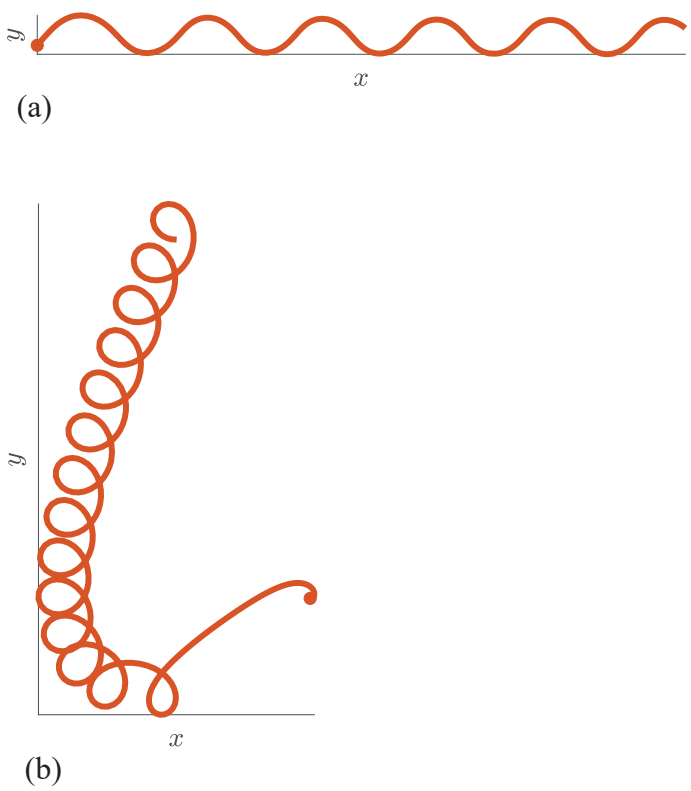

Figure 4.3: (a) Forward-swimming trajectory of a Chaplygin sleigh under the control law in Eqn. 4.8 and (b) undesirable trajectory resulting from a global bifurcation related to the control gains.

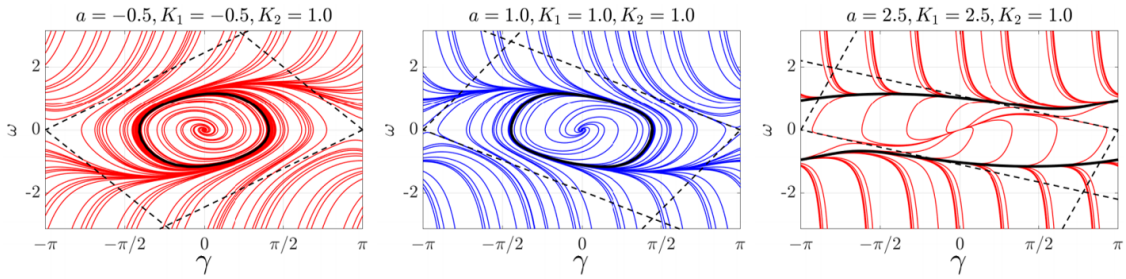

Figure 4.4: Bifurcations of the nonlinear pendulum in phase space: (Left) unstable limit cycle for $-2\sqrt{K_2} < a < 0$; (Middle) stable limit cycle for $0 < a < 2\sqrt{K_2}$; and (Right) two stable limit cycles for $a > a^* > 2\sqrt{K_2}$. Black dashed lines are the stable and unstable manifolds of the linearization of the saddle point at $\theta = \pm\pi$.

angle $\theta_d = 0$. Substituting the solution $v = \frac{l}{d}\omega^2$ (with ω treated as a constant) into the slow subsystem yields

$$\dot{\theta} = \omega$$

$$\dot{\omega} = -a\omega^3 + K_1\omega - K_2 \sin\theta, \tag{4.12}$$

which is the equation of motion of a pendulum with nonlinear damping and natural frequency $\sqrt{K_2}$. The system given by Eqn. (4.12) has equilibrium points $(0, 0)$ and $(\pm\pi, 0)$. As will soon be shown, it also has a limit cycle for certain values of a and K_1.

The Jacobian of Eqn. (4.12) is

$$\frac{\partial f}{\partial z} = \begin{bmatrix} 0 & 1 \\ -K_2\cos\theta & -3a\omega^2 + K_1 \end{bmatrix}, \tag{4.13}$$

which implies the origin $(0, 0)$ is an unstable node or focus and the point $(\pm\pi, 0)$ is a saddle. To facilitate analysis of the limit cycle in Eqn. (4.12), let $K_1 = a$, which yields

$$\dot{\theta} = \omega \tag{4.14}$$

$$\dot{\omega} = a(-\omega^3 + \omega) - K_2 \sin\theta. \tag{4.15}$$

The linearization of Eqn. (4.14)–(4.15) at $(\theta, \omega) = (0, 0)$ becomes

$$\left.\frac{\partial f}{\partial z}\right|_{(0,0)} = \begin{bmatrix} 0 & 1 \\ -K_2 & a \end{bmatrix}, \tag{4.16}$$

which has eigenvalues $\lambda_{1,2} = \frac{a}{2} \pm \frac{1}{2}\sqrt{a^2 - 4K_2}$. Therefore, the eigenvalues are complex if $|a| < 2\sqrt{K_2}$. Consider a as a bifurcation parameter. For $-2\sqrt{K_2} < a < 0$,

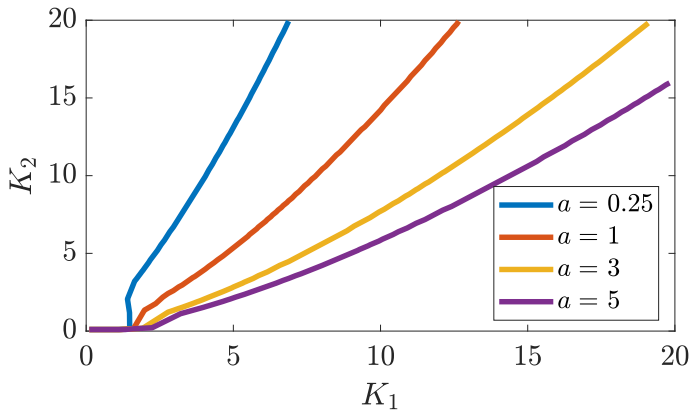

Figure 4.5: Numerical bifurcation analysis: the region above a given curve results in the desired limit cycle.

the origin is a stable focus and, for $0 < a < 2\sqrt{K_2}$, the origin is an unstable focus. Therefore, as a passes through zero, there is a Hopf bifurcation [119] giving rise to a stable limit cycle for $0 < a < 2\sqrt{K_2}$ (and an unstable limit cycle for $-2\sqrt{K_2} < a < 0$).

For some $a^* > 0$, there is another global bifurcation and the limit cycle splits into two limit cycles that orbit the phase cylinder [120]: one in the positive direction and one in the negative direction. This global bifurcation occurs when the limit cycle tangentially intersects the stable manifold of the saddle point at $\theta = \pm\pi$.

For the case where $K_1 \neq a$, a numerical analysis to determine the presence of the desired limit cycle uses the following scheme. For a given set of parameters $a, K_1, K_2 > 0$, choose an initial condition near the origin $(\theta, \omega) = (0, 0)$, which is an unstable fixed point. Simulate the system dynamics for a length of time observed to be much higher than the period of the limit cycle. If, at the end of the simulation, $|\theta| > \pi$, then the desirable limit cycle is not present. This bifurcation analysis shows

that if a trajectory reaches the saddle point $(\pm\pi, 0)$, the desired limit cycle breaks into two undesired ones as shown in Fig. 4.4.

To determine which gains (K_1, K_2) result in the desired behavior for a given set of physical parameters a, perform this numerical simulation scheme across many values of K_1, K_2, and a. Fig. 4.5 shows the results where, for a given a, pairs (K_1, K_2) above the curve result in the desirable limit cycle and those below do not. Gain K_1 has an indirect effect on the amplitude of oscillations about the desired heading angle: larger K_1 creates larger heading oscillations and faster average speed v. Gain K_2 appears in the dynamics as the square of the natural frequency of a pendulum system, so oscillations about the desired heading angle occur at frequency $\sqrt{K_2}$. This analysis shows that for a given K_2, K_1 can be increased only up to the bounding curve in Fig. 4.5. This allows for gains to be chosen intelligently to achieve the desired limit cycle, rather than through trial and error.

4.1.4 Mean limit cycle values

From Ref. [121], we know that a limit cycle must have an unstable fixed point interior to the orbit of the limit cycle. The above limit cycle analysis suggests that the dynamics are periodic with period T such that $\omega(t) = \omega(t + T)$. Write the dynamics again

$$\dot{v} = l\omega^2 - dv \tag{4.17}$$

$$\dot{\gamma} = \omega \tag{4.18}$$

$$\dot{\omega} = -\frac{ml}{b} v\omega + K_1\omega - K_2 \sin\gamma, \tag{4.19}$$

and average the ω dynamics over one period

$$\begin{aligned}\overline{\dot{\omega}} &= \frac{1}{T}\int_t^{t+T}\left(\frac{\mathrm{d}}{\mathrm{d}t}\omega(t)\right)\mathrm{d}t \\ &= \frac{1}{T}\int_{\omega(t)}^{\omega(t+T)}\mathrm{d}\omega \\ &= \frac{\omega(t+T)-\omega(t)}{T} \\ &= 0.\end{aligned}$$

Now take the same integral across both sides of the ω dynamics

$$\begin{aligned}\frac{1}{T}\int_t^{t+T}\dot{\omega}\mathrm{d}t &= \frac{1}{T}\int_t^{t+T}\left(-\frac{ml}{b}v\omega + K_1\omega - K_2\sin\gamma\right)\mathrm{d}t \\ 0 &= \frac{1}{T}\int_t^{t+T}\left(-\frac{ml}{b}v + K_1\right)\omega\mathrm{d}t - K_2\frac{1}{T}\int_t^{t+T}\sin\gamma\mathrm{d}t\end{aligned}$$

The second integral on the right hand side goes to zero since we have established the presence of a limit cycle and the dynamics Eqn. (4.19) are symmetric in γ. Once more using the time scale separation between the slow ω dynamics and fast v dynamics, take the ω outside the integral and conclude that

$$\overline{v} = \frac{bK_1}{ml} \approx \frac{1}{T}\int_t^{t+T} v\mathrm{d}t. \tag{4.20}$$

Take this averaging integral across both sides of the v dynamics

$$\begin{aligned}\frac{1}{T}\int_t^{t+T}\dot{v}\mathrm{d}t &= \frac{1}{T}\int_t^{t+T}\left(l\omega^2 - dv\right)\mathrm{d}t \\ \frac{1}{T}\int_{v(t)}^{v(t+T)}\mathrm{d}v &= \frac{l}{T}\int_t^{t+T}\omega^2\mathrm{d}t - \frac{d}{T}\int_t^{t+T}v\mathrm{d}t \\ \frac{v(t+T)-v(t)}{T} &= l\overline{\omega^2} - d\overline{v} \\ 0 &= l\overline{\omega^2} - d\overline{v} \\ \overline{\omega^2} &= \frac{d}{l}\overline{v},\end{aligned}$$

and substituting Eqn. (4.20) yields

$$\overline{\omega^2} = \frac{dbK_1}{ml^2}. \tag{4.21}$$

This result is needed in the next section to determine the bounds on the heading angle, which yields a capture condition for pursuit.

4.2 Pursuit with Chaplygin fish

This section extends the results of the previous section to pursuit. To derive a condition for guaranteed capture, the mean swimming speed and angular velocity are used in an analysis of the dynamics. Using this capture condition, several pursuit tactics capable of being implemented by the Chaplygin fish are presented.

4.2.1 Derivation of capture condition

Now examine the case where $\gamma_d \neq 0$ and seek to derive capture guarantees for a pursuer using these inner loop dynamics. From Eqn. (4.1), a sufficient condition for $\dot{r} < 0$ is $\cos\delta_1 > \frac{v_2}{v_1}\cos\delta_2$, or equivalently,

$$|\delta_1| < \alpha = \cos^{-1}\left(\frac{v_2}{v_1}\cos\delta_2\right). \tag{4.22}$$

With the presence of a limit cycle confirmed, it follows that under certain conditions the heading angle oscillates about some nominal direction – the average heading of the sleigh. Above it was shown that this limit cycle exists when $\gamma_d = \mu = 0$. Now turn to show that this oscillatory behavior exists under other conditions and can be used to guarantee capture of a target.

Let $\gamma_d(t) = \theta + \delta^*(t)$ be a generally time-varying signal. From Fig. 4.1, $\gamma - \theta = \delta$ the deviation angle and so rewrite Eqn. (4.9) as

$$\dot{\omega} = -\frac{ml}{b} v\omega + K_1\omega - K_2 \sin(\gamma - \gamma_d) + \mu$$

$$\dot{\omega} = -\frac{ml}{b} v\omega + K_1\omega - K_2 \sin(\gamma - \theta - \delta^*(t)) + \mu$$

$$\dot{\omega} = -\frac{ml}{b} v\omega + K_1\omega - K_2 \sin(\delta - \delta^*(t)) + \mu.$$

Now choose $\mu = \ddot{\theta}$ and assume that θ is a slowly varying exogenous input such that $\ddot{\theta} \approx 0$ and the limit cycle therefore exists. Define $\epsilon = \delta - \delta^*(t)$ and so

$$\ddot{\epsilon} = \dot{\omega} - \ddot{\theta} - \frac{\mathrm{d}^2}{\mathrm{d}t^2}\delta^*(t). \tag{4.23}$$

This second derivative term includes second derivatives of the prey's speed and heading, which is either costly or supernatural for the predator to have access to. In lieu of a robust controller, assume that the prey is slowly maneuvering enough such that $\frac{\mathrm{d}^2}{\mathrm{d}t^2}\delta^*(t) \approx 0$. With $\mu = \ddot{\theta}$ the heading angle error dynamics are

$$\ddot{\epsilon} = -\frac{ml}{b} v\omega + K_1\omega - K_2 \sin\epsilon. \tag{4.24}$$

Substitute $v = \overline{v} + \Delta v$ using Eqn. (4.20) where Δv are the deviations from the mean value of $\overline{v}$.

$$\ddot{\epsilon} = -\frac{ml}{b} \Delta v\omega - K_2 \sin\epsilon. \tag{4.25}$$

Since speed $v > 0$, the most conservative bound on Δv is $|\Delta v| < \overline{v} = \frac{bK_1}{ml}$ and so for $K_2 \gg K_1$, the dynamics are approximately

$$\ddot{\epsilon} \approx -K_2 \sin\epsilon. \tag{4.26}$$

Assume that $\theta(t)$ is slowly varying such that $\dot{\theta} \approx 0$ and the prey maneuvers slowly so that $\dot{\delta}^*(t) \approx 0$ and so $\dot{\epsilon} = \dot{\delta} - \dot{\delta}^*(t) = \dot{\gamma} - \dot{\theta} - \dot{\delta}^*(t) \approx \omega$. This assumption yields two results. First, the natural frequency of oscillations is $\omega_n = \sqrt{K_2}$, corresponding to a period of

$$T = \frac{2\pi}{\sqrt{K_2}}. \tag{4.27}$$

Second, the exact solution to these dynamics is (see Ref. [122]),

$$\epsilon(t) = 2 \arcsin\left(\sin\frac{\epsilon_0}{2} sn\left[K\left(\sin^2\frac{\epsilon_0}{2}\right) - \omega_n t; \sin^2\frac{\epsilon_0}{2}\right]\right), \tag{4.28}$$

where $sn(u;m)$ is the Jacobi elliptic function and $K(m)$ is the complete elliptical integral of the first kind. By calculating the average $\dot{\epsilon}^2$ for this simplified system and combining with the actual $\overline{\omega^2} = dbK_1/ml^2$, the amplitude of oscillations can be determined (because this simplified system oscillates with amplitude ϵ_0 under the $\dot{\epsilon}_0 = 0$ assumption). The mean square angular velocity over one period is calculated as

$$\overline{\dot{\omega}^2} \approx \overline{\ddot{\delta}^2} \approx \overline{\ddot{\epsilon}^2} = \frac{1}{T}\int_0^T \left(\frac{\mathrm{d}}{\mathrm{d}t}\delta(t)\right)^2 \mathrm{d}t. \tag{4.29}$$

To ease computations from using the exact solution to the undamped pendulum, use a small angle approximation $\sin\epsilon \approx \epsilon$. Now the (even more) simplified dynamics are

$$\ddot{\epsilon} = -K_2\epsilon.$$

With initial conditions $\epsilon(0) = \epsilon_0$ and $\dot{\epsilon}(0) = 0$, the solution is

$$\begin{aligned}
\epsilon(t) &= \epsilon_0 \cos(\sqrt{K_2}t) \\
\dot{\epsilon}(t) &= -\epsilon_0 \sqrt{K_2} \sin(\sqrt{K_2}t) \\
\ddot{\epsilon}(t) &= -\epsilon_0 K_2 \cos(\sqrt{K_2}t) = -K_2 \epsilon(t).
\end{aligned}$$

The average square angular velocity is

$$\begin{aligned}
\overline{\dot{\epsilon}^2} &= \frac{1}{T}\int_0^T \dot{\epsilon}(t)^2 \mathrm{d}t \\
&= \frac{\sqrt{K_2}}{2\pi}\int_0^{\frac{2\pi}{\sqrt{K_2}}} K_2 \epsilon_0^2 \sin^2(\sqrt{K_2}t)\mathrm{d}t \\
\overline{\epsilon^2} &= \frac{1}{2}K_2\epsilon_0^2
\end{aligned} \tag{4.30}$$

Under the small angle approximation, $\frac{1}{2}\epsilon^2 \approx 1 - \cos\epsilon$. Pulling it all together and recognizing that ϵ plays the role of $\max \epsilon$ in the limit cycle,

$$\begin{aligned}
\overline{\dot{\epsilon}^2} &= K_2(1 - \cos\epsilon_0) \\
\overline{\dot{\epsilon}^2} \approx \overline{\omega^2} = \frac{dbK_1}{ml^2} &= K_2(1 - \cos\epsilon_0) \\
\epsilon_0 &= \arccos\left(1 - \frac{dbK_1}{ml^2K_2}\right).
\end{aligned}$$

Now finally there is an estimate of the amplitude of oscillations within the limit cycle,

$$\max\epsilon \approx \arccos\left(1 - \frac{dbK_1}{ml^2K_2}\right) \approx \sqrt{\frac{2dbK_1}{ml^2K_2}}. \tag{4.31}$$

Figure 4.6 shows a simulation of a pursuit of a slowly maneuvering target and the theoretical bounds on the deviation angles predicted by this result. If $\max\epsilon$ is such that Eqn. (4.22) is satisfied, capture is guaranteed. This can be achieved by choice of K_1, K_2 with an estimate of the maximum prey speed. To relate Eqn. (4.31) to

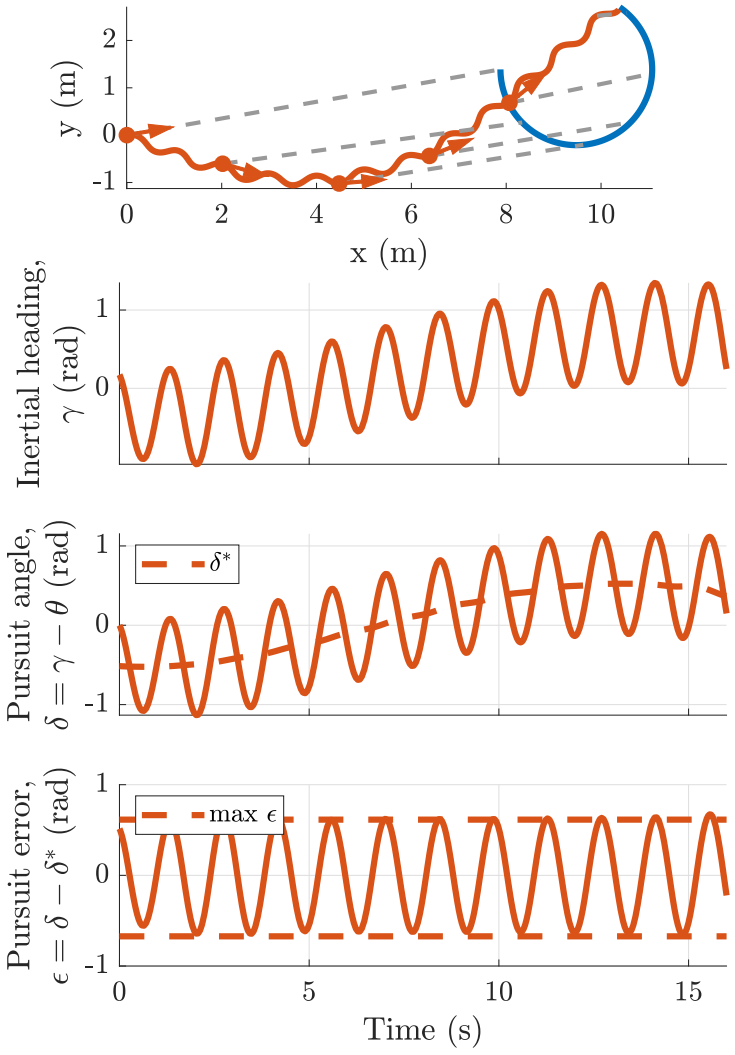

Figure 4.6: Simulation of pursuit of a slowly maneuvering target by a Chaplygin fish under control law Eqn. (4.8) with $\delta^*(t)$ chosen for parallel navigation.

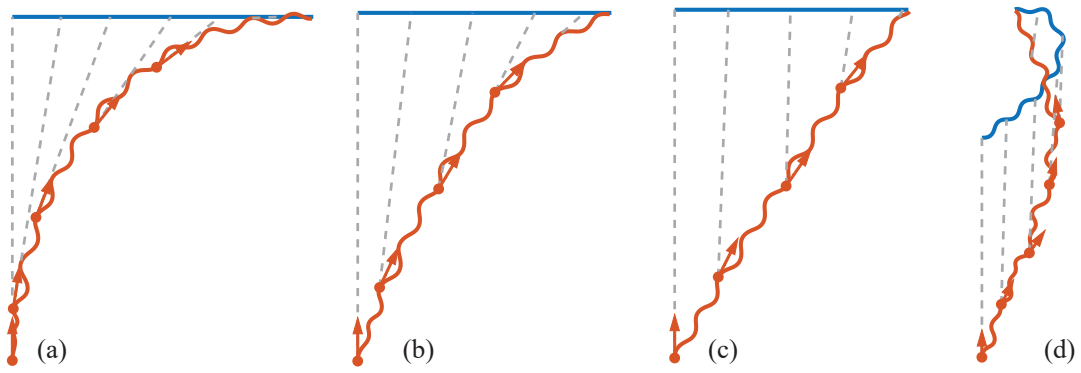

Figure 4.7: Simulation of predator and prey trajectories for (a) pure pursuit $\delta^* = 0$ and a non-maneuvering prey, (b) deviated pure pursuit $\delta^* = -0.3$ and a non-maneuvering prey, (c) intercept, and (d) parallel navigation with a maneuvering prey. Grey dashed lines remain parallel, indicating successful parallel navigation.

capture condition Eqn. (4.22), subtract the effect of the non-zero pursuit angle $\delta^*(t)$. The capture condition becomes

$$\max \epsilon + \max_t \delta^*(t) < \cos^{-1}\left(\frac{v_2}{v_1}\cos\delta_2\right). \tag{4.32}$$

This condition may be difficult to evaluate without knowledge of $\max_t \delta^*(t)$ ahead of time since the prey's movements are unpredictable. Knowledge of the prey's maximum speed and turning rate may be used to predict if capture will be successful.

4.2.2 Pursuit tactics

Now, the choice of desired pursuit angle δ^* can be used to implement several pursuit strategies. See Section 2.5 for an overview of these tactics.

Pure Pursuit In pure pursuit, the pursuers heading γ is aligned with the line-of-sight angle θ. In the current context this requires $\gamma_d = \theta$ and so $\delta^* = \gamma_d - \theta = 0$.

$$\delta^*_{\text{PP}}(t) = 0 \tag{4.33}$$

Deviated Pure Pursuit Deviated pure pursuit maintains the pursuer's heading γ a fixed angle to the left or right of the line-of-sight angle θ.

$$\delta^*_{\text{DPP}}(t) = \delta^* \text{ constant} \tag{4.34}$$

Intercept For a constant velocity predator and prey, the intercept angle is given by Ref. [20] as

$$\delta^*_{\text{intercept}} = \sin^{-1}\left(\frac{v_2}{v_1}\sin\delta_2\right).$$

Substituting the expression for the mean speed Eqn. (4.20), the intercept angle for the Chaplygin fish becomes

$$\delta^*(t)_{\text{intercept}} = \sin^{-1}\left(\frac{ml}{bK_1}v_2\sin\delta_2\right). \tag{4.35}$$

Parallel navigation Parallel navigation is a pursuit tactic where the predator aims to keep the LOS heading angle θ constant (hence *parallel* navigation) [20]. This has the effect of eliminating optical flow from the perspective of the prey (hence *Motion camouflage*). The prey sees only a looming threat that increases in size, but does not translate in the optical field. Motion camouflage is also said to be a strategy where the predator keeps its heading fixed relative to an inertial reference (e.g. a cheetah keeping a tree on the ray extending from the prey to the predator throughout its stalking trajectory). Parallel navigation is sometimes

referred to as motion camouflage with respect a point at infinity or infinity-point motion camouflage, as opposed to real-point motion camouflage. Parallel navigation is also sometimes called *constant bearing*, but the use of the term *bearing* is so varied in literature that I prefer to not use it in any context.

For non-maneuvering prey, the intercept strategy in the above section is sufficient to achieve parallel navigation. It follows then for a slowly maneuvering prey, that allowing tracking a time-varying δ^* will result in parallel navigation. Let $\delta^* = \delta^*(t)$ so that the pursuit angle can now change as a function of time (more practically, as a function of the prey's movement). At any time t let

$$\delta^*(t) = \delta^*_{\mathrm{PN}}(t) = \sin^{-1}\left(\frac{ml}{bK_1} v_2(t) \sin\delta_2(t)\right). \tag{4.36}$$

Figure 4.7 shows simulations of these four pursuit strategies.

4.3 Experimental demonstration

This section demonstrates how this control law can be implemented in practice, onboard a robot with a microcontroller and motor driving a reaction wheel. First, since in practice this control law is implemented by a DC motor, a brief review of motor dynamics and an implementation of this control law for use onboard a microcontroller are presented. Afterwards, the design of the fish robot and experimental testbed are presented before the experimental pursuit is shown.

4.3.1 Implementing the control law with DC motor

Typical DC motors take not desired torque as an input, but instead require a voltage input. To generate input torque using a DC motor and a wheel, introduce the following relationships:

$$\tau_m = K_\tau i, \qquad e = K_e \Omega, \tag{4.37}$$

where K_τ is the motor torque constant, τ_m is motor torque, i is current, K_e is the back EMF (Electromotive Force) constant, Ω is the motor angular rate, and e is the back-EMF voltage. Modeling the motor system as a closed-loop RLC circuit yields $V = L\frac{di}{dt} + iR + e$. Neglecting the inductance L,

$$V = iR + K_e \Omega, \tag{4.38}$$

where V denotes applied total voltage and R is the resistance of the motor winding. When a torque τ_m is applied by the motor, it is amplified by the gear ratio K_g, thus the input torque applied to the reaction wheel is $u = K_g \tau_m$. The angular rate $\dot{\psi}$ of the reaction wheel, which is measured by an encoder, is reduced by the gear ratio to $\dot{\psi} = \Omega / K_g$. Substituting Eqn. (4.37) and the gear ratio into Eqn. (4.38) yields the relationships

$$V = \frac{\tau_m}{K_\tau} R + K_e K_g \dot{\psi} \tag{4.39}$$

$$= \frac{u}{K_g K_\tau} R + K_e K_g \dot{\psi}, \tag{4.40}$$

$$u = C_1 V - C_2 \dot{\psi}, \tag{4.41}$$

where the constants are $C_1 = K_\tau K_g / R$ and $C_2 = K_\tau K_e K_g^2 / R$.

Since voltage V applied to the motor is proportional to the duty ratio of Pulse Width Modulation (PWM), then $V = V_{\max}\text{PWM}/255$ and any arbitrary torque profile can be determined by PWM. The relation between wheel torque and PWM is

$$u = \frac{K_\tau K_g}{R}\left(V_{max}\frac{PWM}{255} - K_e K_g \dot{\psi}\right). \tag{4.42}$$

The PWM corresponding to u is

$$PWM = \frac{255R}{K_\tau K_g V_{max}}\left(u + \frac{K_\tau K_e K_g^2 \dot{\psi}}{R}\right). \tag{4.43}$$

To characterize the motor used in experiments, K_τ and K_e were determined offline as follows. Stall current was measured at 3 A when a torque load of 0.595 Nm was applied to the motor. A maximum speed of 500 rpm with free load was measured at a rated voltage (12V). Then, K_τ and K_e in Eqn. (4.37) were determined to be 0.01 [Nm/A] and 0.01 [Vs], respectively. Given the resistance R and a gear ratio of K_g 20.4, plugging them into Eqn. (4.40) yields $C_1 = 0.05$ [Nm/V] and C_2= 0.01 [Nms] in Eqn. (4.41).

4.3.2 Fish robot overview

Jinseong Lee designed a fish robot made of flexible silicon rubber and 3D-printed material for use in this project as shown in Fig. 4.8. Reference [65] originally presented the design of this robot. Inspired by the body shape of carangiform fish, the robot was modeled with a Bluegill side silhouette and a Joukowski airfoil top silhouette, to be used in the mathematical analysis of flow sensing [123].

The robot body is made of Dragon Skin 10, a flexible silicon rubber that is

Table 4.1: Fish robot specification

Item	**Robot**	**Wheel**	**Units**
Size	317(L) x 80(W) x 150(H)	59(D)	mm
Mass	1.4	0.4	kg
Inertia	0.005	0.0003	kgm^2

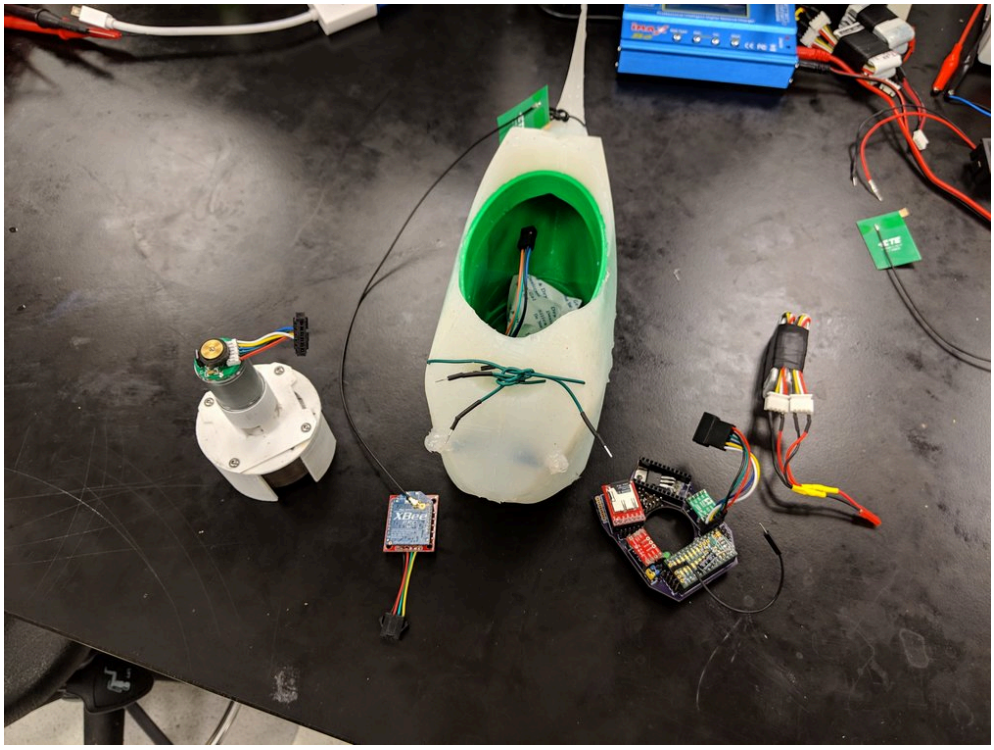

Figure 4.8: A reaction-wheel-based swimming robot made from flexible material. All electronic modules are contained in a watertight pressure vessel. The fish body was designed and modeled by Jinseong Lee. Electronic components including the DC motor were chosen by Jinseong Lee as well.

easily molded to any shape. Its flexibility provides tail flapping motion when the reaction wheel rotates. To accommodate the motor and electronic components, the robot contains a pressure vessel made of 3D-printed PLA plastic coated with epoxy to be watertight. To stabilize and restore the body against rolling motion, the reaction wheel is placed just below the center of buoyancy so that the center of mass is lower than the center of buoyancy. The physical specifications are provided in Table 4.1.

The robot is embedded with various hardware components connected to a custom printed circuit board shown in Fig. 4.9. The board was designed by two summer interns, Jenny Mei and Brynne Schoen, to fit the electronic components chosen by Jinseong Lee. It includes the ARM Cortex-M4 micro processor, reaction wheel, Pololu 20.4:1 geared DC motor, motor driver, 48 pulse rotary encoder, 11.1V LiPo battery, micro SD card, custom interface PCB, power switch, umbilical port for charging and programming, color LEDs, 5/3.3 V regulators, multiplexer, 2.4GHz XBee transceiver, and MPU9250 IMU sensor. The communication between the micro processor and the devices is via serial SPI and I2C, and onboard data is stored in a micro SD card for data analysis. A XBee module transmits data wireless to a remote PC in real time. Wireless communication supports several commands such as start and stop for swimming, heading angle reset, feedback gain setting, and retrieving the files saved on the SD card. The RGB LEDs are activated to convey the state of the robot while swimming.

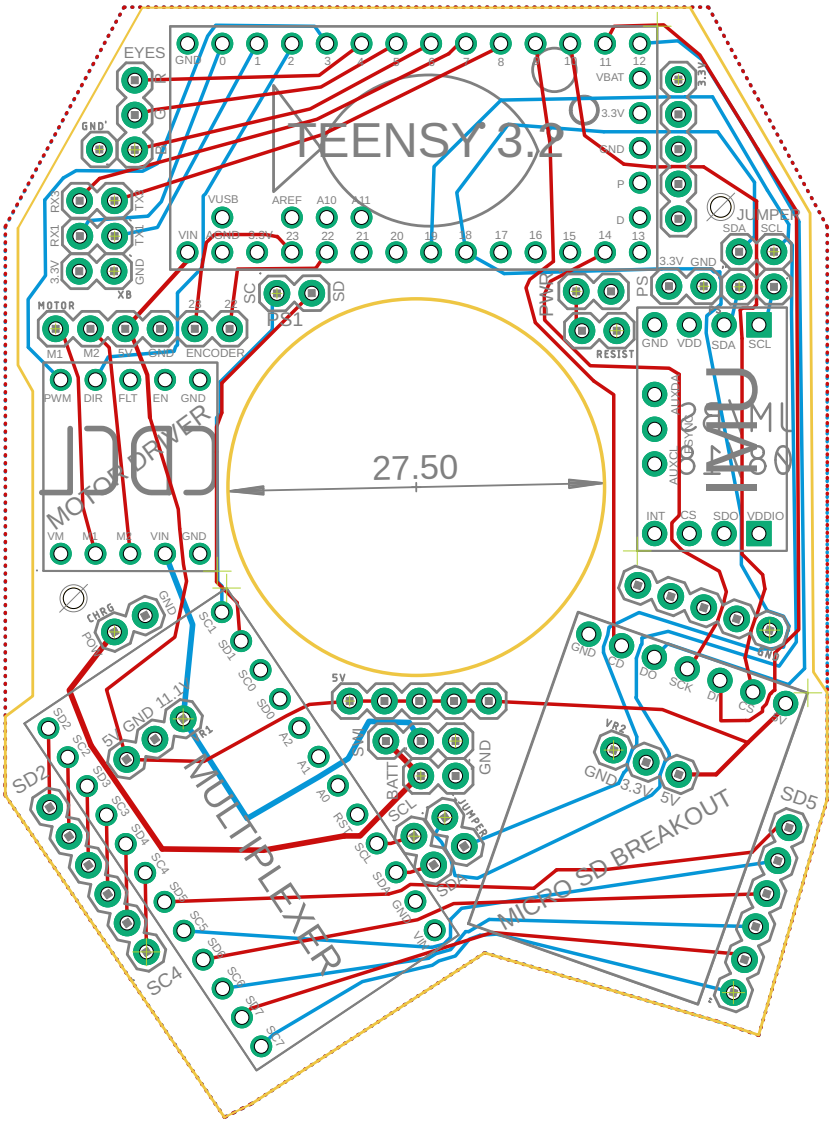

Figure 4.9: Custom printed circuit board used to connect all components used in the fish robot. The large through-hole allows for the components to be arranged radially around the motor to fit in the compact pressure vessel. The board was designed by two summer interns, Jenny Mei and Brynne Schoen, under the direction of Jinseong Lee.

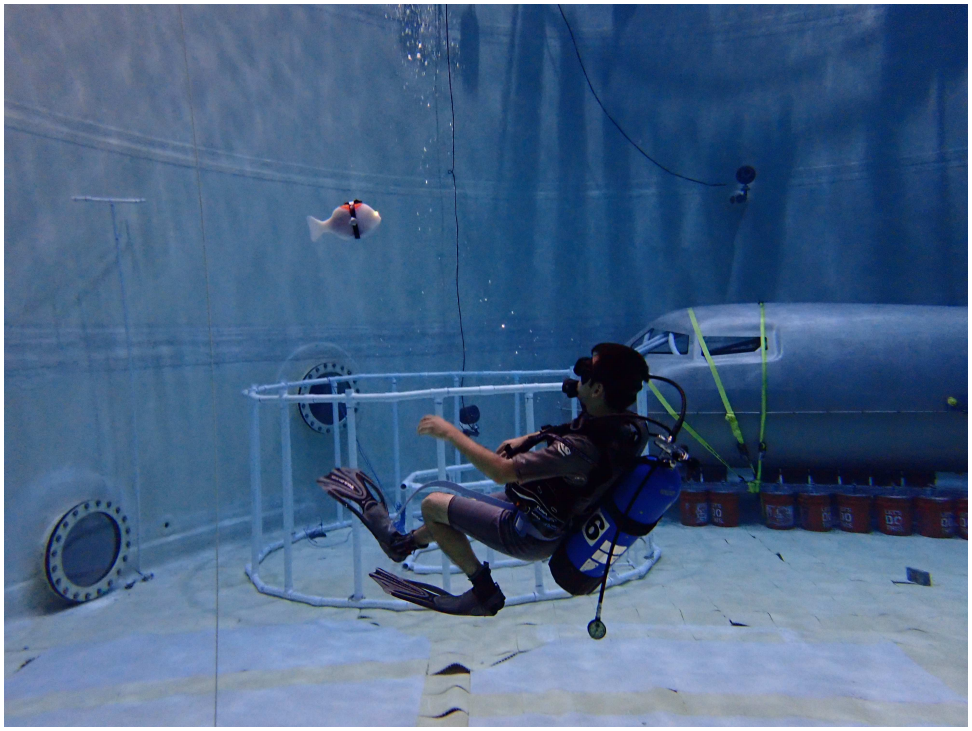

Figure 4.10: Neutral Buoyancy Research Facility.

4.3.3 Neutral Buoyancy Research Facility overview

Swimming motion and steering tests for a submerged vehicle have been demonstrated in the Neutral Buoyancy Research Facility of the University of Maryland (Fig. 4.10). Use of this facility is thanks to Dr. Dave Akin at the University of Maryland Space Systems Lab. The facility is equipped with 16 Qualisys underwater cameras to track three reflective markers mounted on either side of the fish robot. One of Dr. Akin's students, Jeremy Chang, introduced the motion capture system and managed a crew of scientific divers who aimed the cameras under my direction. To feedback virtual prey position to the fish robot for pursuit, it is necessary to have a medium of communication between the motion capture software and

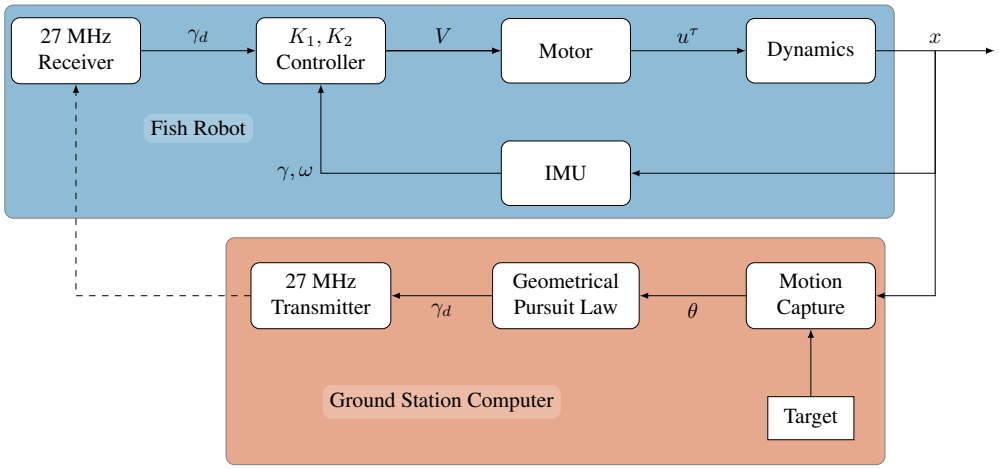

Figure 4.11: Experimental block diagram for Chaplygin fish pursuit in the Neutral Buoyancy Research Facility.

the fish robot. The Qualisys Track Manager program sends marker position data to a MATLAB program that both creates a virtual prey item and calculates the line-of-sight angle θ (Fig. 4.1). The line-of-sight angle is then sent over USB serial communication to a 27 MHz transmitter to the receiver aboard the fish robot. For pure pursuit, the fish uses this as the desired heading and implements the control law described in Section 4.1. This communication system was developed for the purposes of this project. Figure 4.11 shows the control architecture interplay between the onboard computation and sensing and the offboard motion capture system.

Due to interference from the magnetic field generated by the motor inside the fish robot, magnetometer data from the MPU9250 IMU could not be integrated with the accelerometer and gyroscope data to estimate a heading angle in the North-East-South-West refernce frame. Instead, only the accelerometer and gyroscope data were used in a filter to estimate heading with the positive x-axis defined by the initial

direction of the fish robot on start.

Lacking a means of communication from the fish robot to the MATLAB program that manages the virtual prey, the direction of the positive x-axis is defined by observing the motion of the robot for a short period of time. The virtual prey is then defined in that reference frame and begins moving while line-of-sight data is transmitted to the fish robot.

4.3.4 Experimental pursuit results

Before testing the outer-loop pursuit behavior, it is necessary to test the inner-loop guidance law Eqn. (4.8) in experiment. Figure 4.12 shows the response to a step function input of desired heading from 0 to 20 degrees. There is some noticeable disagreement between the heading determined by the onboard IMU and the offboard motion capture system that increases over time. Because the IMU is not using magnetometer readings there is inevitable drift in its estimate of heading, which accounts for this discrepancy. The rate of sensor drift was seen to be anywhere from roughly 2 to 10 degrees per minute depending on an untold number of variables.

Figure 4.13 shows the results of an experiment with feedback of the position of a virtual prey. In this pure pursuit test, the line-of-sight angle θ is the desired heading. As the distance r between the predator and prey decreases, the rate of change in the line-of-sight angle increases as $1/r$, as seen in the increasing amplitude of oscillations in the desired heading towards the end of the experiment. The inner and outer control loops were both successful in this experiment and the virtual prey

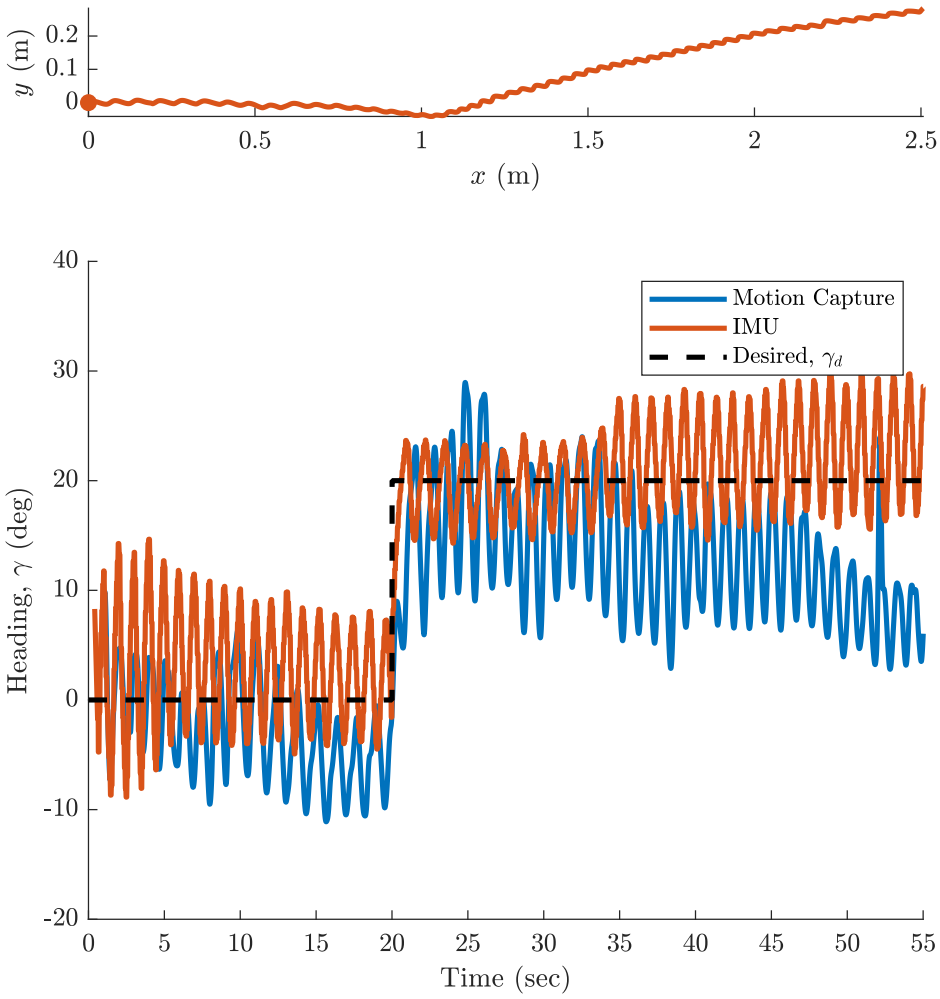

Figure 4.12: Experimental step response.

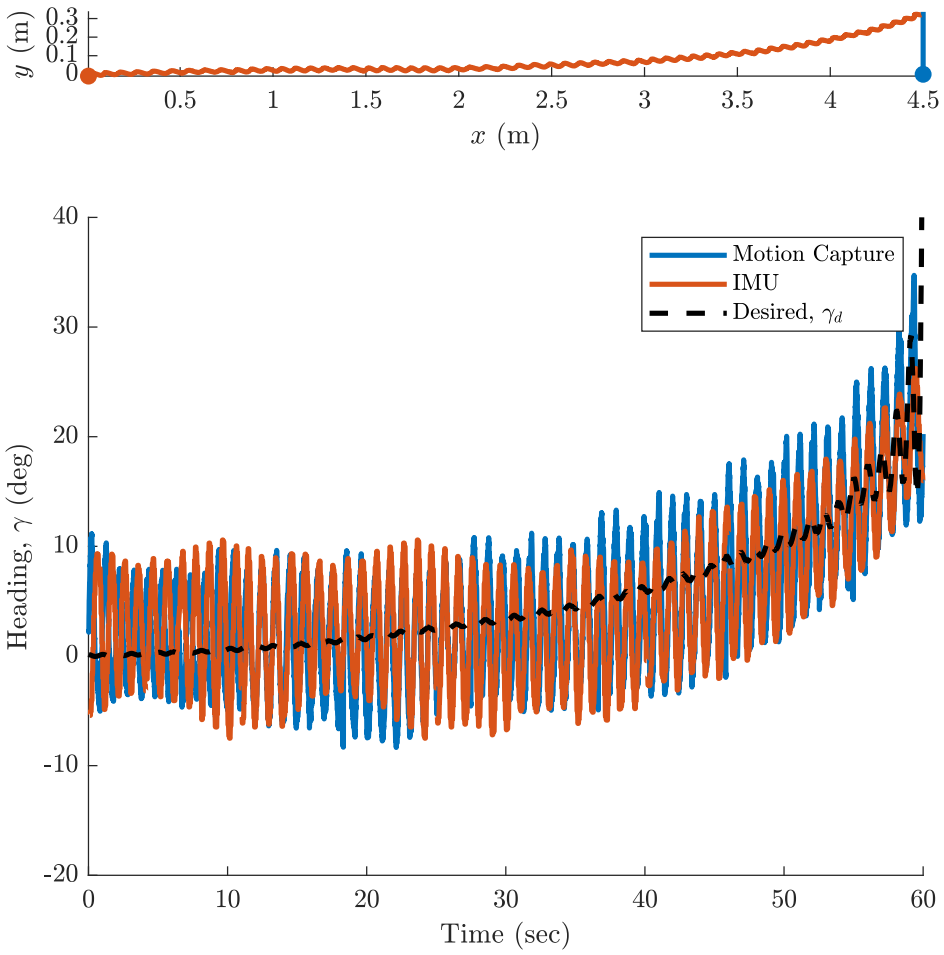

Figure 4.13: Experimental pursuit of virtual target.

is captured.

These two experiments provide a stress test of sorts for the theoretical analysis performed in the previous two sections. Controls engineers often prefer to live in the model world, testing algorithms and different strategies in simulation. However, once simulation and theory can yield no more results and the algorithms are satisfactory, it is a necessary sanity check to implement the control law in the real world. The documentation of these experiments also provides a starting point for future researchers wishing to implement pursuit onboard a vehicle of this type.

The first experiment demonstrates the step response of the system, one of the most basic tests of a control system. Due to the feedback of the inertial heading from the IMU, the robot appropriately adjusts its heading when commanded. The second experiment demonstrates the ability of the system to track a continually changing reference trajectory using feedback from the motion capture cameras. Typically, a more rigorous analysis of the system is needed to assure tracking of an arbitrary reference trajectory, but with the assumption (and virtual choice) of a slowly maneuvering prey, the controller converges to the changing reference at a rate faster than the changing itself and so the prey is captured.

4.4 Summary of chapter

This chapter covered several topics related to pursuit with a reaction-wheel driven fish robot. An autonomous control law is presented and shown in theory, simulation, and experiment to result in a steady, forward-swimming limit cycle in the desired direction. This result is extended to pursuit by allowing the desired direction to be a time-varying signal related to the line-of-sight angle between the predator and prey. Analysis of the pursuit geometry and the closed-loop system dynamics yields a condition that can be evaluated ahead of time to determine whether a pursuit will be successful. Given knowledge of the prey's maneuverability, this condition provides go/no-go decision that can be implemented onboard a robot to determine if it will be worth expending the resources to engage in pursuit. Experiments performed with feedback of prey direction from a motion capture camera system demonstrate the

use of this type of pursuit in practice.

Chapter 5: Vortex estimation and flow relative control

This chapter presents efforts to replicate the touch-at-a-distance sensing modality of the lateral line seen in fish by taking advantage of previous work done in this area (see Section 1.2.3) to push forward state-of-the-art capabilities to include vortex street tracking and flow-relative control.

The specific problem that is sought to be solved is to use an array of pressure sensors in closed-loop, feedback control of a rigid foil in a Kármán vortex street, a pattern of clockwise and anti-clockwise vortices shed by a blunt body and swimming fish due to flow separation. Once solved, this problem opens the door for the use of an artificial lateral line onboard underwater vehicles to track trajectories through a vortex street, including the energy efficient slaloming path. Measurements from the pressure sensors are used together with a model of the flow to estimate the location of the vortices within the street. By actuating angle of attack, the foil generates lift in the cross-stream direction and tracks reference trajectories through the vortex street.

The methodology of this work is outlined below and uses tools from potential flow theory, nonlinear estimation, and nonlinear observability. Estimates of the strength, phase, and cross-stream location of a vortex street are formed us-

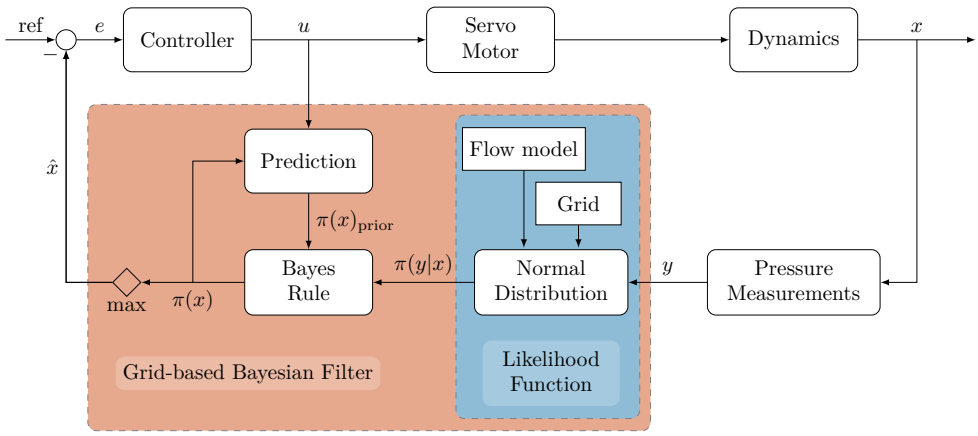

Figure 5.1: Block diagram showing the estimation and control architecture for the vortex sensing and flow-relative control experiment described in this chapter.

ing pressure measurements from an artificial lateral line and used in closed-loop, trajectory-tracking feedback control. The Kármán vortex street is modeled as a potential flow with two parallel infinite lines of vortices [73]. A Joukowski foil is placed in the flow model using the Joukowski transformation on a cylinder [75] and the Milne-Thomson Circle Theorem [100]. Measurement equations formed with the potential flow model and Bernoulli's principle output the predicted pressure reading according to three states: vortex strength of the street, cross-stream position of the street, and a phase angle that represents the downstream position of the primary vortex in the street. In line with the goal of a fully autonomous vehicle, all parameters and calculations are in a reference frame fixed to the Joukowski foil. The measurement equations, in conjunction with real-time sensor readings, are used in a nonlinear, recursive, grid-based Bayesian framework to estimate the three states. The estimate is used in feedback control of the angle of attack of the Joukowski foil to generate lift in the cross-stream direction and to track a reference trajec-

tory through the street. Figure 5.1 shows a block diagram illustrating how these components interact.

The techniques developed in this chapter are demonstrated in an experimental testbed. The testbed includes a 185 L flow tank, an air-bearing system to allow movement of the Joukowski foil in the cross-stream direction, and a system to generate vortices in the desired Kármán vortex street pattern. The system was successful in estimating the state of the vortex street as well as tracking the reference trajectories. This work has applications in autonomous underwater navigation in cluttered environments and sensing or pursuing other fish or robots in water.

The chapter proceeds as follows. Section 5.1 presents the model for the flow over a Joukowski airfoil subject to a Kármán vortex street and derives the measurement equation for the artificial lateral line. Section 5.2 describes the Bayesian framework used to estimate the location and strength of the vortex street. Section 5.3 covers the dynamics of the Joukowski foil and the controller for the angle of attack of the Joukowski foil. Section 5.4 presents the work on empirical observability-based path planning. Section 5.5 describes results from the experimental demonstration.

5.1 Modeling flow over a Joukowski airfoil in a Kármán vortex street

Figure 5.2 shows the physical layout of the modeling framework and the goal of the sensing and control design below. The Joukowski foil has four pressure sensors distributed on the forefront of the body. The Kármán vortex street is modeled with potential flow theory. The inertial reference frame $\mathcal{I} = (O, \mathbf{e}_1, \mathbf{e}_2)$ is aligned

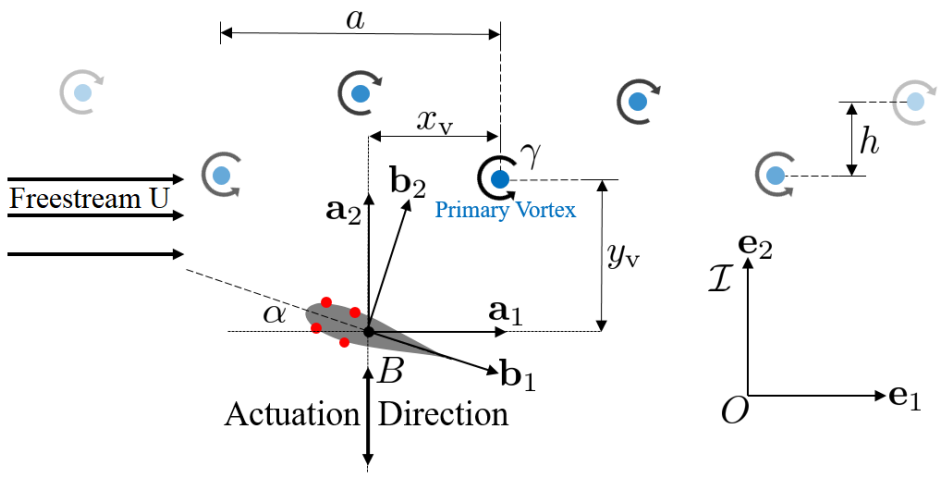

Figure 5.2: Illustration of sensor and control system for the Kármán vortex street. Red circles are pressure sensors.

such that $\mathbf{e}_1 = \mathbf{a}_1$ is pointing downstream. The body-fixed, non-rotating frame $\mathcal{A} = (B, \mathbf{a}_1, \mathbf{a}_2)$ is aligned with $\mathcal{I}$ and centered on the origin of the Joukowski foil. The body-fixed frame $\mathcal{B} = (B, \mathbf{b}_1, \mathbf{b}_2)$ is aligned with $\mathbf{b}_1$ pointing to the trailing edge of the Joukowski foil and is rotated from frame $\mathcal{A}$ by the angle of attack α. The closest anti-clockwise vortex to the Joukowski foil, i.e., the primary vortex, has coordinates $z_v = x_v\mathbf{e_1} + y_v\mathbf{e_2} = x_v + \mathbf{j}y_v$ in frame $\mathcal{A}$, where $\mathbf{j} = \sqrt{-1}$ is the imaginary number. Each vortex has strength γ or $-\gamma$ and the vortex street moves to the right with the freestream speed U. Every like-signed vortex in the street is spaced horizontally by a units. The two lines of vortices are separated vertically by h units. The Joukowski foil is fixed in the $\mathbf{a}_1$ direction and actuates in the $\mathbf{a}_2$ direction by controlling its angle of attack α to generate lift.

The Joukowski foil shape of the robot allows the use of a potential flow model (see Section 2.2 for a review of potential flow). A potential flow model produces the

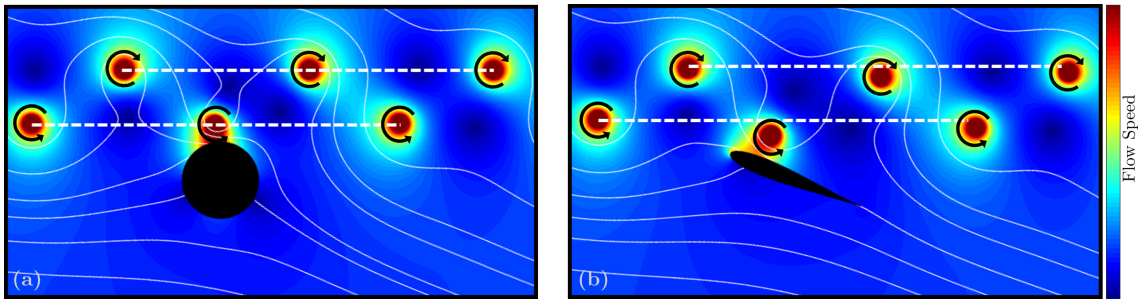

Figure 5.3: Simulated flow field of a lifting cylinder near a Kármán vortex street (a) in the ζ-plane and (b) in the transformed z-plane. The freestream moves from left to right in both panels.

flow velocity at any point from the derivative of a scalar potential function [75, 100, 124]. Potential flow theory characterizes inviscid, irrotational, incompressible flows at low speed flows where viscous effects are minimal. Though in reality the flow is viscous and may separate at large angles of attack, the pressure sensors are grouped towards the leading edge of the Joukowski foil where the flow is attached and the model remains valid [75]. Section 5.1.1 presents the flow over a cylinder at a non-zero angle of attack and the corresponding flow induced by a Kármán vortex street. An altered version of the Milne-Thomson Circle Theorem maintains the cylinder as a boundary condition. Section 5.1.2 presents the Joukowski transformation that converts flow past a cylinder to flow past an airfoil and derives the condition on the circulation around the cylinder to maintain the Kutta condition. Section 5.1.3 uses Bernoulli's equation to derive the measurement equation that gives the pressure difference between two sensors in the artificial lateral line as a function of the three states of the vortex street.

Figure 5.3 shows the flow in the pre-transform ζ-plane and in the post-transform

z-plane, in which the cylinder is transformed into an airfoil. Note that the vortices are in a straight line only in the ζ-plane; the Joukowski transformation has an unintended effect of shifting the position of vortices near the cylinder. As seen in Fig. 5.3, this discrepancy from a straight line is not severe (a more technical discussion follows in subsequent sections) and only affects vortices very near the foil. In practice, this shortcoming of the flow model did not affect the ability to estimate the location of vortices since the discrepancy was so small.

5.1.1 Flow in the circle plane

Modeling flow around a cylinder is a well known application of potential flow theory. The potential flow $F_{\mathrm{C}}(\zeta)$ around a cylinder centered at location ζ_0 in the complex plane is modeled as the summation of uniform flow, a doublet, and a vortex [75]:

$$F_{\mathrm{C}}(\zeta) = U(\zeta - \zeta_0)e^{-\mathbf{j}\alpha} + \frac{Ur_0^2}{\zeta - \zeta_0}e^{\mathbf{j}\alpha} - \mathbf{j}\frac{\Gamma_{\mathrm{C}}}{2\pi}\log\left(\frac{\zeta - \zeta_0}{r_0}\right), \tag{5.1}$$

where U is the flow speed, α is the angle of attack, r_0 is the radius of the cylinder, and Γ_{C} is the circulation strength. In potential flow, the velocity field of a potential flow $f(z)$ is given by the complex conjugate of the derivative of the potential $f(z)$ [75], i.e.,

$$w(z) = u(z) - \mathbf{j}v(z) = \frac{\mathrm{d}f}{\mathrm{d}z},$$

where $u(z)$ and $v(z)$ are the horizontal and vertical components of the velocity. The true velocity field is found by taking the complex conjugate, $\overline{w(z)} = u(z) + \mathbf{j}v(z)$.

The conjugate velocity field for the lifting cylinder in the ζ-plane is

$$\frac{\mathrm{d}F_{\mathrm{C}}}{\mathrm{d}\zeta} = Ue^{-\mathbf{j}\alpha} - U\left(\frac{r_0}{\zeta-\zeta_0}\right)^2 e^{\mathbf{j}\alpha} - \mathbf{j}\frac{\Gamma_{\mathrm{C}}}{2\pi}\frac{1}{\zeta-\zeta_0}. \tag{5.2}$$

From Ref. [73], the potential function for a Kármán vortex street is

$$\begin{aligned} F_{\mathrm{K}}(\zeta) &= \mathbf{j}\frac{\gamma}{2\pi}\Bigg[\log\sin\frac{\pi}{a}(\zeta-\zeta_{\mathrm{v}}) \\ &\qquad -\log\sin\frac{\pi}{a}(\zeta-(\frac{1}{2}a+\mathbf{j}h)-\zeta_{\mathrm{v}})\Bigg]. \end{aligned}$$

Altering this potential for a Kármán vortex street inclined from the real axis at an angle α yields

$$\begin{aligned} F_{\mathrm{K}_\alpha}(\zeta) &= \mathbf{j}\frac{\gamma}{2\pi}\Bigg[\log\sin\left(\frac{\pi}{a}(\zeta-\zeta_{\mathrm{v}})e^{-\mathbf{j}\alpha}\right) \\ &\qquad -\log\sin\left(\frac{\pi}{a}\left((\zeta-\zeta_{\mathrm{v}})e^{-\mathbf{j}\alpha}-(\frac{1}{2}a+\mathbf{j}h)\right)\right)\Bigg]. \end{aligned} \tag{5.3}$$

The complex potential Eqn. (5.3) produces singularities (vortices) at $\zeta = \zeta_{\mathrm{v}} + Nae^{\mathbf{j}\alpha}$ and $\zeta = \zeta_{\mathrm{v}} + Nae^{\mathbf{j}\alpha} + (\frac{1}{2}a+\mathbf{j}h)e^{\mathbf{j}\alpha}$, where $N = 0, \pm1, \pm2, \ldots$.

Next, add the potential for a lifting cylinder Eqn. (5.1) to the potential for a Kármán vortex street Eqn. (5.3) to obtain the potential of a cylinder in a vortex street. To maintain the lifting cylinder as a boundary in the flow, $F_{\mathrm{K}_\alpha}(\zeta)$ must be modified with the Milne-Thomson Circle Theorem [100],

$$w(z) = f(z) + \overline{f}\left(\frac{r_0^2}{z}\right), \tag{5.4}$$

which allows any potential flow $f(z)$ to be augmented to include a cylinder of arbitrary radius r_0 placed at the origin of the coordinate system. As will be shown in Section 5.1.2, it is necessary to impose a cylindrical boundary condition at an arbitrary center, not the origin. (A thorough proof of the Circle Theorem can be

found in Ref. [98, Section 2.1].) The key to the proof of Eqn. (5.4) is that for a point z on a circle C centered at the origin with radius r_0, the complex conjugate is $\overline{z} = r_0^2/z$. To derive the Circle Theorem about an off-origin cylinder, we need only to find the complex conjugate of a point on a circle centered at z_0, which can be shown by substitution to be $\overline{z} = r_0^2/(z - z_0) + \overline{z_0}$. The Circle Theorem then becomes

$$w(z) = f(z) + \overline{f}\left(\frac{r_0^2}{z - z_0} + \overline{z_0}\right). \tag{5.5}$$

(An alternate derivation of the off-origin Circle Theorem using stream functions can be found in Ref. [125, Corollary 1].)

Applying Eqn. (5.5) to the Kármán vortex street complex potential Eqn. (5.3) yields

$$\begin{aligned} F_{\mathrm{K}_\alpha^\circ}(\zeta) = \mathbf{j}\frac{\gamma}{2\pi}\Bigg[&\log\sin\left(\frac{\pi}{a}(\zeta - \zeta_\mathrm{v})e^{-\mathbf{j}\alpha}\right) \\ &- \log\sin\left(\frac{\pi}{a}\left(\frac{r_0^2}{\zeta - \zeta_0} + \overline{\zeta_0} - \overline{\zeta_\mathrm{v}}\right)e^{\mathbf{j}\alpha}\right) \\ &- \log\sin\left(\frac{\pi}{a}\left((\zeta - \zeta_\mathrm{v})e^{-\mathbf{j}\alpha} - (\frac{1}{2}a + \mathbf{j}h)\right)\right) \\ &+ \log\sin\left(\frac{\pi}{a}\left(\left(\frac{r_0^2}{\zeta - \zeta_0} + \overline{\zeta_0} - \overline{\zeta_\mathrm{v}}\right)e^{\mathbf{j}\alpha} - (\frac{1}{2}a - \mathbf{j}h)\right)\right)\Bigg], \end{aligned} \tag{5.6}$$

where r_0 is the radius of a cylinder centered at ζ_0 as in Eqn. (5.1), ζ_v is the location of the primary vortex in the Kármán vortex street, and γ is the vortex strength. This complex potential represents the flow field of a Kármán vortex street augmented to include the lifting cylinder (which will be transformed to become an airfoil) as a

streamline of the flow. The conjugate velocity field is

$$\begin{aligned}\frac{\mathrm{d}F_{\mathrm{K}^{\circ}_{\alpha}}}{\mathrm{d}\zeta} = \mathbf{j}\frac{\gamma}{2a}\Bigg[&\cot\left(\frac{\pi}{a}(\zeta-\zeta_{\mathrm{v}})e^{-\mathbf{j}\alpha}\right)e^{-\mathbf{j}\alpha} \\ &-\cot\left(\frac{\pi}{a}\left(\frac{r_0^2}{\zeta-\zeta_0}+\overline{\zeta_0}-\overline{\zeta_{\mathrm{v}}}\right)e^{\mathbf{j}\alpha}\right)e^{\mathbf{j}\alpha} \\ &-\cot\left(\frac{\pi}{a}\left((\zeta-\zeta_{\mathrm{v}})e^{-\mathbf{j}\alpha}-(\frac{1}{2}a+\mathbf{j}h)\right)\right)e^{-\mathbf{j}\alpha} \\ &+\cot\left(\frac{\pi}{a}\left(\left(\frac{r_0^2}{\zeta-\zeta_0}+\overline{\zeta_0}-\overline{\zeta_{\mathrm{v}}}\right)e^{\mathbf{j}\alpha}-(\frac{1}{2}a-\mathbf{j}h)\right)\right)e^{\mathbf{j}\alpha}\Bigg].\end{aligned} \tag{5.7}$$

Adding Eqn. (5.1) and Eqn. (5.6) yields the total potential flow of a lifting cylinder in the flow field of a Kármán vortex street,

$$F_{\mathrm{T}}(\zeta) = F_{\mathrm{C}}(\zeta) + F_{\mathrm{K}^{\circ}_{\alpha}}(\zeta). \tag{5.8}$$

Similarly, adding Eqn. (5.2) and Eqn. (5.7) yields the total conjugate velocity

$$W_{\mathrm{T}}(\zeta) = \frac{\mathrm{d}F(\zeta)}{\mathrm{d}\zeta} = \frac{\mathrm{d}F_{\mathrm{C}}(\zeta)}{\mathrm{d}\zeta} + \frac{\mathrm{d}F_{\mathrm{K}^{\circ}_{\alpha}}(\zeta)}{\mathrm{d}\zeta}. \tag{5.9}$$

A simulation of this flow field in the pre-transform ζ-plane can be seen in Figure 5.3(a).

5.1.2 Flow in the foil plane

The Joukowski transformation allows the potential flow over a cylinder to be used in order to calculate the flow over an airfoil, the parameters of which are chosen to resemble the cross-section of a fish. The transformation is given by [75]

$$z(\zeta) = \zeta + \frac{c^2}{\zeta}, \tag{5.10}$$

where $c = \ell/4$ is the quarter-chord length and ℓ is the chord length (the length of the fish-shaped body). The center ζ_0 and radius r_0 of the cylinder in the ζ-plane

determine the geometry of the airfoil produced by the Joukowski transformation. The center and radius are [75]

$$\zeta_0 = c\left(\frac{-4}{3\sqrt{3}}\frac{t_\mathrm{a}}{\ell} + 2\mathbf{j}\frac{h_\mathrm{a}}{\ell}\right) \tag{5.11}$$

$$r_0 = \left(\frac{\ell}{4} + \frac{t_\mathrm{a}}{3\sqrt{3}}\right), \tag{5.12}$$

where h_a is the max height of the camber line from the chord line and t_a is the max thickness of the airfoil. For this work an inflexible and uncambered airfoil is used, so $h_\mathrm{a} = 0$.

The conjugate velocity at a point z in the z-plane is found using the derivative of the Joukowski transformation [75], i.e.,

$$\begin{aligned} W(z) = \frac{\mathrm{d}F_\mathrm{T}}{d\zeta}\frac{\mathrm{d}\zeta}{dz} &= \frac{\mathrm{d}F_\mathrm{T}}{\mathrm{d}\zeta}\left(\frac{\mathrm{d}z}{\mathrm{d}\zeta}\right)^{-1} \\ &= W_\mathrm{T}(\zeta(z))\left(1 - \left(\frac{c}{\zeta(z)}\right)^2\right)^{-1} \\ &= u(z) - \mathbf{j}v(z). \end{aligned} \tag{5.13}$$

To find the velocity around the airfoil at point z, Eqn. (5.13) must be evaluated at the corresponding point in the ζ-plane by the inverse Joukowski transformation [126]

$$\zeta(z) = \frac{1}{2}\left(z + \mathrm{sgn}\left(\mathrm{Re}(z)\right)\sqrt{z^2 - 4r_0^2}\right). \tag{5.14}$$

A simulation of this flow field in the post-transform z-plane is in Figure 5.3(b). The z-plane is the physical plane, whereas the ζ-plane is a convenient, non-physical space used to perform calculations. Note that since the vortex street model is defined in the ζ-plane, vortices are deviated slightly from the intended pattern in the z-plane after the Joukowski transformation. However, the error in vortex location due to

the transformation will not exceed $r_0 - t_a/2$, the maximum distance a point on the cylinder's surface is displaced by the Joukowski transformation. For the foil used in the experimental demonstration (Section 5.5), this deviation is 2 cm when a vortex is on the surface of the foil, but quickly decays as the vortex advects with the flow. Due to the smoothing effect of the Bayesian filter and the fact that most measurements are taken when the vortices are not exactly on the surface of the foil, the deviation between modeled and actual vortex location did not prevent successful use of the model in real-time vortex location estimation.

The circulation of the lifting cylinder Γ_C in Eqn. (5.1) remains a free parameter, but can be prescribed by the Kutta condition [75]. In this context, the Kutta condition states that the trailing edge of the airfoil must be a stagnation point in order to avoid non-physical infinite velocities around the sharp trailing edge [75]. Through the Joukowski transformation, the trailing edge of the airfoil corresponds to the point in the ζ-plane where the cylinder intersects the real axis. The angle from the center of the cylinder to the trailing edge point is $\theta_0 = -\alpha - 2h_a/\ell$ [75]. To solve for Γ_C, find the tangential and radial components of the velocity with respect to the center of the cylinder and solve for the circulation that results in a stagnation point at the trailing edge. Changing to polar coordinates centered on the cylinder by substituting $\zeta = \zeta_0 + re^{\mathbf{j}\theta}$ into Eqn. (5.9) yields

$$\tilde{W}_T(r,\theta) = W_T(\zeta) = W_T(\zeta_0 + re^{\mathbf{j}\theta}).$$

The radial u_r and tangential u_θ components of a complex velocity are [75]

$$u_r(r,\theta) - \mathbf{j}u_\theta(r,\theta) = \tilde{W}_T(r,\theta)e^{\mathbf{j}\theta},$$

which implies

$$\begin{aligned} u_r &= \mathrm{Re}\left(\tilde{W}_{\mathrm{T}}(r,\theta)e^{\mathbf{j}\theta}\right) \\ u_\theta &= -\mathrm{Im}\left(\tilde{W}_{\mathrm{T}}(r,\theta)e^{\mathbf{j}\theta}\right). \end{aligned} \tag{5.15}$$

Substituting $r = r_0$ and $\theta = \theta_0 = -\alpha - 2h_{\mathrm{a}}/\ell$ in Eqn. (5.15), u_r evaluates to 0 as expected, because the cylinder was chosen to be a boundary in the flow. Setting $u_\theta = 0$ and solving for Γ_{C} yields the circulation that satisfies the Kutta condition

$$\Gamma_{\mathrm{C}} = 2r_0\pi\left[\mathrm{Im}\left(\frac{\mathbf{j}\gamma e^{\mathbf{j}\theta_0}}{2a}(A_1 + A_2 + A_3 - A_4)\right) \quad + 2U\sin(\theta_0)\right], \tag{5.16}$$

where $\theta_0 = -\alpha - h_a/\ell$,

$$\begin{aligned} A_1 &= e^{\mathbf{j}(\alpha-2\theta_0)}\cot\left[\frac{\pi}{a}e^{\mathbf{j}\alpha}\left(\overline{\zeta_0} - \overline{\zeta_{\mathrm{v}}} + r_0 e^{-\mathbf{j}\theta_0}\right)\right], \\ A_2 &= e^{-\mathbf{j}\alpha}\cot\left[\frac{\pi}{a}\left(\frac{a}{2} + \mathbf{j}h - e^{-\mathbf{j}\alpha}\left(\zeta_0 - \zeta_{\mathrm{v}} + r_0 e^{\mathbf{j}\theta_0}\right)\right)\right], \\ A_3 &= e^{-\mathbf{j}\alpha}\cot\left[\frac{\pi}{a}e^{-\mathbf{j}\alpha}\left(\zeta_0 - \zeta_{\mathrm{v}} + r_0 e^{\mathbf{j}\theta_0}\right)\right], \text{ and} \\ A_4 &= e^{\mathbf{j}(\alpha-2\theta_0)}\cot\left[\frac{\pi}{a}\left(-\frac{a}{2} + \mathbf{j}h + e^{\mathbf{j}\alpha}\left(\overline{\zeta_0} - \overline{\zeta_{\mathrm{v}}} + r_0 e^{-\mathbf{j}\theta_0}\right)\right)\right]. \end{aligned}$$

The mathematics allow for any value of Γ_{C}, but only the value that leads to flow leaving smoothly at the trailing edge is physically realistic. With the analytical solution to the bound vorticity which maintains the Kutta condition as a function of vortex locations, the potential flow model is complete.

5.1.3 Artificial lateral line

The complete potential flow model presented in the previous section provides a means to calculate the velocity field as a function of vortex strength and location.

However, the artificial lateral line is composed of pressure sensors which are only indirectly sensitive to flow velocity. Bernoulli's equation combined with the flow velocities modeled above predicts the pressure at a point z in the flow field of a Joukowski foil in a vortex street. Let $p(z)$ denote the static pressure at z, ρ the fluid density, $W(z)$ the velocity at z, g the gravitational acceleration, and Z the elevation. Applying Bernoulli's principle [60] for steady, inviscid, incompressible, irrotational flow yields

$$p(z) + \frac{1}{2}\rho|W(z)|^2 + \rho g Z = \text{constant}. \tag{5.17}$$

In the experiment described in Section 5.5, four pressure sensors are mounted on the body of the Joukowski foil. Inspired by the function of canal neuromasts [127], pressure differences between sensors are measured and modeled to remove the effects of ambient pressure, rather than using the absolute pressure measurements. From Eqn. (5.17), for any two sensor locations z_i and z_j, we have

$$p(z_i) + \frac{1}{2}\rho|W(z_i)|^2 = p(z_j) + \frac{1}{2}\rho|W(z_j)|^2.$$

The pressure difference, $\Delta p_{ij} = p(z_i) - p(z_j)$, is

$$\Delta p_{ij} = \frac{1}{2}\rho\Big[|W(z_j)|^2 - |W(z_i)|^2\Big], \tag{5.18}$$

where $W(z)$ is given by Eqn. (5.13). The measurement model is now complete. Given a vortex street strength and location, the expressions derived in this section model the pressure that would be measured by a sensor in a particular location. This measurement model is used in the next section as an integral part of the estimation of vortex location.

5.2 Vortex street estimation

The estimation of the states of the vortex street is performed by a recursive, grid-based Bayesian filter [101, 102]. The principle of this filter is to use a measurement model that predicts what the measurements from the sensors would be if the state of the system were a particular value in the state space. A measurement model for the vortex street was derived and presented in the previous section. By comparing the measurement predictions of every point in the state space grid with the actual measurement, a multi-dimensional conditional probability density function (PDF) is formed, called the measurement likelihood function. The likelihood function is combined with the *prior* PDF of the previous time step to become the *posterior* PDF according to Bayes' theorem. The posterior then becomes the prior of the next time step after it is forecast forward according to the system dynamics including process noise. The Bayesian filter is a well-tested tool in the controls engineer's chest. Section 2.3 presents the estimation scheme in its most general form. The grid-based Bayesian filter is applied below to estimate the state of a vortex street

In the current framework, the Bayesian filter assimilates pressure difference measurements to estimate the strength, phase, and cross-stream location of the vortex street. Equations (5.9), (5.13), and (5.18) are used in Section 5.1 to model pressure measurements from the sensors. The recursive, grid-based Bayesian filter estimates a set $\mathbf{X}$ of parameters from a set $\mathbf{Y}$ of measurements [101]. Suppose the

instantaneous measurement vector is

$$\mathbf{Y} = \mathscr{H}(\mathbf{X}) + \eta, \tag{5.19}$$

where $\mathscr{H}(\mathbf{X})$ is the (nonlinear) measurement equation (5.18) and η is (Gaussian) sensor noise. With n_{ps} pressure sensors, there are $n_p = n_{ps} - 1$ measurements of linearly independent pressure differences. Note that there are $n_p = (n_{ps}^2 - n_{ps})/2$ total pressure differences among the pressure sensors, but they are not linearly independent. Using redundant pressure sensor differences in the Bayesian filter framework will have the effect of mitigating sensor noise more quickly (in fewer time steps), but each time step will take longer. In this work, the minimum number of linearly independent sensors are used in order to have the maximum update rate to accommodate the real time dynamics of the Joukowski foil under closed-loop control. The measurement vector is

$$\mathbf{Y} = [\Delta p_1, \ \ldots \ , \Delta p_{n_p}]^T \in \mathbb{R}^{n_p}, \tag{5.20}$$

where each pressure difference entry is given by Eqn. (5.18) evaluated using the locations of the pressure sensors in frame $\mathcal{B}$.

5.2.1 Likelihood function

For the grid-based Bayesian filter with Gaussian measurement noise, the likelihood function is the following conditional probability of measurement $\mathbf{Y}$ given state

vector $\mathbf{X}$ [101]:

$$\pi(\mathbf{Y}|\mathbf{X}) = \frac{1}{\sqrt{(2\pi)^n \det(R)}} \exp\left[-\frac{1}{2}(\mathbf{Y} - \mathscr{H}(\mathbf{X}))^T R^{-1}(\mathbf{Y} - \mathscr{H}(\mathbf{X}))\right], \tag{5.21}$$

where n is the dimension of the state space and $R \in \mathbb{R}^{n_p \times n_p}$ is the covariance matrix of the sensor noise. Let m_i be the width of the i^{th} dimension in the n-dimensional state space, then the discrete grid $\mathbf{X} \in \mathbb{R}^{m_1 \times m_2 \times \ldots \times m_n}$ of all expected possible values of the state space is used to evaluate the measurement equation. (For a large number of grid points, this calculation may be computationally intensive.)

5.2.2 Update step (Bayes theorem)

Bayes' formula allows each new measurement and its likelihood function Eqn. (5.21) to be combined with the prior estimate, yielding the posterior estimate. Let $\mathbf{Y}_k$ be the set of measurements at time t_k, with $k = 1, 2, \ldots$. Then,

$$\pi(\mathbf{X}|\mathbf{Y}_k, \ldots, \mathbf{Y}_1) = \kappa\pi(\mathbf{Y}_k|\mathbf{X})\pi(\mathbf{X}|\mathbf{Y}_{k-1}, \ldots, \mathbf{Y}_1),$$

where κ is a normalizing factor to ensure the posterior integrates to one. After the incorporation of each new measurement, the posterior becomes the prior for the next time step. For the initial time step, we choose a uniform prior. The notation $\pi(\mathbf{X}|\mathbf{Y})$ is used for the posterior $\pi(\mathbf{X}|\mathbf{Y}_k, \ldots, \mathbf{Y}_1)$ at an arbitrary value of k.

5.2.3 Forecast step

The posterior estimate $\pi(\mathbf{X}|\mathbf{Y})$ is an n-dimensional matrix with each dimension corresponding to one of the states in the parameter space. The width m_i of each

dimension is determined by how fine a grid is chosen for the Bayesian filter. The computational time needed for each time step increases with the size of $\pi(\mathbf{X}|\mathbf{Y})$. The time evolution of the posterior (in order to become the prior of the next time step) is accomplished by shifting the values of the PDF according to the continuous dynamics of Section 5.3. The angle of attack α is a known input and is assumed constant over each time step, allowing each point in the posterior to be forecast using a numerical solver such as `ode45` in MATLAB.

5.2.4 Process noise

Process noise is modeled by convolving the PDF with an n-dimensional, zero-mean Gaussian kernel as a numerical approximation of the Fokker-Planck equation with diffusion only [103]. This operation has a blurring effect on the PDF as time goes on. In the absence of new measurements, the PDF becomes uniform as time goes to infinity.

5.2.5 Parameters to estimate

The full flow field given in Eqn. (5.13) is determined by the geometry of the Joukowski airfoil, the circulation of the airfoil found by the Kutta condition in Eqn. (5.16), and the parameters of the Kármán vortex street. Each parameter to be estimated in the Bayesian filter framework greatly increases the computational time needed at each time step. It is therefore advantageous to reduce the number of parameters in the estimation state space as much as possible. For example, the

geometry of the foil is known by design and Γ_{C} is a function of the other states of the system.

There are seven parameters that uniquely determine the flow field: U (the freestream flow speed), α (the angle of attack of the airfoil), γ (the strength of each vortex in the street), a (the horizontal spacing of the vortices), h (the vertical spacing of the vortices), x_{v} (the horizontal location of the vortex street in frame $\mathcal{A}$), and y_{v} (the vertical location of the vortex street in frame $\mathcal{A}$). Previous work [71] demonstrated the use of pressure sensors to estimate the free-stream speed of a flow as well as the angle of attack. Thus, assume here that flow speed U and angle of attack α are estimated by an independent, parallel filter.

The stability analysis in Ref. [73] shows that the vertical spacing h of the vortices is directly proportional to the horizontal spacing a by $h = a\frac{1}{\pi}\sinh^{-1}(1) \approx 0.2805a$, so h can be removed from the parameter space. The horizontal spacing a is related to the diameter of the upstream obstacle shedding the vortices through the Strouhal number St. For low-frequency vortex shedding [128],

$$St = \frac{fD}{U} \approx 0.2, \tag{5.22}$$

where f is the frequency of shedding, D is the obstacle diameter, and U is the flow speed. The frequency obeys $f = U/a$, so if the obstacle diameter is known, then a may be calculated. Finally, because $x_{\mathrm{v}} = \mathrm{Re}(z_{\mathrm{v}})$ measures the horizontal distance to the closest anti-clockwise vortex in an infinite line of vortices moving at constant speed U, this distance is represented by a phase angle

$$\phi = 2\pi\frac{x_{\mathrm{v}}}{a},\ \phi \in [-\pi,\ \pi). \tag{5.23}$$

A phase angle of $\phi = 0$ corresponds to when the primary vortex is horizontally in line with the Joukowski foil; $\phi = \pi$ is when the primary vortex is at $x_{\mathrm{v}} = a/2$ and a new vortex becomes the primary vortex. In this way, the parameter space is reduced to three variables: ϕ (the phase of the vortex street), y_{v} (the cross-stream distance to the primary vortex of the street), and γ (the strength of the street). Though only the phase and cross-stream distance are necessary for the controller described in Section 5.3, the vortex strength must be estimated to have the full mathematical description of the vortex state that is necessary for the Bayesian filter. For the Kármán vortex street, the grid of all possible values is three-dimensional with $\mathbf{X}_{\mathrm{K}^{\circ}_{\alpha}} \in \mathbb{R}^{m_\phi \times m_{y_{\mathrm{v}}} \times m_\gamma}$.

5.3 Dynamics and flow-relative control

To design a controller, perform the observability analysis of Section 5.4, and perform the forecast step of the Bayesian filter, a model of the system dynamics is needed. Several assumptions about the dynamics of the Joukowski foil and vortices are needed to perform real-time estimation. The first assumption is that the vortices are constant strength and do not decay as they move downstream.

The second assumption is that the effect of the vortex street on the Joukowski foil is ignored. In order to account for these dynamics, the lift L in the $\mathbf{a}_1$ direction (see Figure 5.2) would be given by the Kutta-Joukowski Theorem [75] as $L = \rho U \Gamma_{\mathrm{C}}$, where Γ_{C} from Eqn. (5.16) is a function of angle of attack α. This assumption does not have theoretical justification, but was needed in order for the control loop to run

fast enough to operate in real time. In practice, the estimator and controller were robust enough such that any error between the actual dynamics and the simplified dynamics here was quickly removed due to the fast convergence of the estimator. In the absence of a vortex street, i.e., in a uniform flow, this lifting law reduces to the thin airfoil theory below.

The third assumption is that the airfoil does not affect the path of the vortices in the street. Each vortex in the street deflects from its nominally straight path as it interacts with the obstruction of the airfoil. This effect is well modeled in potential flow using Routh's Rule [129,130], but individual movement of vortices in the vortex street is not represented in the current framework because the measurement equation Eqn. (5.18) assumes the entire vortex street can be represented by one set of planar coordinates. The error due to this effect is mitigated because the vortices are only deflected once they are downstream of the airfoil. Previous work [126] has shown that the most effective sensor placement is near the leading edge of the Joukowski foil and is thus less effected by the vortex deflection than if the sensors were placed closer to the trailing edge.

5.3.1 Thin airfoil theory

For the cross-stream coordinate y_{v} dynamics, adopt the lifting law from thin airfoil theory [60]. Thin airfoil theory shows that the sectional lift coefficient $c_l = 2\pi\alpha$ and

$$L = c_l q S = \rho \pi U^2 S \alpha, \tag{5.24}$$

where S is the surface area of the foil. We model the cross-stream dynamics as

$$m\ddot{y}_{\mathrm{v}} = -L - b\dot{y}_{\mathrm{v}}, \tag{5.25}$$

where b is a damping term and the negative sign on L is included because y_{v} measures the vertical displacement of the primary vortex relative to the center of the foil. If the Joukowski foil has positive lift, y_{v} decreases as the foil moves in the positive $\mathbf{a}_2$ direction.

5.3.2 Flow-relative phase dynamics

Because the Joukowski foil is fixed in the downstream direction, the phase angle ϕ (which keeps track of the $\mathbf{a}_1$ coordinate, x_{v}, according to Eqn. (5.23)) is unaffected by the foil's movement and the vortices advect in the flow at speed U. The downstream dynamics are

$$\dot{\phi} = 2\pi\frac{U}{a} = \text{constant}. \tag{5.26}$$

Finally, the vortex strength dynamics are

$$\dot{\gamma} = 0,$$

because of the assumption that the vortices do not decay as they travel downstream.

5.3.3 Tracking feedback linearization

The goal of the closed-loop control here is to track a phase-dependent reference trajectory $y_{\mathrm{v,ref}} = y_{\mathrm{v,ref}}(\phi)$, meaning for any given phase ϕ there is a reference

vertical position y_{v} that should be achieved by actuating the angle of attack α of the Joukowski foil. Note that y_{v} is the position of the vortex street in body-fixed, non-rotating frame $\mathcal{A}$ (see Figure 5.2) so if the Joukowski foil moves in the $\mathbf{e_2}$ direction in the inertial frame $\mathcal{I}$, y_{v} decreases. All calculations within the estimator and controller are performed in body-fixed frame $\mathcal{B}$. If the Kármán vortex street never moves in the cross-stream direction, y_{v} still changes if the Joukowski foil translates in the cross-stream direction. Let $\hat{\phi}$ and $\hat{y}_{\text{v}}$ represent the maximum likelihood estimate of the relative phase and cross-stream position of the vortex street from $\pi(\mathbf{X}|\mathbf{Y})$, the three-dimensional PDF output every time step by the Bayesian filter (see Section 5.2). Although the posterior is only updated once per time step, the relatively fast update rate of 20 Hz allows the system to be well characterized by continuous dynamics. The reference trajectory $y_{\text{v,ref}} = y_{\text{v,ref}}(\hat{\phi})$ is a function of the estimate of the phase of the vortex street. Letting $e_1 = \hat{y}_{\text{v}} - y_{\text{v,ref}}$ and $e_2 = \dot{\hat{y}}_{\text{v}} - \dot{y}_{\text{v,ref}}$, the error dynamics are

$$\begin{aligned} \dot{e}_1 &= e_2 \\ \dot{e}_2 &= -\frac{1}{m}\rho\pi U^2 S\alpha - \frac{b}{m}\dot{\hat{y}}_{\text{v}} - \ddot{y}_{\text{v,ref}}, \end{aligned}$$

where the cross-stream dynamics Eqn. (5.24) and Eqn. (5.25) have been used. Choose a tracking PD controller [66] for the angle of attack α,

$$\alpha = -\frac{m}{\rho U^2 \pi S}\left(\ddot{y}_{\text{v,ref}} + \frac{b}{m}\dot{\hat{y}}_{\text{v}} - k_p e_1 - k_d e_2\right), \tag{5.27}$$

with control gains $k_p = k_d = 5$. Damping constant $b = 15\,\text{kg}\,\text{s}^{-1}$ was found to best match the experimental dynamics through trial and error. This damping term

represents the damping effect of the water on the Joukowski foil as well as the nonzero friction of the air-bearing system. The stable, closed-loop error dynamics are

$$\begin{aligned} \dot{e}_1 &= e_2 \\ \dot{e}_2 &= -k_p e_1 - k_d e_2, \end{aligned}$$

with eigenvalues of

$$\lambda = -\frac{k_d}{2} \pm \frac{\sqrt{k_d^2 - 4k_p}}{2},$$

which have negative real parts since $k_p, k_d > 0$.

5.4 Observability-based path-planning

The observability of a system quantifies the capability of a set of outputs $\mathbf{Y}$ to be used to infer the internal states $\mathbf{X}$ of the system on which the outputs depend. This concept is used here to find the reference trajectory through the vortex street that leads to the best estimates of the street parameters. Traditional observability gives a binary answer to the question of whether measurements $\mathbf{Y}$ can be used to estimate states $\mathbf{X}$ and, for nonlinear systems such as the one here, often requires taking Lie derivatives of the system dynamics and evaluating the observability rank condition [131]. Empirical observability instead gives a quantitative measure of how easily observed a system is and requires only the ability to simulate the system dynamics. Krener and Ide conceived the *empirical observability gramian* W_o [131]. For the nonlinear system

$$\dot{\mathbf{X}} = f(t, \mathbf{X}) \text{ and } \mathbf{Y} = \mathscr{H}(t, \mathbf{X}),$$

$$W_o(i,j) = \frac{1}{4\epsilon^2}\int_0^\tau (\mathbf{Y}^{+i} - \mathbf{Y}^{-i})^\top (\mathbf{Y}^{+j} - \mathbf{Y}^{+j})\mathrm{d}t, \tag{5.28}$$

where $\mathbf{Y}^{\pm i}$ is the measurement produced from the state $\mathbf{X}^{\pm i} = \mathbf{X} \pm \epsilon\mathbf{e}^i$, and $\epsilon\mathbf{e}^i$ is a small perturbation along the i^{th} unit vector in $\mathbb{R}^n$, with $i = 1, \ldots, n$. The inverse of the minimum singular value of W_o on a time interval $[0, \tau]$ is the *local unobservability index*, $\nu = 1/\sigma_{\min}(W_o)$. Since this metric requires simulating the system dynamics, it depends on parameters specific to experimental conditions such as sensor placement, vortex strength, foil geometry, etc., and therefore cannot be used to compare observability between different configurations. It is, however, useful for comparing different trajectories with the same experimental configuration. The path with the lowest unobservability index will lead to the best estimate of the parameter space.

5.4.1 Unobservability index

To choose the path $y_{\mathrm{v,ref}}(\phi)$, the unobservability indices ν calculated along sinusoidal trajectories of varying phase and amplitude are compared. Sinusoidal trajectories are examined because of the periodic structure of the vortex street and the sinusoidal nature of Kármán gaiting behavior in fish. By simulating the system dynamics given in Section 5.3 with the control law for α described therein, Eqn. (5.28) provides the local unobservability index for each trajectory. Nominal initial conditions are set to start on the reference trajectory. The vortex street spacing, vortex strength, flow speed, foil geometry, and sensor configuration match those in the experiment described in Section 5.5. Figure 5.4 shows the local unobservabiltiy

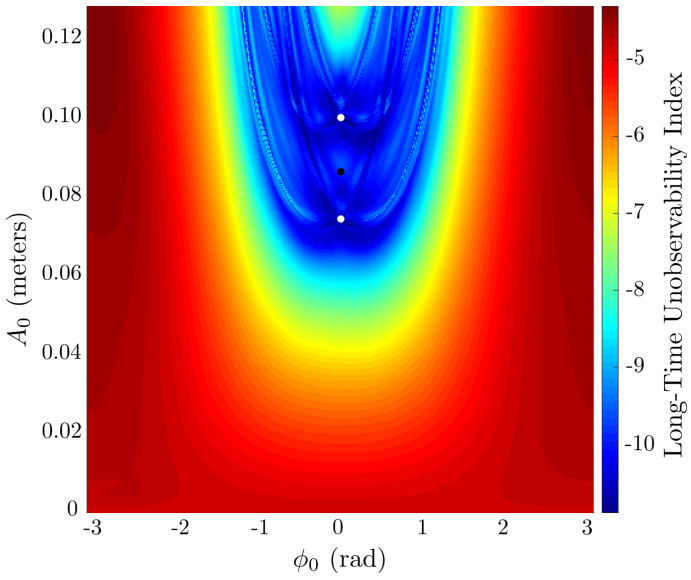

Figure 5.4: Long-time unobservability index for sinusoidal trajectories of the form $A_0 \cos(\phi + \phi_0) - h/2$ through the (ϕ, y_v) plane. The white circles represent minima of the test grid. The black circle represent the path followed in the experiment.

index for each sinusoidal reference trajectory and was generated with the measurement model presented above. The minima on this graph indicated by white circles are the paths of the Joukowski foil leading to the best estimates of the parameters $\mathbf{X}_{\mathrm{K}_\alpha^\circ}$.

The corresponding optimal paths are shown in Figure 5.5 in white. Figure 5.5 was generated not by simulating full trajectories with the proper control law, but by selecting initial conditions in the (ϕ, y_v) plane and simulating the dynamics with $\alpha = 0$ for one time step of 0.1 seconds. Figure 5.5 gives a metric for the unobservability for each point in the plane regardless of how that point was reached, referred to here as the short-term unobservability index. In contrast, Figure 5.4 gives a metric for the unobservability of an entire reference trajectory, referred to here

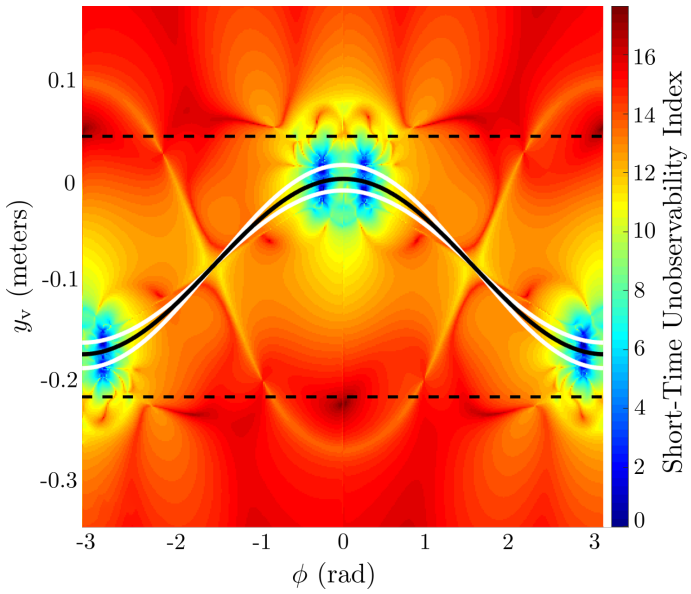

Figure 5.5: Short-time unobservability index at various points in the (ϕ, y_v) plane. White and black curves correspond to the white and black circles in Fig. 5.4. The dashed black lines indicate the width of the test section of the experimental setup described in Section 5.5.

as the long-term unobservability index. Each point in Figure 5.4 corresponds to an entire trajectory through Figure 5.5. The low unobservability index areas in Figure 5.5 are those that bring one of the four pressure sensors close to a vortex in the street. The optimally observable paths shown in white are those that bring the vortices close to these low unobservability index areas, creating a large pressure difference between the sensor pairs and hence a good estimate of the vortex street location and strength.

5.4.2 Bioinspired slaloming and maximally observable paths

For the experimental demonstration described in Section 5.5, the black trajectory was chosen for $y_{\mathrm{v,ref}}$ for three reasons. First, it avoids unmodeled boundary effects of coming too close to the walls of the test section (indicated by black dashed lines). Second, the sensors do not pass directly through the singularity of the vortices as they do for the white trajectories. In the potential flow model, the velocity at the center of each vortex is infinite, which is of course nonphysical, so by avoiding intentional measurements at the singularities, it avoids a discrepancy between the model and the real world. Finally, the black trajectory is very close to the two white trajectories and has a low unobservability index as compared to the rest of the field in Figure 5.4. The chosen path is

$$y_{\mathrm{v,ref1}} = \frac{h}{2}\cos(\phi) - \frac{h}{2}, \tag{5.29}$$

which takes the center of the Joukowski foil (but not the pressure sensors) through the center of each vortex. The offset $-h/2$ ensures that the trajectory is centered

between the upper and lower lines of vortices in the street. It is interesting to note that fish do not adopt this strategy. Instead, they slalom between the vortices capturing some of the energy to propel themselves [76], a behavior known as Kármán gaiting. To demonstrate this path, a second reference trajectory is defined as

$$y_{\mathrm{v,ref2}} = \frac{h}{2}\cos(\phi + \pi) - \frac{h}{2}, \tag{5.30}$$

representing the Kármán gaiting behavior. Figure 5.6 shows the difference between the two reference trajectories that are executed in the experiments described in Section 5.5.

5.5 Experimental demonstration

In order to validate the modeling and estimation scheme presented above, it is necessary to present a practical demonstration in experiment. This section presents the testbed used for experiments to track reference trajectories through a Kármán vortex street and discusses the results in tracking both the optimally observable and the biologically inspired paths.

5.5.1 Testbed

Figure 5.7 shows the experimental testbed for the Kármán vortex street estimation and flow-relative control experiments. A 185 L Loligo flow tank creates a uniform 15 cm/s flow in an 88cm × 25cm × 25cm test section. A stepper motor controls a black acrylic fin that flaps to create vortices at the desired spacing and frequency. The fin extends to the bottom of the flow tank and is parallel to the

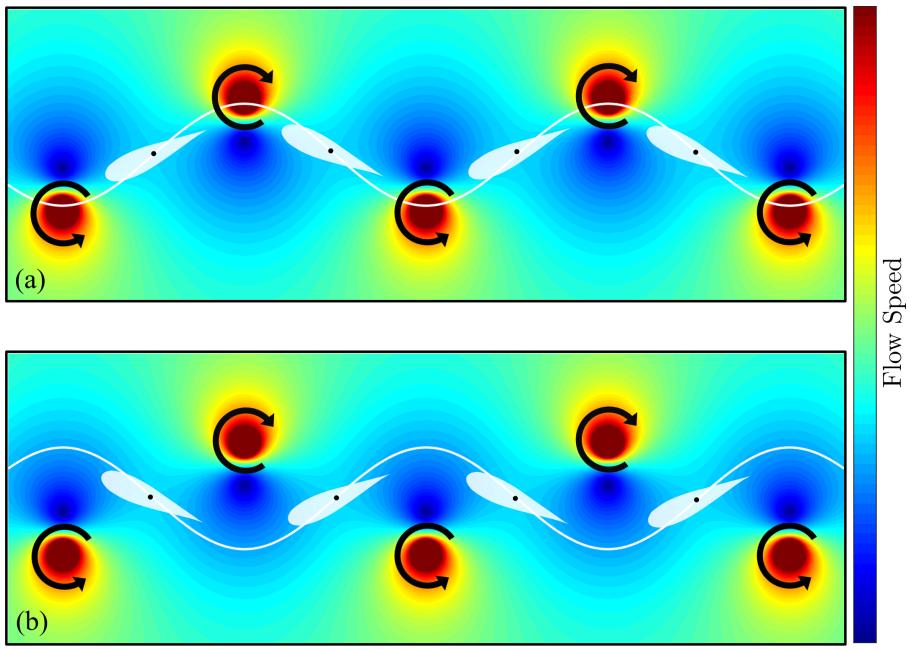

Figure 5.6: (a) Reference trajectory 1, the optimally observable path through the vortex street. The Joukowski foil passes through each vortex in the street. (b) Reference trajectory 2, the slalom path corresponding to Kármán gaiting. Note that this figure is in a flow-fixed frame. In the inertial frame, the Joukowski foil is fixed in the downstream coordinate and the vortices flow past it.

flow until a vortex is generated. The fin then rotates clockwise (or anti-clockwise) and slowly returns to center to create an anti-clockwise (or clockwise) vortex that travels downstream with the freestream. This pattern is consistent with that of a Kármán vortex street shed from an obstacle in the flow. Through the use of dye packets and image processing, the strength of each vortex in the street was empirically determined to be $\gamma \approx 0.0605\,\mathrm{m^2 s^{-1}}$ by measuring the time it took for a dye packet to complete a revolution around a vortex at a particular distance. This method has many possible sources of error and it would be better to use particle image velocimetry techniques for a more robust estimate of vortex strength, but the physical setup of the flow tank made optical access challenging.

The Joukowski foil is suspended in the water from a servomotor that controls the angle of attack directly according to Eqn. (5.27). The servomotor is mounted on a set of nearly frictionless air bearings. The air bearings have a supply of compressed air that is released radially inward towards a 3/4 inch steel shaft, creating a pillow of air that supports the air bearings as they move. This configuration allows the servomotor and Joukowski foil to freely translate in the cross-stream direction, but holds the foil locked at a particular downstream position from the vortex generator. Four Millar pressure sensors are mounted directly on the side of the foil to emulate the lateral line seen in biology. The variance of noise in the pressure sensors was found to be $R_p = 49$ Pa^2. The sensor noise matrix in Eqn. (5.21) is

$$R = \mathrm{diag}(\underbrace{R_p \ \ldots \ R_p}_{n_p}),$$

where R_p is the expected noise variance of the pressure-difference measurements,

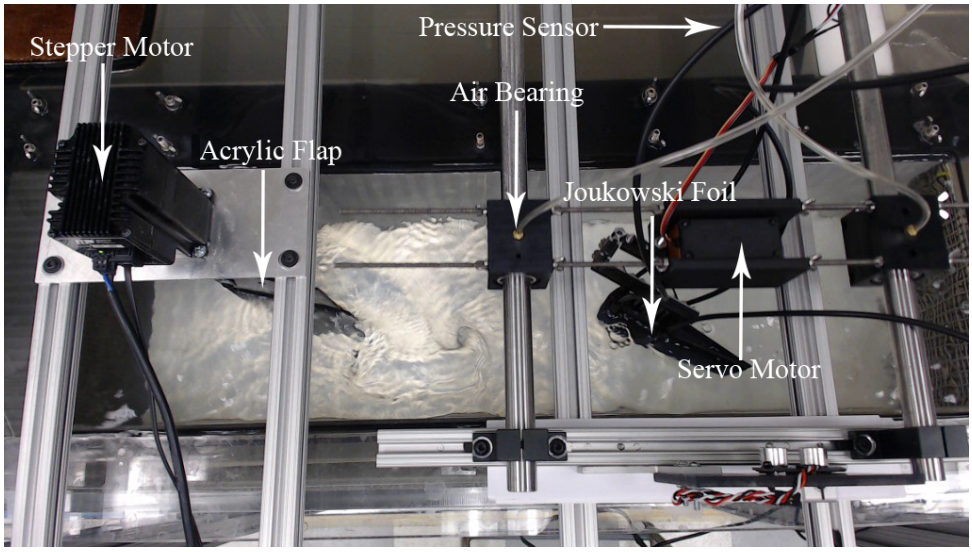

Figure 5.7: The testbed for the vortex street estimation and flow-relative control experiments. A flow tank generates flow from left to right. The Joukowski foil, equipped with four pressure sensors as an artificial lateral line, controls its cross-stream position by actuating a servomotor to control angle of attack. The Joukowski foil is attached to an air-bearing system that allows free movement in the cross-stream direction, but fixes the foil in its downstream position. A stepper motor actuates a fin to create the vortices in the desired vortex street pattern. An overhead camera is used to calculate the ground truth location of the vortices.

found by fitting a Gaussian density to the data collected from the pressure sensors in uniform flow.

Printed from PLA plastic with a MakerBot Replicator, the rigid Joukowski foil has the shape detailed in Section 5.1. The print includes internal cutouts to allow an assembly of 1 cm MakerBeam to mount the foil to the servomotor horn. The length of the Joukowski foil is 15 cm and maximum thickness is 2 cm. The body is uncambered. The height of the body (the span of the foil) is 12 cm and was suspended into the water to leave 2 cm exposed to air and to eliminate any unmodeled flow over the top of the foil. Pressure sensors were mounted on the Joukowski foil at the locations shown in Figure 5.2 and were midway down the depth of the body.

A camera mounted above records the experiments in order for the actual vortex positions to be determined offline through manual pixel selection and a built-in MATALB script to map pixels to the dimensions of the tank. This method relies on the easy visibility of the center of each vortex and therefore does not provide ground truth when the vortices dissipate or are occluded by something in the experimental setup. Particle image velocimetry provides more accurate and robust ground truth data for vortex position, but imaging of this type was precluded here because the bottom of the tank is opaque and the free surface prevents imaging from above.

The estimation, data acquisition, image capture, control calculation, stepper motor, and servomotor are all controlled in real time from a laptop computer running MATLAB. A $30 \times 30 \times 15$ coarse grid of possible points $\mathbf{X}_{\mathrm{K}_\alpha^\circ}$ in the $(\phi, y_\mathrm{v}, \gamma)$ state space was used to update the estimate and control at approximately 20 Hz in order

to have stable convergence to the reference trajectory. Experiments ran for 700 time steps at 20 Hz, equating to nominally 35 second run times (the actual run time varied by up to 2 seconds due to variable computation time per time step and unknown loads on the computer's processor by programs other than MATLAB). The vortices created by the flapper were spaced by $a = 0.6\,\mathrm{m}$, which corresponds to a hypothetical upstream obstacle of diameter 12 cm according to Eqn. (5.22) and a shedding frequency of 0.25 Hz. This yielded approximately 9 cycles per experiment.

5.5.2 Results

Figure 5.8(a-c) shows the time history of the marginal densities of the three states in $\pi(\mathbf{X}|\mathbf{Y})$ for the closed-loop experiment to track the optimally observable reference trajectory given in Eqn. (5.29). The marginal density for each state was formed by summing along the other two states of the three-dimensional probability density at each time step. The initial value of ϕ is plotted instead of the current value for ease of visualization. Integrating Eqn. (5.26) directly and rearranging yields

$$\phi_0 = \phi(t) - 2\pi\frac{U}{a}t, \tag{5.31}$$

the initial value of ϕ. Since this value is constant and the second term is known, a proper estimate of $\phi(t)$ will lead to a constant estimate of ϕ_0. The experiment was successful in actuating the Joukowski foil to pass through each of the vortices after an initial period of larger error. This period of larger error is due to the time it takes the estimator to converge on a particular estimate after the control was turned on.

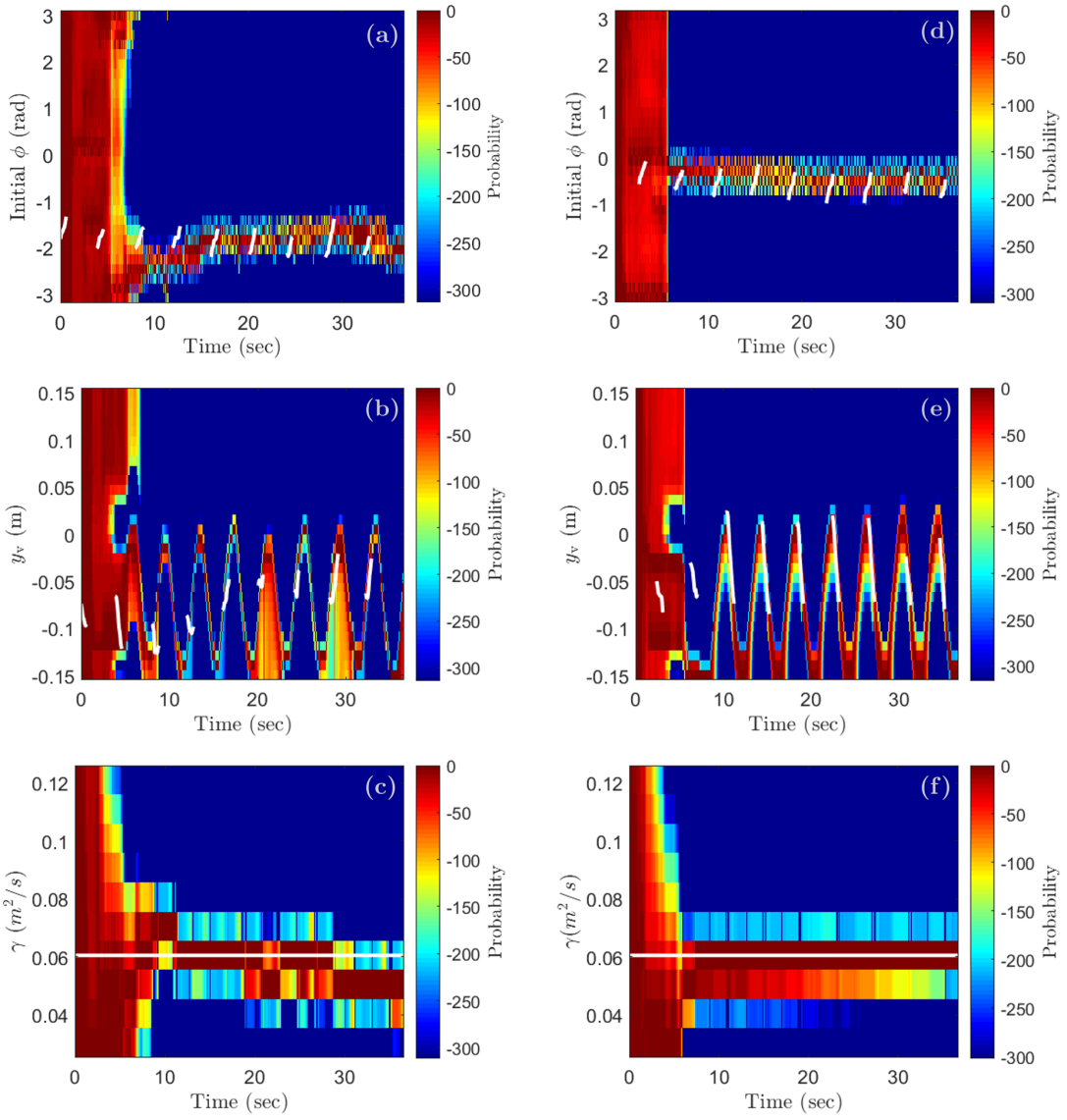

Figure 5.8: Time history of the marginal posteriors from the Bayesian estimator during the closed-loop control experiment in the flow tank. Panels (a,d) show the initial value of ϕ given by Eqn. (5.31), (b,e) y_v, and (c,f) γ. Panels (a-c) correspond to the optimally observable reference trajectory Eqn. (5.29) and panels (e-f) correspond to the Kármán gaiting trajectory Eqn. (5.30). Feedback control starts at 5 seconds.The white lines indicate the ground truth.

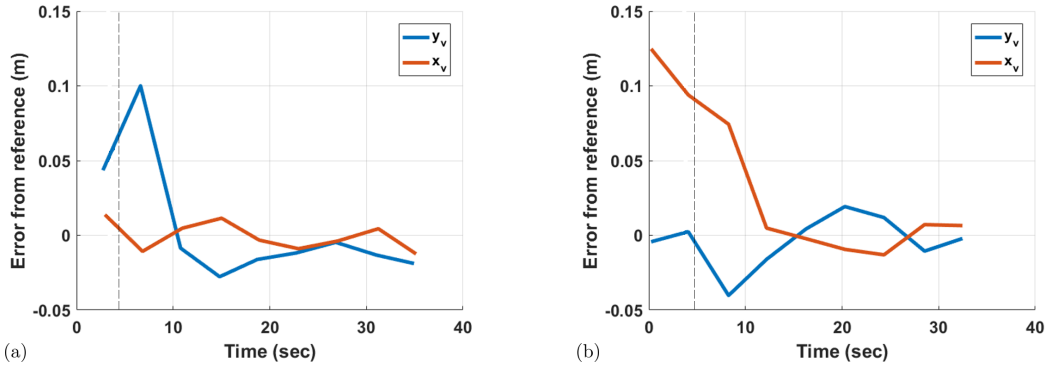

Figure 5.9: Error between reference and ground truth of x_{v} and y_{v} over the Kármán vortex street experiment for the (a) optimal observability and (b) Kármán gaiting trajectory. x_{v} is shown rather than the non-dimensionalized ϕ to more easily compare the errors in the two states. Feedback control starts at 5 seconds, indicated by the dashed vertical lines.

Due to the noisy sensors, it takes many measurements for the filter to determine the true vortex locations. Figure 5.9(a) shows the time history of the error from the reference trajectory.

Figure 5.8(d-f) shows the time history of the marginal densities of the three states in $\pi(\mathbf{X}|\mathbf{Y})$ for the closed-loop experiment to track the Kármán gaiting trajectory given in Eqn. (5.30). The experiment was successful in actuating the Joukowski foil to slalom through the vortex street after an initial period of larger error. Figure 5.9(b) shows the time history of the error from the reference trajectory.

The estimator and controller were successful in both closed-loop control experiments, meaning that there was stable convergence to the reference trajectories and errors tended to zero. For the first five seconds for each experiment, the controller was disabled and the angle of attack was kept at $\alpha = 0$. During this period, the

vortices did not come near the pressure sensors on the Joukowski foil and thus the estimate had a very large variance. In both cases, after the controller was enabled, the Joukowski foil came close to the vortices in the street (by design in the optimally observable case and by initial error in the slaloming case) and the variance in the estimate was reduced due to the larger difference in the pressure sensor measurements at this close proximity. This result agrees with the result from the observability analysis in Section 5.4, which showed that better estimates of the state arise when the fish is close to the vortices. Notice that after the initial five second period, the variance in the estimate of y_{v} in Fig. 5.8(b) (the optimally observable path) is lower than that of Fig. 5.8(e) (the Kármán gaiting path) because the latter trajectory does not bring the foil as close to the vortices.

The ground truth values well match the areas of high probability in the estimate, indicating that the estimator is functioning properly. In the last 8 seconds of Fig. 5.8(c), the area of highest probability differs from the ground truth by a significant amount. However, the estimate is only one grid-division away from ground truth. A finer grid of possible value of γ may reduce the estimation error, although a finer grid may also jeopardize the real time operation.

The estimates of γ and the initial value of ϕ are essentially constant, as expected, because the ground truth values are constant. One exception is in Fig. 5.8(a) at around 10 seconds, where the estimate of the initial ϕ increases to the correct value. This increase is accompanied by a decrease in the estimate of γ in Fig. 5.8(c) at the same time, illustrating the deep coupling of the three parameters in the Bayesian filter. A particular measurement may correspond to a vortex very

close and weak, or strong and far away due to the influence of a vortex decaying as the inverse of the distance. It is through the Bayesian filter's integration of these data through time (new measurements are taken each time step) and space (the distribution of the pressure sensors) that this ambiguity is removed.

The estimates of y_v follow a sinusoidal pattern as expected because the robot is tracking a sinusoidal reference trajectory. The estimator uses the dynamic model presented in Section 5.3 to shift the probability density at each time step according to the control input it chooses from Eqn. (5.27).

5.5.3 Discussion of results

The results in the previous section used a potential flow model of a foil in a vortex street combined with a grid-based Bayesian filter to estimate the location of the vortices within the street and demonstrate flow-relative control to an arbitrary reference trajectory. This worked through the interplay of the controller, system dynamics, pressure sensors, flow model, and estimator seen in Fig. 5.1. The estimator used pressure measurements to converge to the vortex location fast enough to allow for the controller to track the desired reference trajectory. Additionally, it was shown that the optimally observable reference trajectory is one that intersects with each vortex in the street, though in practice this yielded only a mildly better estimate compared to the biologically inspired slaloming trajectory. These experiments are the first steps in real-time wake estimation for use onboard robots exhibiting pursuit or schooling behavior.

5.6 Summary of chapter

In this chapter, in an effort to replicate the wake sensing capabilities of fish in nature, an artificial lateral line was used onboard a robotic foil to estimate the location of vortices within a Kármán vortex street. Furthermore, a control law was presented that actuates angle of attack in order to generate cross-stream lift and track an arbitrary reference trajectory through the vortex street. These goals were accomplished using a complex potential flow model and Bernoulli's principle to form a measurement equation that takes input of vortex street location and strength and outputs the expected pressure readings. This measurement equation was used in a Bayesian filter to provide a real-time estimate of vortex location which was then used as an input to the trajectory-tracking control law. The experimental demonstration shows the validity of the modeling work done in this chapter.

Chapter 6: Conclusion

This dissertation describes the investigation of bioinspired sensing and control for novel underwater vehicles, particularly for an autonomous, reaction-wheel driven, fish-inspired robot used in pursuit scenarios. This investigation was facilitated by many tools including nonlinear control, thin airfoil theory, potential flow, classical mechanics, and probability theory. The three main chapters of this work address three questions related to this effort. Chapter 3 developed data-driven modeling techniques to investigate which factors are most important to a successful pursuit. Chapter 4 determined how to guarantee capture in underwater pursuit by a fish-inspired robot. Chapter 5 investigated how we might track the wake of a flapping vehicle by taking inspiration from the lateral line seen in fish. The contributions of each of these efforts are outlined below in Sections 6.2.1 – 6.2.3. Section 6.3 makes suggestions for future work in this area.

6.1 Summary of research

The pursuit modeling tasks, which ultimately resulted in the technique I call Probabilistic Analytical Modeling, were focused on how to draw conclusions from nothing more than an experimental dataset of predator/prey interactions. The

technique was originally much more narrow in scope, applying only to the zebrafish case study addressed in Section 3.4. I realized that the technique could be applied much more generally by allowing the dynamics model and key metric to adapt to the particular predator/prey interaction being examined. The general methodology requires a researcher to select a dynamics model, fit probability densities of parameters in the model to the dataset, derive an expression for the expected value of a key metric, and vary the parameters in the model to see the effect on the key metric. Once this general method was established, I then turned to the bluefish case study in Section 3.3.

The bioinspired pursuit with a robotic fish tasks were a combination of both modeling and experimental goals. My early work on this task was focused on the bifurcation and limit cycle analyses, which showed under what control gains the fish exhibits the desired forward-swimming behavior. I heavily relied on the study of nonlinear dynamics presented in [120] and [121]. Once I well understood the dynamics of the fish robot under our feedback law, I began deriving a condition under which capture is guaranteed. This goal was achieved through many pages of pen-and-paper analysis, much of which was fruitless, but ultimately informed my decisions on what approaches could yield the final result. The experimental portion of these tasks was mostly an exercise in robotics. I soldered and assembled the electronics package inside the fish, tuned the gains on the controller to produce forward-swimming behavior, and programmed the onboard logic to implement the same. I tested many low frequency radios in an attempt to send a signal deep enough in the water to reach the fish. Once I found a suitable transmitter, I attached a

microcontroller and programmed it to send the desired signals to the fish. I aimed (with the help of divers at the Space Systems Lab) the Qualisys motion capture cameras and calibrated the system several times over the experiments. I wrote the MATLAB program which communicates with both the motion capture software via a TCP/IP server and the fish via a 27MHz radio wave. I performed the experiments presented in this dissertation and made all necessary repairs to the robot throughout.

The wake sensing tasks were also a combination of modeling and experimental goals. The modeling was a relatively straightforward application of potential flow theory. I found the potential flow model of a Kármán vortex street in literature and applied the Milne-Thomson Circle theorem and the Joukowski transformation to model the flow field around a foil in a vortex street. The tool used for estimation in this project was the grid-based Bayesian filter and I provided a means to use it in real time to estimate the state of a vortex street. This was accomplished by identifying the states in the model that cannot be inferred from other parameters. Additionally, states such as flow speed or angle of attack were removed from the problem and taken as given since those have already been estimated with a Bayesian filter in the literature. I used empirical unobservability tools to conclude that the optimally observable path through the vortex street is one that crashes into each vortex as it comes downstream. Finally, I designed and performed the experiments presented here which successfully estimated the state of an artificially created vortex street and converged to the desired reference trajectories.

6.2 Highlighted original contributions

6.2.1 Probabilistic Analytical Modeling

The data-driven pursuit modeling work performed in this dissertation provides a new means for researchers and scientists to examine experimentally gathered kinematic data in order to determine which parameter is most important to a successful escape or pursuit. A five-step procedure is presented, which details the process to use probability density functions of parameters (speed, turning rate, etc.) fit from experimental data combined with a dynamics model derived from the kinematic data to quantify which factors are most important to survival. Secondary to this main contribution is the demonstration of this technique in two case studies. The case study on the predation of fundulus by bluefish showed for the first time that bluefish do not use time-optimal pursuit tactics in their choice of pursuit angle. The case study on the predation of larval zebrafish by adults showed that sensing range is most important to the survival, confirming what was originally determined in [42]. In contrast to that work, where a Monte Carlo approach was used by numerically simulating the dynamics model, this work provides analytical results by applying tools from probability theory and requires no simulations. This probabilistic analytical modeling technique provides researchers with an alternative to numerical Monte Carlo simulations in cases where analytical transparency is desired or numerical simulations too costly.

The following is a summary of contributions:

1. a probabilistic analytical modeling technique useful in determining key factors in survival in a predator/prey interaction given an experimental dataset of the kinematics of pursuit and

2. the negative result that bluefish do not optimize their pursuit angle with respect to time to capture.

6.2.2 Bioinspired pursuit

The bioinspired pursuit work performed in this dissertation provides a solid theoretical groundwork for using autonomous feedback control as means to either steer a flexible fish-robot with an internal reaction-wheel or engage in pursuit. The conditions under which the robot enters the desirable forward-swimming limit cycle are derived, similar to what is done in [132] with a non-autonomous controller using different techniques. These conditions depend on the physical parameters of the robot (weight, length, moment of inertia) as well as the gains chosen in the autonomous controller. I also present results relevant to pursuit with an underwater vehicle of this type, which needs special consideration because of the oscillatory behavior of the instantaneous heading around the desired heading. By specifying the desired heading to be a value related to the line-of-sight angle between the predator and prey, I show how pure pursuit, deviated pure pursuit, intercept, and parallel navigation can be achieved with a vehicle of this type. A boolean condition derived from the dynamics of the Chaplygin sleigh under the feedback control law determines whether or not capture is guaranteed. This condition depends on

the physical parameters of the robot, the gains chosen in the control law, and the maximum speed/acceleration capabilities of the evader. Finally, an experimental demonstration of the feedback law used onboard an autonomous fish robot in a 4 meter pursuit establishes that these results do not apply only in theory, but also in practice.

The following is a summary of contributions:

1. a bifurcation analysis specifying which control gains result in forward swimming behavior of the Chaplygin fish,

2. a condition to evaluate if pursuit by a Chaplygin fish will be successful given basic knowledge of prey capabilities, and

3. an experimental demonstration of this type of pursuit with a robot fish.

6.2.3 Vortex estimation and flow-relative control

The work in this dissertation on the topic of vortex estimation and flow-relative control makes many contributions to the artificial lateral line scientific community as well as the underwater robotics community. The grid-based Bayesian filter framework presented demonstrates in practice how to estimate the position of vortices within a vortex street in real time. This framework confirms the result from [89] where it was found that an artificial lateral line composed of pressure sensors is sensitive to enough information to estimate the vortex spacing, strength, location, etc. While that work shows it is possible, there has been no means to do so prior to the work of this dissertation. Within the context of navigating a fish robot through

a Kármán vortex street, tools from empirical unobservability are used to determine that the optimally observable trajectory through a vortex street is one that intersects with each vortex therein. This intuitive result concludes mathematically that for an artificial lateral line, a better estimate of the state of a flow structure is achieved by bringing the sensor array closer to the structure of interest. A control law is presented that allows control of the fish robot to any arbitrary reference trajectory through the vortex street using angle of attack as the input to generate cross-stream lift. This result facilitates future work in autonomous fish robot station holding behind obstacles or swimming fish.

The following is a summary of contributions:

1. specification and demonstration of a Bayesian filter framework that estimates the strength and location of vortices within vortex street,

2. determination that a trajectory intersecting with each vortex in the street is optimally observable, and

3. derivation and demonstration of a control law that modulates angle of attack to drive a fish robot to an arbitrary trajectory through a vortex street.

6.3 Suggestions for future work

Platform integration and improvement. This dissertation has pushed forward the sensing and control capabilities of bioinspired underwater vehicles, but has not fully integrated the various components into one vehicle. Chapter 4 includes the description of a robotic platform capable of pursuit when given extrasensory

information from the motion capture system where the fish was tested. Chapter 5 presents experimental demonstration of estimation and one-dimensional control relative to a vortex street.

Future work may look to integrate pressure sensors into an artificial lateral line on the free-swimming fish robot in order to track the wake of swimming bodies nearby. This sensing modality has an effective range on the order of one body length, so additional sensing modalities may be needed to track targets at a greater distance. Continuing with the bioinspiration theme, computer vision might be implemented to identify targets and determine their coordinates in the body frame of the robot. A more traditional method such as sonar may also be viable.

The robotic platform described in Chapter 4 has no means of depth control. For use outside the laboratory environment, depth control is critical and can be achieved through several avenues. In nature, fish have a lung-like organ called the swim bladder. A fish can control its buoyancy by generating or releasing gas within this bladder. A bioinspired analog to this could be implemented on the robotic platform by installing an expandable chamber under the silicone skin that changes the volume of water displaced in order to change buoyancy and hence depth. A second method to achieve depth control could be to implement pitch/roll control. The fish robot generates thrust by swimming and so could swim up or down by controlling pitch. Many underwater vehicles have internal actuated masses to control pitch and roll. A three-dimensional control moment gyro would also enable this type of control.

Schooling. Schooling or swarming is a burgeoning area of research. There are many examples of research into swarming techniques for autonomous aerial vehicles such as quadcopters, but there is comparatively little in the underwater domain. The robotic platform developed in this dissertation and its ability to autonomously control heading combined with the artificial lateral line sensing modality provides the tools to sense nearby agents and adjust heading accordingly to demonstrate schooling behavior with other fish robots. By studying the schooling behavior of fish to determine the rules each agent follows, it may even one day be possible to school with real fish.

Bibliography

[1] John D. Anderson. *Introduction to Flight*. McGraw Hill, 2015.

[2] William J. Van Trump and Matthew J. McHenry. The morphology and mechanical sensitivity of lateral line receptors in zebrafish larvae (*Danio rerio*). *The Journal of Experimental Biology*, 211, 2008.

[3] Sheryl Coombs. Signal detection theory, lateral-line excitation patterns and prey capture behaviour of mottled sculpin. *Animal Behavior*, 58(2):421–430, 1999.

[4] Andres Carrillo and Matthew J. McHenry. Zebrafish learn to forage in the dark. *Journal of Experimental Biology*, 219(4):582–589, 2016.

[5] Saurabh Sharma, Sheryl Coombs, Paul Patton, and Theresa Burt de Perera. The function of wall-following behaviors in the Mexican blind cavefish and a sighted relative, the Mexican tetra (*Astyanax*). *Journal of Comparative Physiology*, 195(3):225–240, 2009.

[6] Amy Gao and Michael Triantafyllou. *Bio-inspired pressure sensing for active yaw control of underwater vehicles*. IEEE, 2012.

[7] A. Chardenon, Gilles Montagne, M.J. Buekers, and Michel Laurent. The visual control of ball interception during human locomotion. *Neuroscience letters*, 334(1):13–16, 2002.

[8] Dennis M. Shaffer, Scott M. Krauchunas, Marianna Eddy, and Michael K. McBeath. How dogs navigate to catch frisbees. *Psychological Science*, 15(7):437–441, 2004.

[9] Brett R. Fajen and William H. Warren. Visual guidance of intercepting a moving target on foot. *Perception*, 33(6):689–715, 2004.

[10] Brett R. Fajen and William H. Warren. Behavioral dynamics of intercepting a moving target. *Experimental Brain Research*, 180(2):303–319, 2007.

[11] R.M. Olberg, A.H. Worthington, and K.R. Venator. Prey pursuit and interception in dragonflies. *Journal of Comparative Physiology A*, 186(2):155–162, 2000.

[12] Akiko Mizutani, Javaan S. Chahl, and Mandyam V. Srinivasan. Insect behaviour: Motion camouflage in dragonflies. *Nature*, 423(6940):604–604, 2003.

[13] Kaushik Ghose, Timothy K. Horiuchi, P.S. Krishnaprasad, and Cynthia F. Moss. Echolocating bats use a nearly time-optimal strategy to intercept prey. *PLoS biology*, 4(5):e108, 2006.

[14] Matthew J. McHenry, Jacob L. Johansen, Alberto P. Soto, Brian A. Free, Derek A. Paley, and James C. Liao. The pursuit strategy of predatory bluefish (pomatomus saltatrix). *Proceedings of the Royal Society B*, 286(1897), 2019.

[15] William D. Hamilton. Geometry for the selfish herd. *Journal of Theoretical Biology*, 31(2):295–311, 1971.

[16] Efstathios Bakolas and Panagiotis Tsiotras. Optimal pursuit of moving targets using dynamic Voronoi diagrams. *Proc. IEEE Conference on Decision and Control*, pages 7431–7436, 2010.

[17] William Scott and Noami Ehrich Leonard. Dynamics of pursuit and evasion in a heterogeneous herd. *Proc. IEEE Conference on Decision and Control*, pages 2920–2925, 2014.

[18] Tae-Hyoung Kim and Toshiharu Sugie. Cooperative control for target-capturing task based on a cyclic pursuit strategy. *Automatica*, 43(8):1426–1431, 2007.

[19] Daigo Shishika and Derek A. Paley. Mosquito-inspired swarming for decentralized pursuit with autonomous vehicles. In *American Control Conference*, pages 923–929. IEEE, 2017.

[20] N. A. Shneydor. *Missile Guidance and Pursuit: Kinematics, Dynamics, and Control*. Horwood, 1998.

[21] Paul J. Nahin. *Chases and escapes: the mathematics of pursuit and evasion*. Princeton University Press, 2012.

[22] Ermin Wei, Eric W. Justh, and P.S. Krishnaprasad. Pursuit and an evolutionary game. In *Proceedings of the Royal Society of London A*, volume 465, pages 1539–1559. The Royal Society, 2009.

[23] Rufus Isaacs. *Differential Games*. John Wiley and Sons, Inc., New York, 1965.

[24] D. Weihs and P. Webb. Optimal avoidance and evasion tactics in predator-prey interactions. *Journal of Theoretical Biology*, 106:189–206, 1984.

[25] A. Soto, W. J. Stewart, and M. J. McHenry. When optimal strategy matters to prey fish. *Integr. Comp. Biol.*, 55:55, 2015.

[26] P. Domenici and Robert Batty. Escape manoeuvres of schooling Clupea harengus. *J. Fish. Biol.*, 45(SUPPL A):97–110, 1994.

[27] P. Domenici and R.W. Blake. The kinematics and performance of the escape response in the angelfish (Pterophyllum-Eimekei). *J. Exp. Biol*, 156(1):187–205, 1991.

[28] J.H.S. Blaxter and L.A. Fuiman. The role of the sensory systems of herring larvae in evading predatory fishes. *Journal of the Marine Biological Association of the United Kingdom*, 70(02):413, 1990.

[29] R. C. Eaton, R. Didomenico, and Jonathan Nissanov. Flexible body dynamics of the goldfish C-start: implications for reticulospinal command mechanisms. *J. Exp. Biol*, 1988.

[30] W.J. Stewart, A. Nair, H. Jiang, and M.J. McHenry. Prey fish escape by sensing the bow wave of a predator. *Journal of Experimental Biology*, 217:4328–4336, 2014.

[31] Rune Vabø and Leif Nøttestad. An individual based model of fish school reactions: predicting antipredator behaviour as observed in nature. *Fisheries Oceanography*, 6(3):155–171, 1997.

[32] Daniel S. Calovi, Ugo Lopez, Paul Schuhmacher, Hugues Chaté, Clément Sire, and Guy Theraulaz. Collective response to perturbations in a data-driven fish school model. *Journal of The Royal Society Interface*, 12(104):20141362, 2015.

[33] W. Willman. Formal solutions for a class of stochastic pursuit-evasion games. *IEEE Transactions on Automatic Control*, 14(5):504–509, 1969.

[34] Alex James, Paul D. Baxter, and Jonathan W. Pitchford. Modelling predation as a capped rate stochastic process, with applications to fish recruitment. *Journal of The Royal Society Interface*, 2(5):477–487, 2005.

[35] Violet Mwaffo, Ross P. Anderson, Sachit Butail, and Maurizio Porfiri. A jump persistent turning walker to model zebrafish locomotion. *Journal of The Royal Society Interface*, 12(102):20140884, 2015.

[36] Emily A. Kane and Timothy E. Higham. Modelled three-dimensional suction accuracy predicts prey capture success in three species of centrarchid fishes. *Journal of The Royal Society Interface*, 11(95):20140223, 2014.

[37] Pieter Boets, Koen Lock, Marjolein Messiaen, and Peter L.M. Goethals. Combining data-driven methods and lab studies to analyse the ecology of *Dikerogammarus villosus* . *Ecological Informatics*, 5(2):133 – 139, 2010.

[38] Itai Dattner, Ezer Miller, Margarita Petrenko, Daniel E. Kadouri, Edouard Jurkevitch, and Amit Huppert. Modelling and parameter inference of predator–prey dynamics in heterogeneous environments using the direct integral approach. *Journal of The Royal Society Interface*, 14(126):20160525, 2017.

[39] Erica Chauvet, Joseph E. Paullet, Joseph P. Previte, and Zac Walls. A lotka-volterra three-species food chain. *Mathematics magazine*, 75(4):243–255, 2002.

[40] P.H. Leslie and J.C. Gower. The properties of a stochastic model for the predator-prey type of interaction between two species. *Biometrika*, 47(3/4):219–234, 1960.

[41] Matthew Oremland and Reinhard Laubenbacher. Optimal harvesting for a predator-prey agent-based model using difference equations. *Bulletin of Mathematical Biology*, 77(3):434–459, 2015.

[42] A. Nair, C. Nguyen, and M.J. McHenry. A faster escape does not enhance survival in zebrafish larvae. *Proceedings of the Royal Society of London B*, page 20170359, 2017.

[43] Mauricio Guelman. A qualitative study of proportional navigation. *IEEE Transactions on Aerospace and Electronic Systems*, (4):637–643, 1971.

[44] A. Maguer, R. Dymond, A. Grati, R. Stoner, P. Guerrini, L. Troiano, and A. Alvarez. Ocean gliders payloads for persistent maritime surveillance and monitoring. In *Oceans-San Diego*, pages 1–8, 2013.

[45] Paul Ozog, Nicholas Carlevaris-Bianco, Ayoung Kim, and Ryan M. Eustice. Long-term mapping techniques for ship hull inspection and surveillance using an autonomous underwater vehicle. *Journal of Field Robotics*, 33(3):265–289, 2016.

[46] Michael Purcell, Dave Gallo, Greg Packard, Mark Dennett, Marcel Rothenbeck, Andy Sherrell, and Sylvain Pascaud. Use of remus 6000 auvs in the search for the air france flight 447. In *OCEANS*, pages 1–7, 2011.

[47] Daniela Rus and Michael T. Tolley. Design, fabrication and control of soft robots. *Nature*, 521(7553):467, 2015.

[48] Chunlin Zhou and K.H. Low. Design and locomotion control of a biomimetic underwater vehicle with fin propulsion. *IEEE/ASME Transactions on Mechatronics*, 17(1):25–35, 2012.

[49] Vladislav Kopman, Jeffrey Laut, Francesco Acquaviva, Alessandro Rizzo, and Maurizio Porfiri. Dynamic modeling of a robotic fish propelled by a compliant tail. *IEEE Journal of Oceanic Engineering*, 40(1):209–221, 2015.

[50] A.V. Borisov and I.S. Mamayev. The dynamics of a Chaplygin sleigh. *Journal of Applied Mathematics and Mechanics*, 73(2):156–161, 2009.

[51] Zhier Chen, Jiancheng Yu, Aiqun Zhang, and Fumin Zhang. Design and analysis of folding propulsion mechanism for hybrid-driven underwater gliders. *Ocean Engineering*, 119:125–134, 2016.

[52] Feitian Zhang, Patrick Washington, and Derek A. Paley. A flexible, reaction-wheel-driven fish robot: Flow sensing and flow-relative control. In *American Control Conference*, pages 1221–1226, 2016.

[53] Panagiotis Tsiotras, Haijun Shen, and Chris Hall. Satellite attitude control and power tracking with energy/momentum wheels. *Journal of Guidance, Control, and Dynamics*, 24(1):23–34, 2001.

[54] Phanindra Tallapragada and Vitaliy Fedonyuk. Steering a chaplygin sleigh using periodic impulses. *Journal of Computational and Nonlinear Dynamics*, 12(5):054501, 2017.

[55] Gilad Refael and Amir Degani. A single-actuated swimming robot: Design, modelling, and experiments. *Journal of Intelligent & Robotic Systems*, pages 1–19, 2018.

[56] Ivan A. Bizyaev, Alexey V. Borisov, and Sergey P. Kuznetsov. Chaplygin sleigh with periodically oscillating internal mass. *EPL (Europhysics Letters)*, 119(6):60008, 2017.

[57] Michael J. Fairchild, Peter M. Hassing, Scott David Kelly, Parthesh Pujari, and Phanindra Tallapragada. Single-input planar navigation via proportional heading control exploiting nonholonomic mechanics or vortex shedding. In *ASME Dynamic Systems and Control Conference and Bath/ASME Symposium on Fluid Power and Motion Control*, pages 345–352, 2011.

[58] Phanindra Tallapragada. A swimming robot with an internal rotor as a nonholonomic system. In *American Control Conference (ACC), 2015*, pages 657–662. IEEE, 2015.

[59] Anthony Bloch, John Baillieul, Peter Crouch, Jerrold E. Marsden, Dmitry Zenkov, Perinkulam Sambamurthy Krishnaprasad, and Richard M. Murray. *Nonholonomic Mechanics and Control*. Springer, 2003.

[60] John D. Anderson. *Fundamentals of Aerodynamics*. McGraw Hill, 2007.

[61] Phanindra Tallapragada and Vitaliy Fedonyuk. Steering a Chaplygin sleigh using periodic impulses. *Journal of Computational and Nonlinear Dynamics*, 12(5):054501, 2017.

[62] Vitaliy Fedonyuk and Phanindra Tallapragada. Stick–slip motion of the Chaplygin sleigh with a piecewise-smooth nonholonomic constraint. *Journal of Computational and Nonlinear Dynamics*, 12(3):031021, 2017.

[63] Scott David Kelly, Michael J. Fairchild, Peter M. Hassing, and Phanindra Tallapragada. Proportional heading control for planar navigation: The Chaplygin beanie and fishlike robotic swimming. In *American Control Conference*, pages 4885–4890, 2012.

[64] Phanindra Tallapragada and Scott David Kelly. Self-propulsion of free solid bodies with internal rotors via localized singular vortex shedding in planar ideal fluids. *The European Physical Journal Special Topics*, 224(17-18):3185–3197, 2015.

[65] Jinseong Lee, Shyline Santana, Brian A. Free, and Derek A. Paley. State-feedback control of an internal rotor for propelling and steering a flexible fish-inspired underwater vehicle. In *Proc. American Control Conference*, pages 2011—2016, 2019.

[66] Hassan K. Khalil. *Nonlinear Control*. Pearson, 2015.

[67] Rufus Isaacs. *Differential Games: A Mathematical Theory with Applications to Warfare and Pursuit, Control and Optimization*. Dover, 1965.

[68] Jongki Moon, Kiseok Kim, and Youdan Kim. Design of missile guidance law via variable structure control. *Journal of Guidance, Control, and Dynamics*, 24(4):659–664, 2001.

[69] Tahereh Binazadeh and Mohammad Javad Yazdanpanah. Robust partial control design for non-linear control systems: a guidance application. *Proceedings of the Institution of Mechanical Engineers, Part I: Journal of Systems and Control Engineering*, 226(2):233–242, 2012.

[70] Sheryl Coombs. Smart skins: information processing by lateral line flow sensors. *Autonomous Robots*, 11(3):255–261, 2001.

[71] Francis D. Lagor, Levi DeVries, Kathryn Waychoff, and Derek A. Paley. Bio-inspired flow sensing and control: Autonomous rheotaxis using distributed pressure measurements. *Journal of Unmanned System Technology*, 1(3), 2013.

[72] Brian A. Free, Mukund K. Patnaik, and Derek A. Paley. Observability-based path-planning and flow-relative control of a bioinspired sensor array in a karman vortex street. In *Proc. American Control Conference*, pages 548–554, 2017.

[73] P.G. Saffman. *Vortex Dynamics*. Cambridge University Press, 1992.

[74] Richard Mason. *Fluid Locomotion and Trajectory Planning for Shape-Changing Robots*. PhD thesis, California Institute of Technology, Pasadena, California, 2003.

[75] Ronald L. Panton. *Incompressible Flow*. Wiley, 2005.

[76] James C. Liao. The role of the lateral line and vision on body kinematics and hydrodynamic preference of rainbow trout in turbulent flow. *Journal of Experimental Biology*, 209(20):4077–4090, 2006.

[77] James C. Liao. Neuromuscular control of trout swimming in a vortex street: implications for energy economy during the Kármán gait. *Journal of Experimental Biology*, 207(20):3495–3506, 2004.

[78] James C. Liao. A review of fish swimming mechanics and behaviour in altered flows. *Philos. Trans. R. Soc. Lond., B, Biol. Sci.*, 362(1487):1973–1993, Nov 2007.

[79] Brian L. Partridge and Tony J. Pitcher. The sensory basis of fish schools: relative roles of lateral line and vision. *Journal of Comparative Physiology*, 135(4):315–325, 1980.

[80] M.J. McHenry, K.E. Feitl, J.A. Strother, and W.J. Van Trump. Larval zebrafish rapidly sense the water flow of a predator's strike. *Biology Letters*, 5(4):477–479, 2009.

[81] Horst Bleckmann. Reaction time and stimulus frequency in prey localization in the surface-feeding fish *Aplocheilus lineatus*. *Journal of Comparative Physiology*, 140(2):163–172, 1980.

[82] John Montgomery, Sheryl Coombs, and Matthew Halstead. Biology of the mechanosensory lateral line in fishes. *Reviews in Fish Biology and Fisheries*, 5(4):399–416, 1995.

[83] O. Akanyeti, P.J.M. Thornycroft, G.V. Lauder, Y.R. Yanagitsuru, A.N. Peterson, and J.C. Liao. Fish optimize sensing and respiration during undulatory swimming. *Nature Communications*, 7, 2016.

[84] Boris P. Chagnaud, Horst Bleckmann, and Michael H. Hofmann. Kármán vortex street detection by the lateral line. *Journal of Comparative Physiology*, 193(7):753–763, 2007.

[85] Yingchen Yang, Nam Nguyen, Nannan Chen, Michael Lockwood, Craig Tucker, Huan Hu, Horst Bleckmann, Chang Liu, and Douglas L. Jones. Artificial lateral line with biomimetic neuromasts to emulate fish sensing. *Bioinspiration & Biomimetics*, 5(1):016001, 2010.

[86] Levi DeVries, Frank D. Lagor, Hong Lei, Xiaobo Tan, and Derek A. Paley. Distributed flow estimation and closed-loop control of an underwater vehicle with a multi-modal artificial lateral line. *Bioinspiration & Biomimetics*, 10:1–15, 2015.

[87] Vicente I. Fernandez. *Performance analysis for lateral-line-inspired sensor arrays*. PhD thesis, Massachusetts Institute of Technology, 2011.

[88] Perry Y. Li and Saroj Saimek. Modeling and estimation of hydrodynamic potentials. In *Proc. IEEE Conference on Decision and Control*, volume 4, pages 3253–3258, 1999.

[89] Zheng Ren and Kamran Mohseni. A model of the lateral line of fish for vortex sensing. *Bioinspiration & Biomimetics*, 7(3):036016, 2012.

[90] Taavi Salumäe and Maarja Kruusmaa. Flow-relative control of an underwater robot. In *Proc. R. Soc. A*, volume 469, page 20120671, 2013.

[91] Roberto Venturelli, Otar Akanyeti, Francesco Visentin, Jaas Ježov, Lily D. Chambers, Gert Toming, Jennifer Brown, Maarja Kruusmaa, William M. Megill, and Paolo Fiorini. Hydrodynamic pressure sensing with an artificial lateral line in steady and unsteady flows. *Bioinspiration & Biomimetics*, 7(3):036004, 2012.

[92] Wei Wang, Xingxing Zhang, Jianwei Zhao, and Guangming Xie. Sensing the neighboring robot by the artificial lateral line of a bio-inspired robotic fish. In *Intelligent Robots and Systems (IROS)*, pages 1565–1570. IEEE, 2015.

[93] Adrian Klein and Horst Bleckmann. Determination of object position, vortex shedding frequency and flow velocity using artificial lateral line canals. *Beilstein Journal of Nanotechnology*, 2:276, 2011.

[94] Brian A. Free, Mathhew J. McHenry, and Derek A. Paley. Probabilistic analytical modeling of predator-prey interactions in fishes. *J. R. Soc. Interface*, 16(150), January 2019.

[95] Brian A. Free and Derek A. Paley. Model-based observer and feedback control design for a rigid joukowski foil in a kármán vortex street. *Bioinspiration & biomimetics*, 13(3), 2018.

[96] Brian A. Free, Matt McHenry, and Derek A. Paley. Non-deterministic predator-prey model with accelerating prey. In *Proc. American Control Conference*, pages 1202–1207, June 2018.

[97] James Ward Brown and Ruel V. Churchill. *Complex variables and applications*. McGraw Hill, 2009.

[98] Serdar Tulu. *Vortex Dynamics in Domains with Boundaries*. PhD thesis, Izmir Institute of Technology, 2011.

[99] Richard Hamming. *Numerical methods for scientists and engineers*. Courier Corporation, 2012.

[100] L.M. Milne-Thomson. *Theoretical Hydrodynamics*. Dover Publications, Inc., 1968.

[101] M. Sanjeev Arulampalam, Simon Maskell, Neil Gordon, and Tim Clapp. A tutorial on particle filters for online nonlinear/non-Gaussian Bayesian tracking. *IEEE Transactions on Signal Processing*, 50(2):174–188, 2002.

[102] Lawrence D. Stone, Carl A. Barlow, and Thomas L. Corwin. *Bayesian Multiple Target Tracking*. Artech House, Inc., 1999.

[103] G.W. Wei. A unified approach for the solution of the fokker-planck equation. *Journal of Physics A: Mathematical and General*, 33(27):4935, 2000.

[104] Henry Stark and John W. Woods. *Probability, Random Processes, and Estimation Theory for Engineers*. Prentice Hall, 1986.

[105] Christopher M. Bishop. *Pattern Recognition and Machine Learning*. Springer, 2006.

[106] R.P.W. Duin, P. Juszczak, P. Paclik, E. Pekalska, D. De Ridder, D.M.J. Tax, and S. Verzakov. A Matlab toolbox for pattern recognition. *PRTools version*, 3:109–111, 2000.

[107] Geoffrey Grimmett and David Stirzaker. *Probability and random processes*. Oxford university press, 2001.

[108] B.S. Lanchester and R.F. Mark. Pursuit and prediction in the tracking of moving food by a teleost fish (acanthaluteres spilomelanurus). *Journal of Experimental Biology*, 63(3):627–645, 1975.

[109] Tal Shima. Deviated velocity pursuit. In *Proc. of the AIAA Guidance, Navigation, and Control Conference, Hilton Head, SC*, 2007.

[110] Suzanne Amador Kane and Marjon Zamani. Falcons pursue prey using visual motion cues: new perspectives from animal-borne cameras. *Journal of Experimental Biology*, 217(2):225–234, 2014.

[111] Eric W. Justh and P.S. Krishnaprasad. Steering laws for motion camouflage. In *Proceedings of the Royal Society of London A: Mathematical, Physical and Engineering Sciences*, volume 462, pages 3629–3643. The Royal Society, 2006.

[112] W.J. Stewart, G.S. Cardenas, and M.J. McHenry. Zebrafish larvae evade predators by sensing water flow. *Journal of Experimental Biology*, 216:388–398, 2013.

[113] John Lygeros. Lecture notes on hybrid systems. In *Notes for an ENSIETA Workshop*, 2004.

[114] Rafal Goebel, Ricardo G. SanFelice, and Andrew R. Teel. Hybrid dynamical systems. *IEEE Control Systems Magazine*, 29(2):28–93, 2009.

[115] Jianghai Hu, John Lygeros, and Shankar Sastry. Towards a theory of stochastic hybrid systems. In *International Workshop on Hybrid Systems: Computation and Control*, pages 160–173. Springer, 2000.

[116] Morris R. Driels and Young S. Shin. Determining the number of iterations for Monte Carlo Simulations of weapon effectiveness. *Naval Postgraduate School, Dept. of Mechanical & Astronautical Engineering*, 2004.

[117] Peter Eris Kloeden, Eckhard Platen, and Henri Schurz. *Numerical solution of SDE through computer experiments*. Springer Science & Business Media, 2012.

[118] Joseph Troy Lee Tuttle. Studies of systems with nonholonomic constraints: The segway and the chaplygin sleigh. Master's thesis, Purdue University, 2014.

[119] Steven H. Strogatz. *Nonlinear dynamics and chaos with applications to physics, biology, chemistry, and engineering*. CRC Press, 2018.

[120] John Guckenheimer and Philip Holmes. *Nonlinear oscillations, dynamical systems, and bifurcations of vector fields*, volume 42. Springer Science & Business Media, 2013.

[121] Steven H. Strogatz. *Nonlinear dynamics and chaos: with applications to physics, biology, chemistry, and engineering*. CRC Press, 2018.

[122] Augusto Beléndez, Carolina Pascual, DI Méndez, Tarsicio Beléndez, and Cristian Neipp. Exact solution for the nonlinear pendulum. *Revista brasileira de ensino de física*, 29(4):645–648, 2007.

[123] Brian A. Free, Mukund K. Patnaik, and Derek A. Paley. Observability-based path-planning and flow-relative control of a bioinspired sensor array in a karman vortex street. In *American Control Conference*, pages 548–554, 2017.

[124] Peter S. Bernard. *Fluid Dynamics*. Cambridge University Press, 2015.

[125] Francis D. Lagor, Kayo Ide, and Derek A. Paley. Touring invariant-set boundaries of a two-vortex system using streamline control. In *Proc. IEEE Conference on Decision and Control*, pages 2217–2222, 2015.

[126] Levi DeVries and Derek A. Paley. Observability-based optimization for flow sensing and control of an underwater vehicle in a uniform flowfield. In *Proc. American Control Conference*, pages 1386–1391, 2013.

[127] Branislava Ćurčić-Blake and Sietse M. van Netten. Source location encoding in the fish lateral line canal. *Journal of Experimental Biology*, 209(8):1548–1559, 2006.

[128] Haniu Sakamoto and H. Haniu. A study on vortex shedding from spheres in a uniform flow. *Journal of Fluids Engineering*, 112(4):386–392, 1990.

[129] Turgut Sarpkaya. Computational methods with vortices- the 1988 freeman scholar lecture. *ASME, Transactions, Journal of Fluids Engineering*, 111:5–52, 1989.

[130] Quen-yaw Sheen. *Potential flow analysis of unsteady Jourkowski airfoil in the presence of discrete vortices*. PhD thesis, University of Colorado, 1986.

[131] Arthur J. Krener and Kayo Ide. Measures of unobservability. In *Proc. IEEE Conference on Decision and Control*, pages 6401–6406. IEEE, 2009.

[132] Vitaliy Fedonyuk, Phanindra Tallapragada, and Yongqiang Wang. Limit cycle analysis and control of the dissipative chaplygin sleigh. In *ASME 2017 Dynamic Systems and Control Conference*. American Society of Mechanical Engineers, 2017.